2016

Robustness of Topological Superconductivity in Solid State Hybrid Structures

Piyapong Sitthison

Robustness of Topological Superconductivity in Solid State Hybrid Structures

Piyapong Sitthison

Dissertation submitted
to the Eberly College of Arts and Sciences
at West Virginia University
in partial fulfillment of the requirements for the degree of
Doctor of Philosopy in
Physics

Approved by

Tudor Stanescu, Ph.D., Chair
David Lederman, Ph.D.
Edward Flagg, Ph.D.
Mikel Holcomb, Ph.D.
Adam M. Halasz, Ph.D.

Department of Physics and Astronomy
Morgantown, West Virginia
2016

Keywords:
Topological insulator, Topological superconductor, Majorana bound states

Abstract

Robustness of Topological Superconductivity in Solid State Hybrid Structures

Piyapong Sitthison

The non-Abelian statistics of Majorana fermions (MFs) makes them an ideal platform for implementing topological quantum computation. In addition to the fascinating fundamental physics underlying the emergence of MFs, this potential for applications makes the study of these quasiparticles an extremely popular subject in condensed matter physics. The commonly called 'Majorana fermions' are zero-energy bound states that emerge near boundaries and defects in topological superconducting phases, which can be engineered, for example, by proximity coupling strong spin-orbit coupling semiconductor nanowires and ordinary s-wave superconductors. The stability of these bound states is determined by the stability of the underlying topological superconducting phase. Hence, understanding their stability (which is critical for quantum computation), involves studying the robustness of the engineered topological superconductors. This work addresses this important problem in the context of two types of hybrid structures that have been proposed for realizing topological superconductivity: topological insulator - superconductor (TI-SC) and semiconductor - superconductor (SM-SC) nanostructures. In both structures, electrostatic effects due to applied external potentials and interface-induced potentials are significant. This work focuses on developing a theoretical framework for understanding these effects, to facilitate the optimization of the nanostructures studied in the laboratory.

The approach presented in this thesis is based on describing the low-energy physics of the hybrid structure using effective tight-binding models that explicitly incorporate the proximity effects emerging at interfaces. Generically, as a result of the proximity coupling to the superconductor, an induced gap emerges in the semiconductor (topological insulator) sub-system. The strength of the proximity-induced gap is determined by the transparency of the interface and by the amplitude of the low-energy SM (TI) states at the interface. In turn, this amplitude is strongly impacted by electrostatic effects. In addition, these effects control the value of the chemical potential in the nanowire (nanoribbon), as well as the strength of the Rashba-type spin-orbit coupling – two key parameters that determine the stability of the topological superconducting phase. To account for these critical effects, a numerically efficient Poisson-Schrödinger scheme is developed.

Contents

Dedication

To Prastana, Jarinya and Kamick Sitthison

Acknowledgments

This dissertation is a collection of work done under the supervision of Tudor Stanescu for the last five years. The first three years work is mainly about a field of topology in condensed matter physics. He introduced me to the topological insulators and superconductors for an application of realizing a topological quantum computation. The idea of a quantum computer was only a fantasy for me when I was a high school student. Having an opportunity to study the robustness of the system is a real expansion of my horizon. In the last two years of work, he pointed out that the electrostatic effect generated at the interface should play a major role in determining the stability of topological superconducting phase. The idea leads to the whole dissertation. It was the problem of Schrodinger-Poisson equation in 1D that I have a chance to show my skill of computational conformal mapping. Although the study in 1D system is not yet completed, the result is very promising. Moreover, the algorithm can be adapted and applied in many problems related to applications of Metal-Semiconductor junction. His expertise in physics is not only essential knowledge that I have to learn from him; also a characteristic of handling a situation expressing the manner of being a professional physicist. He always keeps the conversations short and precise, though he also shows his friendly gesture and kindness. I would like to express my gratitude for his time and effort that he has put on me.

This work could not be completed without useful discussions with John Stenger who is sharing an office with me. He is also another student under the supervision of Tudor Stanescu. We discussed many issues about topology, condensed matter physics and many topics that are not really related to physics. Our discussions lead to many great conclusions and sometime ending with open-end questions. His knowledge on a calculation of differential conductance gave me an insight to the significant role of the interface physics. I also would like to thank him for his help on the error correction and proofreading this dissertation.

List of Figures

List of Tables

Nomenclature

ARPES	Angle-Resolved Photoemission Spectroscopy
BdG	Bogoliubov de-Gennes
FQH	Fractional Quantum Hall
IQHE	Integer Quantum Hall Effect
MBS	Majorana Bound States
MZM	Majorana Zero Modes
PHS	Particle-Hole Symmetry
QSHE	Quantum Spin Hall Effect
QL	Quantuple Layer
SLS	Sub-Lattice Symmetry
SPT	Symmetry Protected Topological
SC	Superconductor
SM	Semiconductor
SOC	Spin-Orbit Coupling
TI	Topological Insulator
TQPT	Topological Quantum Phase Transition
TRS	Time-Reversal Symmetry
TSC	Topological Superconductor

Chapter 1

Introduction

Water has three phases, solid, liquid and gas. A phase change can be induced, for example, by tuning temperature, while pressure and all other thermodynamic variables are kept constant. The phenomenon is very intuitive because we often witness it in nature and, as a result, take it for granted. However, the formalism describing this elementary process is based on rather sophisticated and carefully defined concepts, such as heat and energy. The phase transitions of water (e.g., from liquid to gas) are standard examples of phase transitions. The physical quantities involved in the description of this type of process can be defined classically and the relations among them are well understood within classical thermodynamics. This knowledge has a significant practical side: understanding the relation between the phase transitions of water and temperature have led to technological advances, such as, for example, the steam engine. Nonetheless, in addition to the science, the development of the steam engine involved hundreds of years of engineering, from the aeolipile of the ancient Greeks to the first practical steam engine constructed by Thomas Savery (1698).

For crystalline solids, the electrical conductivity can be used to categorize different

materials into two classes: insulators and conductors. From a quantum mechanical perspective, one can use the energy gap of the material to classify it: a nonzero gap corresponds to an insulating phase, while a vanishing gap makes the material a conductor. Note that in this case the use of quantum mechanics is critical. Unlike the classification of the phases of water, which can be completely understood classically, the classification of materials according to their electric transport properties can only be explained (properly) by quantum mechanics. Although temperature affects conductivity, the physics that describes this transport phenomenon is qualitatively different from that involved in the process of turning ice into vapor. But different physics requires different conceptual tools; not having the appropriate tools makes certain phenomena look strange or even incomprehensible.

The quantum Hall effect is a great example of a 'thing that cannot happen'. Indeed, at the time of its discovery the paradigm for understanding the existence of distinct phases of matter was based on Landau's symmetry breaking theory: two phases are distinct if they have different symmetries. Going from one phase to the other requires a change in the symmetry of the system and involves passing through a phase transition. Quantum Hall states, on the other hand, have all the same symmetry, yet they are separated by phase transitions. If symmetry is out of question, what makes these phases distinct? The answer that eventually emerged is *topology*. The quantum Hall liquids do not have long-range order and cannot be distinguished based on their local properties, i.e. using a local order parameter. It is some global, topological property that makes them distinct. To use a simple analogy, a sphere and a torus are locally indistinguishable: locally they both look like $\mathbb{R}_2$, as we may know from living on Earth. Nonetheless, their global (topological) properties are clearly distinct and there is no way to smoothly transform one into

the other without 'cutting' the object (i.e. going through a phase transition).

Once the new paradigm that recognizes the role of topology was born, many new predictions were made and new scenarios were proposed. One of the most beloved children of the new paradigm is the Majorana fermion, a type particle predicted in the late 1930s by the homonym Italian physicist but not discovered for more than 70 years, which reemerged as a quasiparticle in topological superconductors. Below, I will summarize the main ideas behind the classification of phases of matter based on the concept of topology. I will start my story with a bief history of the field.

1.1 Brief History of Topological Matter

The beginning of the topological era in condensed matter physics is marked by the discovery of the Integer Quantum Hall Effect (IQHE) in 1980 by von Klitzing, Dorda and Pepper [37]. A two-dimensional electron gas hosted by a semiconductor quantum well is placed under a strong (perpendicular) magnetic field at low temperature. In these conditions, the system is characterized by a vanishing longitudinal conductivity, σ_{xx}, and by the emergence of a quantized Hall conductivity, σ_{xy}, which comes in integer multiples of e^2/h. The discrete and extremely well defined nature of the Hall conductivity in IQHE cannot be explained by the Landau theory of symmetry breaking. It was not until the work of Thouless, Kohmoto, Nightingale and den Nijs (TKNN) in 1982 that a successful explanation for the quantization of σ_{xy} was provided using Kubo's formula [65]. Although the word "topology" was not used in that work, it basically showed that the Hall conductance of an IQH liquid is proportional to a topological invariant (the so-called first Chern number). In 1983, Avron published a paper discussing the work of Thouless *et al.* and pointed out that the integer that quantizes the Hall conductance is, in fact, a topological invariant [7].

The word "topology" was entering the world of condensed matter physics. By the end of 1983, Simon was emphasizing the relation of the topological invariant to Berry's phase [57]. Note that Berry's original paper was not published until 1984. Simon's work provided an appealing mathematical framework which greatly facilitated the understanding the IQHE in terms of topological properties of the ground state.

The strong magnetic field and low temperature were limiting factors that led to the idea that topological quantum states, such as the quantum Hall fluids, are exotic states that can occur only in extreme conditions. In 1988, Haldane proposed a mathematical model to realize IQHE without a net magnetic flux [25]. More specifically, Haldane realized that the key ingredient necessary for realizing the quantum Hall effect is not the magnetic field itself, but the absence of time-reversal symmetry. The key role of the magnetic field is to break the time-reversal symmetry. Haldane proposed a model of spinless fermions on a honeycomb lattice in the presence of a periodic magnetic field. The magnetic field has the property that the total flux through each unit cell is zero.

Although Haldane's model realizes the IQHE with zero net magnetic flux, its practical realization would be very challenging. Nonetheless, the conceptual simplicity of the model, which makes the role of topology extremely transparent, places the Haldane model as the 'first stop' in the theoretical effort of understanding the role of topology in condensed matter physics. In 2005, Kane and Mele generalized Haldane's model by applying the idea to graphene and replacing the periodic (external) magnetic field by a spin orbit coupling field. Instead of spin-polarized electrons, the system has now spin-full particles and a spin-orbit interaction that preserves time-reversal symmetry. This marked the birth of the time-reversal-invariant (or $\mathcal{T}$-invariant) Quantum Spin Hall Effect (QSHE) [33], the first example of a so-called

$\mathbb{Z}_2$ topological insulator (TI). A more realistic model of QSHE was proposed by Bernevig *et al.,* in 2006 in the context of $HgTe$ quantum wells [9]. The authors pointed out that the actual spin orbit coupling in graphene is too small to realize the topological state proposed by Kane and Mele. In their proposal, Bernevig *et al.,* predicted that in a mercury telluride–cadmium telluride semiconductor quantum wells the electronic state changes from a normal to an "inverted" type when the thickness of the quantum well is varied. It did not take long for someone to pick up the idea and verify it experimentally. In 2007, König *et al.,* confirmed the QSHE in $HgTe$ quantum wells [38].

The progress in understanding the topological nature of these new phases of matter led to the refinement of the theory and to an explosion of new predictions. In 2007 Fu and Kane pointed out that the presence of inversion symmetry greatly reduce the difficulty of evaluating the Z_2-invariant and predicted that time-reversal invariant topological insulators can also exist in three dimensions, more specifically in $Bi_{1-x}Sb_x$ [23]. Again, within a year, the prediction was verified experimentally by Hsieh *et al.* in 2008 [29]. Soon after, Bi_2Te_3 and Bi_2Se_3 were also predicted and confirmed to be topological insulators. Due to the simplicity of its surface state and the presence of a large bulk gap, Bi_2Se_3 is currently the most studied TI material. The rather remarkable accuracy of the theoretical predictions leading to these discoveries indicates that the theory has captured the fundamental properties of this class of materials, which are essentially topological in nature.

This brief story is limited to the discovery of the so-called *topological insulators*. In essence, these are insulating phases of noninteracting fermions that are topologically distinct from the *trivial insulator*, i.e. the atomic insulator. In addition, driven by the potential applications in quantum computation, topological superconducting

phase were also investigated theoretically and are currently studied experimentally. In particular, the realization of zero-energy Majorana bound states in topological superconductors could be an important step toward topological quantum computation. It was the work of Kitaev in 2001 that first proposed a mathematical model for such a topological superconducting phase [36]. Later, various schemes were proposed for the practical realization of the Kitaev model in solid state heterostructures.

A complete topological classification of fully gapped free fermion systems – the so-called topological insulators and superconductors – has been developed for non-interacting systems described by Hamiltonians belonging to generic symmetry classes determined by time-reversal symmetry (TRS), particle-hole symmetry (PHS), and chiral symmetry [35, 55]. Note that in this context superconductors are treated at the mean-field level (e.i. within the Bogoliubov - de Gennes formalism) and can be viewed as gapped phase of noninteracting fermion systems having particle-hole symmetry. However, superconductivity is a fundamentally interacting phenomenon that occurs in systems of charged fermions interacting electromagnetically. If we take into consideration the dynamics of the electromagnetic field, superconductivity should be regarded as a phase of charged fermions interacting with a dynamical gauge field. This was shown to be phase that possesses so-called *intrinsic topological order*. Hence, the first topological phase was discovered in 1911 by Heike Kamerlingh Onnes. Of course, for almost a hundred years nobody understood the intrinsic topological structure of superconductivity.

The concept of *topological order* was introduced by X.-G Wen in 1990 [69] in the context of spin liquids. Later, it was applied to the best known topologically ordered states: the fractional quantum Hall (FQH) fluids [67, 41]. Note that quantum phases with intrinsic topological order emerge in strongly interacting systems, are ro-

bust agains *any* type of perturbation, and are characterized by exotic properties, such as bulk excitations with fractional statistics and fractional quantum numbers (i.e. the so-called *anyons*). What we call *topological insulators* are states with no intrinsic topological order: they do not have anyonic bulk excitations and are not robust against arbitrary perturbations, but only against perturbations that preserve certain symmetries (e.g. time-reversal). Topological insulators are, in fact, examples of so-called *symmetry protected topological* (SPT) states. These phases are distinct (i.e. a gapped quantum state belonging to one phase cannot be continuously connected with a gapped state belonging to a different phase without crossing a topological quantum phase transition characterized by the vanishing of the quasi-particle energy gap) as long as certain symmetry constraints are imposed (e.g., time-reversal symmetry is preserved). Once the symmetry constraints are removed, different phases become indistinguishable. By contrast, topological phases that have (intrinsic) topological order (e.g., fractional quantum Hall fluids) are distinct even in the absence of symmetry constraints. Besides the topological states of noninteracting fermions (i.e. topological insulators and, at the mean field level, topological superconductors), SPT phases include interacting states of fermions and bosons that do not have intrinsic topological order (but are topological distinct in the presence of certain symmetries). The interacting SPT phases, as well as the interacting quantum states with topological order are presently the objects of intense theoretical and experimental research. This thesis does not address these general problems, but focuses on the small subclass of noninteracting SPT phases (i.e. on topological insulators and superconductors). A summary of some major publications representing key steps in our understanding of topological quantum matter is provided in Table 1.1.

Onnes	1911	First topological phase (superconductivity), see [68]
...	...	...
Klitzing *et al.*	1980	Discovery of IQHE [37]
Tsui *et al.*	1982	Discovery of FQHE [67]
TKNN	1982	Hall conductance as a topological invariant [65]
Laughlin	1983	Wave function for the FQH fluid [41]
Avron	1983	Explicit use of the term "topological invariant" [7]
Simon	1983	Connection with Berry's phase [57]
Berry	1984	Geometric phase [10]
Haldane	1988	First model of a Chern insulator [25]
Wen	1990	The concept of 'topological order' [69]
Kitaev	2001	Model of 1D p-wave topological superconductor [36]
Kane & Mele	2005	First model of $\mathbb{Z}_2$ TI [33, 32]
Bernevig *et al.*	2006	Proposal of QSHE in $HgTe$ [9]
Konig*et al.*	2007	Discovery of QSHE in $HgTe$ [38]
Fu & Kane & Mele	2007	Prediction of 3D TI [24]
Schnyder *et al.*	2008	Classification of TIs and TSCs [55]
Hsieh *et al.*	2008	Confirmation of 3D TI in $Bi_{1-x}Sb_x$ [29]
Fu & Kane	2008	Prediction of MF in TI-SC structures [22]
Zhang *et al.*	2009	Prediction of 3D TI in Bi_2Te_3 and Bi_2Se_3 [75]
Xia *et al.*	2009	ARPES detection of surface states in Bi_2Se_3[73]
Chen *et al.*	2009	ARPES detection of surface states in Bi_2Te_3[13]
Sau *et al.*	2010	Prediction of MF in SM-SC structures [53]
Cook & Franz	2011	Prediction of MF TI nanowire - SC [15]

Table 1.1: Some relevant publications leading to proposals for the realization of topological superconducting phases and Majorana bound states in hybrid solid state structures.

1.2 Geometry & Topology

In the early 1980's, the concept of topology entered condensed matter physics in the context of understanding the integer and fractional quantum Hall effects. This marked the beginning of the 'topological era' in condensed matter physics. Before we discuss in more detail the physics of topological insulators and topological superconductors, we briefly introduce the concept of topology, then we discuss its relevance in the context of condensed matter physics.

Topology is a field of mathematics that studies those properties of certain abstract spaces that are preserved under continuous deformations. Given a set, one defines a collection of subsets, called *open sets*, that satisfy certain properties. The collection of all open subsets is called a *topology*. A set endowed with a topology is called a *topological space*. All our considerations involving the term 'topology' will concern properties of topological spaces that depend only on the choice of topology (i.e. on the collection of open subsets). Note that in the definition of the topological space the set itself can be anything, for example a geometric figure or a collection of functions defined on an abstract space [45]. To better grab the idea of topology, we will focus on the topological properties of geometric figures. This will provide an intuitive and quick way to absorb the main ideas.

In geometry, the concepts of length, angle and curvature are well defined and are fundamental in describing and understanding the properties of various geometric objects. For example, these quantities can be used to distinguish a sphere from a cube. On the other hand, topology is only concerned with those properties that are invariant under *continuous deformations*. The sphere, for example, can be continuously deformed into a cube, or any other shape that does not require cutting or tearing the surface. On the other hand, it is obvious that the sphere cannot be con-

tinuously deformed into a donut shape (e.g., a torus) without destroying the surface. A sphere and a donut are said to be *topologically distinct*, while the sphere and the cube are topologically equivalent. In other words, a sphere and a cube share some global property that is not affected by continuous deformations. To quantitatively

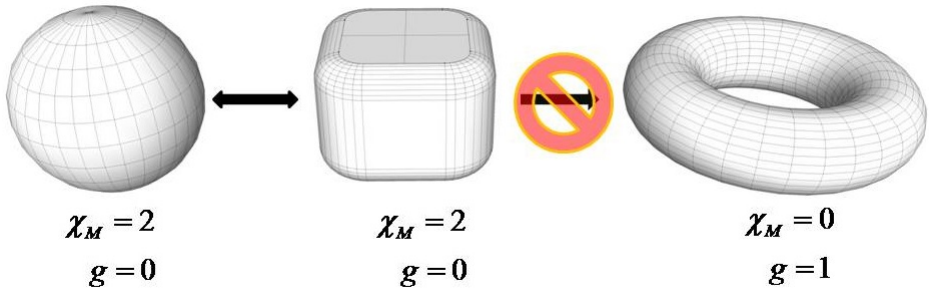

Figure 1.1: A sphere and a cube can be continuously deformed into each other (i.e. they are topologically equivalent), but they cannot be continuously deformed into a torus. The Euler characteristic χ_M (and the genus g) of topologically equivalent objects has the same value, i.e. it is a *topological invariant*.

capture this 'global property', we introduce the concept of *topological invariant*. As the name suggest, a topological invariant is a quantity that remains invariant under any continuous deformation. For geometric figures, a useful topological invariant is the Euler characteristic, which can be expressed using the Gauss - Bonnet theorem as

$$\chi_M = \frac{1}{2\pi} \oiint_M K \, dS \tag{1.1}$$

where K is the *Gaussian curvature*. The Gaussian curvature of a surface at a given point P is the product of the *principal curvatures* (κ_1 and κ_2) at that point, $K = \kappa_1 \kappa_2$. In turn, the principal curvatures can be obtained by considering the vector normal to the surface at P and the collection of normal planes containing the normal vector and intersecting the surface along a certain curve. This curve will, in general, have different curvatures at P for different normal planes; the principal curvatures κ_1 and

κ_2 are the maximum and minimum of these curvatures. Returning to the Euler characteristic, note that $\chi_M = 0$ for the torus and $\chi_M = 2$ for the sphere. Note that for orientable compact surfaces without boundary (such as the sphere and the torus), the Euler characteristic equals $2 - 2g$, where g – the so-called *genus* of the surface – counts the number of holes. Note that locally the curvature of the sphere may be the same as the curvature of the torus, but their total curvatures are different and this *global* property makes them topologically distinct objects.

From this simple example we can extract the following key ideas. Topology is concerned with the properties of certain mathematical objects (called topological spaces) that are invariant under continuous deformations. Two topological spaces are equivalent if they can be continuously deformed into one another. This continuous mapping defines an *equivalence relation* on the set of topological spaces and allows us to classify the topological spaces into different *equivalence classes*. Different classes are labeled by different values of certain *topological invariants*, e.g. the genus g. For example, a sphere and a cube belong to the same equivalence class characterized by $g = 0$, while a torus, a donut, and a coffee cup belong to an equivalence class characterized by $g = 1$. Note that there are many topological invariants associated with any given topological space. However, all members of an equivalence class will be characterized by the same value for each of these topological invariants.

1.3 Topology in Condensed Matter Physics

The failure to be able to identify the fundamental difference between two distinct IQHE phases does not 'prove' the incorrectness of the Landau's theory of symmetry breaking. However, it raises an awareness that the tools for the classification of quantum phases of matter should not be based on symmetry alone. In fact, there

certain *topological* properties of the underlying quantum states that successfully explain the 'mystery' of distinct IQHE phases sharing the same symmetry. Thus, the concept of topology can (and has to) be used to classify the phases of matter. We note that there are quantum phenomena discovered before the IQHE that cannot be properly explained without using the concept of topology, e.g., the Ahronov-Bohm effect [3] and solitons in polyactylene [27]. The work of Berry on geometric phases unveils the link between topology and quantum physics providing a solid and elegant explanation to quantum phenomena such as the Ahronov-Bohm effect. Also, it turns out that topology is a more common occurrence in condensed matter physics than one might have thought. Since condensed matter physics is essentially many-body quantum mechanics, Berry's work opened a new paradigm in the condensed matter world, which lead to a new classification of phases of matter based on their topological properties (in addition to their symmetry). To better understand the basis of this classification, it is worthwhile to make an effort to walk through a few relevant historical landmarks, including the topological interpretation of the Ahronov-Bohm effect [57] and the expression of the Hall conductance of the IQHE states in the terms of Berry's curvature [10].

1.3.1 Berry's phase

The phase of the wavefunction is typically believed to carry no physical meaning [11]. Phase differences, on the other hand, play a key role in quantum mechanics, e.g., in the context of quantum superpositions and interference processes. The role of geometric phases has been overlooked for decades, until Berry emphasized their non-trivial properties in 1984 [10]. It is perhaps surprising that a geometric phase naturally appears from an adiabatic evolution of the Schrödinger equation. To define

the basic concepts, consider a system whose Hamiltonian depends on a parameter that changes over time adiabatically, $R = R(t)$. Note that, more generally, R can be though of as a set of time-dependent parameters, $R = \{R_1, R_2, \dots\}$. The time-dependent Schrödinger equation can be written as

$$H\left(R\left(t\right)\right)\left|\psi\left(t\right)\right\rangle = i\frac{d}{dt}\left|\psi\left(t\right)\right\rangle, \tag{1.2}$$

where $H(R)$ is the parameter-dependent Hamiltonian of the system. For a given value of the parameter R, the eigenstates $|n, R\rangle$ of $H(R)$ form an orthonormal basis,

$$H(R)|n, R\rangle = E_n(R)|n, R\rangle. \tag{1.3}$$

We postulate that the Hilbert space (of physical states) spanned by the basis vectors $|n, R\rangle$ is independent of R. Assuming that we are looking for a solution of the Schrödinger equation (1.2) corresponding to the initial condition $|\psi(0)\rangle = |n, R_0\rangle$, the system will remain in the instantaneous eigenstate corresponding to $E_n(R(t))$, according to the adiabatic theorem. Consequently, the general solution of the time-dependent Schrödinger equation has the form

$$\left|\psi\left(t\right)\right\rangle = e^{i\gamma_n(t)}e^{-i\int_0^t dt'\, E_n(R(t'))}\left|n, R\left(t\right)\right\rangle. \tag{1.4}$$

where the second exponential represents the familiar dynamical phase and the first exponential is an additional phase that we discuss below. For a generic initial condition, the solution of Eq. (1.2) is given by the linear combination

$$\left|\Psi\left(t\right)\right\rangle = \sum_n c_n\left(t\right)\left|n, R(t)\right\rangle e^{i\theta_n(t)}, \tag{1.5}$$

where

$$\theta_n(t) = -\frac{1}{\hbar}\int_0^t E_n(t')\,dt'. \tag{1.6}$$

are dynamical phases. For simplicity, we will sometimes denote the state $|n, R(t)\rangle$ as $|n\rangle$ (i.e. the dependence of the parameter R is implicitly assumed). Solving for $c_n(t)$ yields

$$\dot{c}_n(t) = -c_n\left\langle n\left|\frac{d}{dt}\right|n\right\rangle - \sum_{n\neq m} c_m \frac{\left\langle n\left|\frac{d}{dt}H\right|m\right\rangle}{E_m - E_n} e^{-i(\theta_n(t)-\theta_m(t))}, \tag{1.7}$$

Since the change of the Hamiltonian is dictated by the 'speed' of the adiabatic evolution, i.e. by dR/dt, the second term can be made arbitrary small. Consequently, in the adiabatic approximation we have

$$c_n(t) = c_n(0)\, e^{i\gamma_n(t)} \tag{1.8}$$

where

$$\gamma_n(t) = i\int_0^t dt' \left\langle n, R(t')\left|\frac{\partial}{\partial t'}\right|n, R(t')\right\rangle \tag{1.9}$$

are additional phases.

Before we further discuss these phases, it is worth emphasizing that the parameter R in the above expressions can represent different physical quantities, e.g., some external field, a geometric property of the system, or the wave vector $\boldsymbol{k}$ associated with electron states in a lattice system. In the latter case, the electronic properties of a crystal are described (within a non-interacting approximation) by the single-particle Hamiltonian

$$H = \frac{-\hbar^2}{2m}\boldsymbol{\nabla}^2 + V(\boldsymbol{r}), \tag{1.10}$$

where m is the electron mass and $V(\boldsymbol{r}) = V(\boldsymbol{r} + \boldsymbol{a}_i)$ is a periodic potential, $\boldsymbol{a}_i$ being

the primitive lattice vectors. The eigenvectors of (1.10) satisfy the Bloch condition $\psi_{n\boldsymbol{k}}(\boldsymbol{r}+\boldsymbol{a}_i) = e^{i\boldsymbol{k}\cdot\boldsymbol{a}_i}\psi_{n\boldsymbol{k}}(\boldsymbol{r})$, which can be regarded as a $\boldsymbol{k}$-dependent boundary condition that generates a multitude of $\boldsymbol{k}$-dependent Hilbert spaces. However, we can perform a unitary transformation by introducing the cell-periodic function

$$u_{n\boldsymbol{k}}(\boldsymbol{r}) = e^{-i\boldsymbol{k}\cdot\boldsymbol{r}}\psi_{n\boldsymbol{k}}(\boldsymbol{r}). \tag{1.11}$$

The Hilbert space spanned by this basis is unique (i.e. $\boldsymbol{k}$-independent), but the Hamiltonian becomes $\boldsymbol{k}$-dependent

$$H(\boldsymbol{k}) = \frac{-\hbar^2}{2m}(\boldsymbol{\nabla} + i\boldsymbol{k})^2 + V(\boldsymbol{r}). \tag{1.12}$$

It is the Bloch Hamiltonian (1.12) that we can treat within the general Berry's phase formalism. More specifically, we have the following correspondence

$$\begin{aligned} &R \longrightarrow \boldsymbol{k}, \\ &H(R) \longrightarrow H(\boldsymbol{k}), \\ &|n, R\rangle \longrightarrow |u_n(\boldsymbol{k})\rangle. \end{aligned} \tag{1.13}$$

Let us now return to the additional phase (1.9). One may think that this is some arbitrary phase that can always be eliminated, e.g., be re-defining the zero of the energy (which will generate an extra dynamical phase). However, this is not the case if we consider *cyclic* evolutions of the system. More specifically, Berry considered adiabatic cyclic evolutions defined by the condition $R(0) \equiv R_0 = R(T)$, where T is the total evolution time. Such an evolution can be viewed as transporting the Hamiltonian, $H(R(t))$, around a closed path C in the parameter space M. In this

case, the general solution of the time-dependent Schrödinger equation with initial condition $|\psi(0)\rangle = |n, R_0\rangle$ can be expressed as

$$|\psi\,(T)\rangle = e^{i\gamma_n(C)} e^{-\frac{i}{\hbar}\int_0^T dt'\, E_n(R(t'))}\,|\psi\,(0)\rangle \tag{1.14}$$

where

$$\gamma_n = i \oint_C \langle n, R|\nabla_R|n, R\rangle \cdot dR. \tag{1.15}$$

We note that Eq. (1.15) can be obtained from Eq. (1.9) by changing the integration variable, $t' \to R$, $\partial/\partial t' = \dot{R}\nabla_R$, etc., and imposing the cyclic condition $R(0) = R(T)$. The quantity γ_n defined by this equation is the *Berry phase* angle or the *geometric phase* angle and the phase $e^{i\gamma_n}$ is called the *Berry* (or the *geometric*) phase. We note that the quantity γ_n is defined modulo 2π and represents a physical observable. Indeed, one can show that arbitrary choices of phases for the basis functions $|n, R\rangle$ can only change γ_n by integer multiples of 2π. The fraction $\gamma_n \pmod{2\pi}$ – and, consequently, the Berry phase $e^{i\gamma_n}$ – is uniquely determined by the geometry of the closed path C (hence the name *geometric phase*).

Using the Stokes' theorem the Berry phase angle can be rewritten in a form,

$$\gamma_n = \oint_C \vec{\mathcal{A}}_n \cdot d\vec{R} = \iint_S \vec{\nabla} \times \vec{\mathcal{A}}_n \cdot d\vec{S} = \iint_S \vec{\mathcal{F}}_n \cdot d\vec{S}, \tag{1.16}$$

where S is a surface in the parameter space having the curve C as its boundary, $\vec{\mathcal{A}}_n$ is the so-called *Berry connection* (associated with energy band n),

$$\vec{\mathcal{A}}_n = \langle n, R|\vec{\nabla}_R|n, R\rangle, \tag{1.17}$$

and $\vec{\mathcal{F}}_n$ is the so-called *Berry curvature* vector (for band n),

$$\vec{\mathcal{F}}_n = \vec{\nabla} \times \vec{\mathcal{A}}_n. \tag{1.18}$$

Here, we have assumed that $R = \{R_1, R_2, R_3\}$ is a three-component parameter. More generally, we can define the component μ of the Berry connection as $[\mathcal{A}_n]_\mu = \langle n, R| \frac{\partial}{\partial R_\mu} |n, R\rangle$ and introduce the Berry curvature *tensor* $\Omega_{\mu\nu} = \nabla_\mu \mathcal{A}_\nu - \nabla_\nu \mathcal{A}_\mu$, where $\nabla_\mu = \frac{\partial}{\partial R_\mu}$ and we omitted the band index n (to simplify the notation).

It is interesting to note that $\vec{\mathcal{A}}_n$ can be viewed as a 'magnetic' vector potential, while $\vec{\mathcal{F}}_n$ would correspond to a 'magnetic' field in the parameter space. From this perspective, the reason why the Berry phase cannot be eliminated by some choice of phases for the basis functions $|n, R\rangle$ is the gauge-independence of the integral of the vector potential along a closed loop, which is given by the flux of the magnetic field passing through the loop [12]. Indeed, consider the local phase shift $|n, R\rangle \to e^{i\varphi_n} |n, R\rangle$. The Berry connection will changed according to

$$\vec{\mathcal{A}}_n \to \vec{\mathcal{A}}'_n = \vec{\mathcal{A}}_n + \nabla \varphi_n. \tag{1.19}$$

Eq. (1.19) expresses the fact that the Berry connection is a gauge-dependent quantity, similar to the vector potential. By contrast, the curl of each of these quantities (i.e. the Berry curvature vector and the magnetic field, respectively) is gauge-independent and represents a physically observable quantity. Similarly, the integral of the Berry connection along a closed path (i.e. the Berry phase angle) representing the analog of the magnetic flux through the loop is also gauge-invariant (hence, observable). Finally, it is worthwhile to emphasize the analogy between the expression (1.16) corresponding to S being the full parameter space (e.g., the Brillouin zone

in the case of a crystalline system characterized by $\boldsymbol{R} = \boldsymbol{k}$) and the Gauss-Bonnet theorem (1.1). This suggests that the integral of the Berry curvature over the entire parameter space (the so-called *first Chern number*) represents a topological invariant that uniquely characterizes the topological nature of corresponding quantum state.

The relation between the expression of the Berry phase and the Gauss-Bonnet theorem can be further formalized within the framework of differential geometry. This was carried out in 1983 by Simon, who pointed out that the Berry phase can be essentially understood as the *holonomy* of a *fiber bundle* [57]. This recasting of the Berry phase formalism allows one to study a quantum system using the tools of differential geometry and topology. Such an analysis can provide powerful insight into the nature of different quantum phases and recipes for determining the topologically invariant quantities associated with them [79].

To sketch the basic concepts of this powerful formalism, let us consider a quantum system described by a Hamiltonian that depends on a parameter $R = \{R_1, R_2, \dots\}$ belonging to a certain parameter space represented by the manifold, $\mathcal{M}$. Note that a manifold is space that locally resembles the (N-dimensional) Euclidean space, e.g., a sphere, torus, Möbius band, etc. The Hamiltonian is assumed to evolve adiabatically as a function of R along a closed cycle $C \in M$. For each value of R the quantum states $|n, R\rangle$ form an orthonormal basis for the Hilbert of physical states. Note that the states $|n, R\rangle$ are defined up to an arbitrary phase factor. However, we assume that the phase factors are chosen so that $|n, R\rangle$ is a single-valued function of R, i.e. $|n, R(T)\rangle = |n, R(0)\rangle$. For simplicity, we also assume that the eigenvalues $E_n(R)$ are non-degenerate. Let the initial state of the system be $|n, R(0)\rangle$. According to the adiabatic theorem, at an arbitrary time $0 \leq t \leq T$ the system will be in a quantum state $e^{i\varphi}|n, R(t)\rangle$. If we regard $e^{i\varphi}|n, R\rangle$ with $0 \leq \varphi \leq 2\pi$ as a one-dimensional

mathematical object (equivalent to a circle), we can attach such an object to each point $R \in \mathcal{M}$ corresponding to the cyclic evolution C. In the language of differential geometry, $e^{i\varphi}|n, R\rangle$ with $0 \leq \varphi \leq 2\pi$ defines a *fiber* G and the collection of all fibers associated with the points R of the parameter manifold $\mathcal{M}$ define a *fiber bundle*. Since $e^{i\varphi}|n, R\rangle$ can be viewed as an element of a one-dimensional vector space, the corresponding fiber bundle is a *vector bundle*, i.e. a family of vector spaces parameterized by the parameter R with values in the manifold $\mathcal{M}$. If E is the total space of the fiber bundle, each fiber G is associated with a specific parameter value through the projector

$$\pi : E \to M \tag{1.20}$$

satisfying $\pi(G) = R$. For example, if the base manifold $\mathcal{M}$ is a circle, S^1, and the fiber G is a one-dimensional vector space (i.e. a line, for example the real line $\mathbb{R}$), the fiber bundle defined by the direct product $E = S^1 \times G$ is topologically equivalent to a cylinder (i.e. it is a cylinder up to arbitrary continuous transformations). A fiber bundle, such as the cylinder, that can be expressed as a direct product is called a trivial bundle. However, using the same base manifold and one-dimensional fibers one can construct a nontrivial fiber bundle by 'gluing' together the fibers in a different way. The Möbious strip is an example of such construction. Locally, it is identical to the cylinder, but their global properties are completely different.

To summarize, we have seen that the eigenstates $e^{i\varphi}|n, R\rangle$, which are defined up to a phase factor, correspond to a one dimensional vector space (i.e. a fiber) associated with each value of the parameter $R \in \mathcal{M}$. We can view this collection of vector space as a fiber bundle (more specifically, a vector bundle). Schematically, this mathematical object can be represented as in Fig. 1.2. Each line represents a fiber corresponding to a certain eigenvector $e^{i\varphi}|n, R\rangle$; one moves along the fiber by

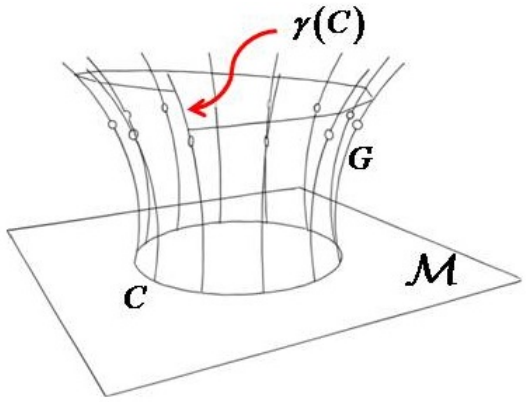

Figure 1.2: Schematic representation of the fiber bundle representing the collection of vector spaces $e^{i\varphi}|n, R\rangle$ with $0 \leq \varphi \leq 2\pi$ associated with each value of a parameter $R \in \mathcal{M}$. The adiabatic cyclic evolution of the system corresponds to R evolving along a closed path C in the parameter space. The corresponding evolution of the quantum state is represented by a curve (generally not closed) on the fiber bundle. The Berry phase is obtained as the holonomy $\gamma(C)$ corresponding to the parallel transport of the initial state vector on the bundle.

changing the phase angle φ. Only a few fibers are explicitly represented. Note that, strictly speaking, the fibers are topologically equivalent to a circle (because they are periodic in φ with period 2π), but we represented them as open lines for simplicity. Each fiber is projected onto a specific point R from the base manifold $\mathcal{M}$ (i. e. the parameter space).

Consider now the adiabatic cyclic evolution of the system as a result of slowly changing the parameter R along a certain closed path C in the parameter space. The initial state $e^{i\varphi_0}|n, R(0)\rangle$ is represented by the point $\varphi = \varphi_0$ on the fiber attached to $R = R(0)$. As one moves along C, the state at time $0 \leq t \leq T$ will be represented by a point on the fiber $R = R(t)$ and, after completing the cycle, it will return to the initial fiber (since $R(T) = R(0)$) but, in general, will correspond to a different point $\varphi_T \neq \varphi_0$. The difference $\varphi_T - \varphi_0$ represents the phase acquired by the quantum state during its adiabatic evolution. This phase difference contains a (standard) dynamical

component and the Berry phase, $e^{i(\varphi_T-\varphi_0)} = e^{i\gamma_n}e^{-i\alpha_{dyn}}$, where

$$\alpha_{dyn} = \frac{i}{\hbar}\int_0^T dt'\, E_n(R(t')). \tag{1.21}$$

Intuitively, one can view the dynamical component as an evolution along the fibers, while the Berry component results from moving from one fiber to the next, which corresponds to parallel transport on the fiber bundle. Movement along the fibers (hence α_{dyn}) depends on how fast we complete the cycle, while parallel transport (hence γ_n) is uniquely determined by the geometric properties of the fiber bundle and does not depend on T (assuming that we remain within the limits of the adiabatic approximation). If the fibers are parallel to each other (which means that the fiber bundle is 'flat'), a state corresponding to R with $\varphi = \varphi_R$ will be parallel transported into a state corresponding to $R + \delta R$ that has the same phase angle, $\varphi_{R+\delta R} = \varphi_R$. The resulting Berry phase after completing the cycle will be zero. If, on the other hand, there is some curvature, there will be a non-vanishing Berry phase. The key point is that the Berry phase $e^{i\gamma_n}$ is given by the holonomy (i.e. phase difference) that corresponds to parallel transport on the fiber bundle and that differential geometry provides powerful tools for characterizing it.

To formally describe parallel transport on the fiber bundle we consider the state $|\psi(t)\rangle = e^{i\varphi(t)}|n, R(t)\rangle$ and transport it to $|\psi(t+dt)\rangle = e^{i\varphi(t+dt)}|n, R(t+d)\rangle$. Parallel transport is defined by the condition that the change $|\psi(t+dt)\rangle - |\psi(t)\rangle$ of the state vector be orthogonal on $|\psi(t)\rangle$. Note that this condition will generate a state at $t + dt$ that is, generally, different from the state produced by the unitary evolution generated by the Hamiltonian $H(R)$. Explicitly, we have

$$|\psi(t+dt)\rangle - |\psi(t)\rangle = \left(i\frac{d\varphi}{dt}e^{i\varphi}|n, R\rangle + \frac{dR}{dt}e^{i\varphi}\nabla_R|n, R\rangle\right)dt, \tag{1.22}$$

where $\nabla_R = \partial/\partial R$. The scalar product of this difference with $\langle\psi(t)| = e^{-i\varphi}\langle n, R|$ is zero, which gives the relation

$$\frac{d\varphi}{dt} = i\langle n, R|\nabla_R|n, R\rangle\frac{dR}{dt}. \tag{1.23}$$

Integrating Eq. (1.23) from $t = 0$ to $t = T$, which corresponds to the parameter R cycling along the loop C, gives the Berry phase angle

$$\gamma_n \equiv \gamma(C) = \varphi(T) - \varphi(0) = \oint_C dR \cdot \mathcal{A} \qquad (\text{mod } 2\pi), \tag{1.24}$$

where

$$\mathcal{A} = i\langle n, R|\nabla_R|n, R\rangle \tag{1.25}$$

is the so-called adiabatic connection. We conclude that the Berry phase acquired by a quantum system during a cyclic adiabatic evolution is given by the holonomy (i.e. phase difference) corresponding to parallel transport on a fiber bundle defined by the collection of vector spaces corresponding to the eigenstates of $H(R)$ associated with each value of the parameter R. This holonomy is a geometric property of the fiber bundle and does not depend on the speed of the evolution. Differential geometry provides a powerful framework for describing the properties of fiber bundles, including the characterization of parallel transport in terms of the connection $\mathcal{A}$. Note that this framework can be applied beyond the adiabatic evolution of non-degenerate states. Generalizations include the Aharonov-Anandan (non-adiabatic) phase [2] and the non-Abelian phase associated with degenerate energy levels (first discussed by Wilczek and Zee [71]).

1.3.2 Aharonov-Bohm effect

A phenomena that, at the time of its discovery, could suggest the incompleteness of quantum mechanics was elegantly explained nearly 25 years later based on the concept of geometric phase developed by Berry [10]. But there is more. The Aharonov-Bohm phase is not a simple *geometric phase* (i.e. a quantity that depends on geometric properties, such as the Berry curvature and the shape of the evolution path), but an example of *topological* phase (i.e. a quantity that only depends on the topology of the evolution path). To use a classical analogy, parallel transport of a vector on a sphere along a closed path C results in the direction of the vector being modified by a certain angle γ_C that depends on the shape of the path (more specifically on the solid angle subtended by C). The angle γ_C is an example of a *classical geometric holonomy*. By contrast, parallel transport on a Möbius band along a closed path Γ generates an angle $\gamma_\Gamma = 0$ or $\gamma_\Gamma = \pi$ that only depends on whether Γ loops around the Möbius band an even or an odd number of times. This is a *topological* property independent of the details of Γ and γ_Γ is an example of a *classical topological holonomy*. The Aharonov-Bohm phase is a quantum analogue of this quantity.

In classical electrodynamics the scalar and vector potentials are not observable quantities and can be viewed as a convenient mathematical tool. In quantum mechanics the potentials, rather than the fields, enter the canonical formalism. The work of Aharonov and Bohm [3] further emphasizes the importance of the vector potential in quantum mechanics. Consider a particle with mass m and charge q that is confined in a 'box' by a potential $V_{\boldsymbol{R}}(\boldsymbol{r}$ centered at $\boldsymbol{R}$ and is placed in an external magnetic field. The Hamiltonian that describes the dynamics of the quantum system

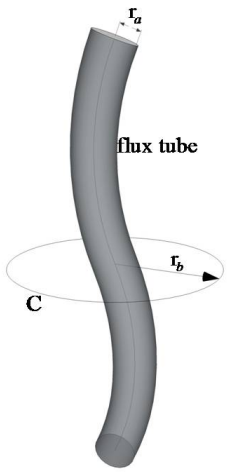

Figure 1.3: Charged particle moving around an finitely long, impenetrable solenoid with radius r_a carrying magnetic flux $\Phi = \pi r_a^2 B$. The magnetic field B is only non-zero inside the solenoid.

has the form

$$H = \frac{1}{2m}\left(\frac{\hbar}{i}\nabla - q\vec{A}\right)^2 + V_{\boldsymbol{R}}(\boldsymbol{r}), \tag{1.26}$$

where $\vec{A}$ are the vector potential associated with the magnetic field. In the absence of the magnetic field, the confined particle is in a state $\psi_n^0(\boldsymbol{r}-\boldsymbol{R})$ of energy E_n. Next, we assume that the magnetic field corresponds to a thin (impenetrable) flux tube carrying total magnetic flux Φ, as shown in Fig. 1.3. In the presence of a magnetic flux, the eigenvector corresponding to E_n will be

$$\psi_n(\boldsymbol{r}, \boldsymbol{R}) = \exp\left(\frac{iq}{\hbar}\int_{\boldsymbol{R}}^{\boldsymbol{r}} \vec{A}(\boldsymbol{x}) \cdot d\boldsymbol{x}\right) \psi_n^0(\boldsymbol{r} - \boldsymbol{R}). \tag{1.27}$$

Taking the box that contains the particle along a closed loop C that does not intersect the impenetrable flux tube, results in the quantum state acquiring a geometric phase given by

$$\gamma_{AB}(C) = \frac{q}{\hbar}\oint_C \vec{A} \cdot d\boldsymbol{R} = \nu_C \frac{q\Phi}{\hbar}, \tag{1.28}$$

where ν_C is the number of times C cycles around the flux line. Note that the Aharonov-Bohm phase $\gamma_{AB}(C)$ is a gauge-invariant (hence, observable) quantity that only depends on the topology of the path C (i.e. on how many times is goes around the flux tube). Moreover, the system acquires a nontrivial phase although the box is moving in a region with *no magnetic field* and the charged particle is confined inside the box. The information about the presence of the flux tube is extracted directly from the vector potential $\vec{A}$.

The Aharonov-Bohm phase can be naturally understood within the general Barry phase formalism. The Hamiltonian (1.26) depends parametrically on the position $\boldsymbol{R}$ of the box. The eigenfunction corresponding to a given value of the parameter is given by Eq. (1.27), $|n, R\rangle \to \psi_n(\boldsymbol{r}, \boldsymbol{R})$. As the box containing the particle is adiabatically transported along a closed loop C, the state vector acquires a geometric phase $\gamma(C)$ that can be expressed in terms of a Berry connection using Eqns. (1.24) and (1.25). Explicit calculations give $\mathcal{A} = \frac{q}{\hbar}\vec{A}$, i.e. the Berry connection is proportional to the external vector potential. Of course, in this case the Berry phase (1.24) takes the specific form given by Eq. (1.28).

A proposed experimental setup for realizing the Aharonov-Bohm effect through interference is illustrated in Fig. 1.4. When $\vec{A} \neq 0$, the wavefunction of the Hamiltonian in Eq.(1.26) with $V_{\boldsymbol{R}} = 0$ (i.e. no box) will carry an extra phase factor,

$$\psi^A_{I,II}(r) \equiv e^{iq\int_{\mathcal{O}}^{r} A(r')dr'}\psi_{I,II}(r) \tag{1.29}$$

where the $\psi_{I,II}(r)$ are wave functions corresponding to two different beams in the case $\vec{A} = 0$ and $\mathcal{O}$ is a reference point. The interference pattern can be studied by considering the superposition of the two beams, $\psi^A_I(r) + \psi^A_{II}(r)$. Setting $\psi^A_I(P) =$

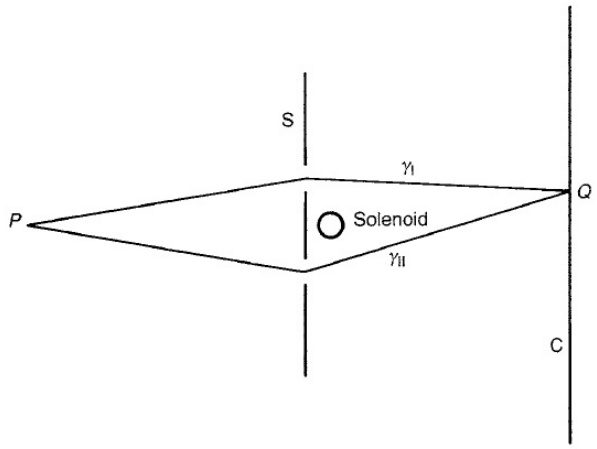

Figure 1.4: From Ref. [49]. An electron beam is split into two beams at point P. Each of the beams travels around an infinitely long solenoid. The beams meet again at point Q where the interference pattern is observed on the screen C. This reveals the information about the phase difference between the beams.

$\psi_{II}^{A}(P)$, the amplitude of the wavefunction at point Q can be expressed as

$$\psi_{I}^{A}(Q)+\psi_{II}^{A}(Q) = e^{iq\int_{\gamma_I}A(r')dr'}\psi_{I}(Q)+e^{iq\int_{\gamma_{II}}A(r')dr'}\psi_{II}(Q) \quad (1.30)$$

$$= e^{iq\int_{\gamma_{II}}A(r')dr'}\left(e^{iq\oint_{\gamma}Adr'}\psi_{I}(Q)+\psi_{II}(Q)\right) \quad (1.31)$$

The factor $e^{iq\int_{\gamma_{II}}A(r')dr'}$ will be canceled out when computing $|\Psi|^2$, but the phase factor $e^{iq\oint_{\gamma}Adr'}$ containing the Aharonov-Bohm phase will contribute to the constructive and destructive interference. Consequently, the interference pattern will independent of the shape of the closed loop γ but will contain information about the magnetic flux carried by the solenoid.

1.3.3 Integer Quantum Hall Effect

The quantization of the Hall conductance of an integer quantum Hall (IQH) in terms of a topological invariant was first demonstrated by Thouless, Kohmoto,

Nightingale, and den Nijs (TKNN) in 1982 [65] using the linear response theory. It was Simon [57] who interpreted the result within the general Berry phase formalism. Generally, the Hall conductance is given by

$$\sigma_{xy} = \frac{\langle j_x \rangle}{E_H}, \tag{1.32}$$

where E_H is the electric field in the y direction and $\langle j_x \rangle$ is the current density in the x direction. The current density can be obtained as the expectation value of the current density operator $\jmath_x \propto v_x$ in the presence of a perturbing potential $\phi = -Ey$ [56, 8]. Here, we follow a different path based on the investigation by Haldane of the Berry curvature of the Fermi surface [26]. An explicit calculation can be found in the lecture notes by Kai Sun [62].

Within a semiclassical model, the equations of motion for a free electron in an electromagnetic field are [6]

$$\dot{\vec{x}} = \frac{1}{\hbar}\frac{\partial \mathcal{E}_{0,n}\left(\vec{k}\right)}{\partial \vec{k}}, \quad \hbar\dot{\vec{k}} = -e\vec{E} - e\dot{\vec{x}} \times \vec{B}. \tag{1.33}$$

To calculate the Hall conductance, we have to incorporate the fact that the system is not continuous, but defined on a lattice. Hence, we have to consider Bloch wave functions $\psi_{n\boldsymbol{k}}(\boldsymbol{r})$, which account for the periodicity of the lattice system. The equations of motion derived using Bloch wave functions contain an extra anomalous velocity term [63]. Explicitly, we have

$$\dot{\vec{x}} = \frac{1}{\hbar}\left[\frac{\partial \mathcal{E}_{0,n}\left(\vec{k}\right)}{\partial \vec{k}} + \frac{d\vec{k}}{dt} \times \left[\vec{\nabla}_k \times \mathcal{A}\left(\vec{k}\right)\right]\right], \tag{1.34}$$

where $\mathcal{A} = i\langle u_n(\boldsymbol{k})|\boldsymbol{\nabla}_{\boldsymbol{k}}|u_n(\boldsymbol{k})\rangle$ is the Berry's connection defined in terms of the cell-

periodic functions $u_{n\boldsymbol{k}}(\boldsymbol{r}) = e^{-i\boldsymbol{k}\cdot\boldsymbol{r}}\psi_{n\boldsymbol{k}}(\boldsymbol{r})$. The equation of motion for the crystal momentum is not changed. On the other hand, Eq. (1.34) allows us to express the current density $\boldsymbol{j} = e\dot{\vec{x}}/A$, where A is the area of the two-dimensional electron gas, as

$$j = \frac{e}{A}\sum_{n,k}\frac{1}{\hbar}\left[\vec{\nabla}_k\varepsilon_n\left(\vec{k}\right) + \left(e\vec{E}\times\vec{e}_z + e\vec{v}\times\vec{B}\times\vec{e}_z\right)\mathcal{F}_n\left(\vec{k}\right)\right], \tag{1.35}$$

where we have introduced the z component of the Berry curvature vector, $\mathcal{F}_n(\vec{k}) = [\boldsymbol{\nabla}\times\boldsymbol{A}]_z$. The (non-vanishing) component along the x direction has the form

$$j_H = \frac{e}{A}\sum_{n,k}\frac{1}{\hbar}(e\vec{E}\times\vec{e}_z)\mathcal{F}_n(\vec{k}). \tag{1.36}$$

Hence, changing the summation over $\boldsymbol{k}$ into an integral, the Hall conductance (1.32) becomes

$$\sigma_{xy} = \frac{e^2}{\hbar}\sum_n\int_{BZ}\frac{d^2k}{2\pi}\,\mathcal{F}_n(\vec{k}), \tag{1.37}$$

where the summation over n includes all *occupied* bands and the integral of the Berry curvature is over the entire Brillouin zone.

It is worth comparing the integral in Eq. (1.37) with the Gauss-Bonnet formula (1.1). Both represent the integral of a curvature over a certain manifold and we know that the quantity in Eq. (1.1) is a *topological invariant* that is uniquely determined by the topological properties of the surface. The integral in Eq. (1.37) is a quantum analogue of the Gauss-Bonnet formula that defines an integer topological invariant called the *first Chern number*,

$$C_1^n = \int_{BZ}\frac{d^2k}{2\pi}\,\mathcal{F}_n(\vec{k}). \tag{1.38}$$

As we will see below, the first Chern number plays an important role in the classifica-

tion of topological phases of noninteracting fermion systems. The Hall conductance can be expressed in terms of this topological invariant as

$$\sigma_{xy} = \frac{e^2}{\hbar}\nu, \tag{1.39}$$

where the integer $\nu = \sum_n C_1^n$ is the sum of the first Chern numbers characterizing the occupied bands. For an integer quantum Hall system ν coincides with the (integer) filling factor that characterizes the system and, consequently, takes distinct values for each quantum Hall plateau.

We have shown that the concept of Berry phase provides a natural interpretation to the Aharonov-Bohm effect. In addition, the Berry phase formalism allows us to connect the Hall conductance of an integer quantum Hall fluid to a topological invariant, thus providing a firm basis for the classification of different quantum Hall states. This suggests that the concept of topology could be a useful tool for distinguishing and classifying quantum phases of matter.

1.4 General classification of quantum phases of matter

Landau's theory of symmetry breaking has proven to be a great tool for classifying different phases of matter. In essence, given a many-body system described by a Hamiltonian characterized by certain symmetries (e.g., spin-rotation symmetry), the physical states of the system can have the same symmetry as the Hamiltonian (e.g., a spin system in a paramagnetic state), or a lower symmetry (e.g., a ferromagnet). According to Landau's theory, states characterized by different symmetry properties belong to different phases and the transition from one phase to another is a so-

called *spontaneous symmetry breaking* phase transition. The concept of topology adds a new paradigm to the classification of quantum phases. Following the original example involving quantum Hall states, it was realized that distinct phases may share the same symmetry (i.e, the system can evolve from one phase to another without spontaneously breaking the symmetry), but the *topological* properties of the two phases have to be different. Within the new paradigm, one can identify two basic types of topological phases involving somehow different types of 'topological properties'. A useful criterion to distinguish them is based on the concept of *quantum entanglement*. This concept, which is at the heart of quantum mechanics, completes the tool set currently used for classifying quantum phases of matter. We note that below we only consider *gapped* quantum phases at *zero temperature*, i.e. quantum systems that are characterized by (bulk) ground states that are separated from higher energy state by a finite energy gap.

Concerning the concept of *entanglement*, let us consider two quantum states of a system of identical particles occupying certain orbitals (α and β) on two different sites (1 and 2). The first state, Eq. (1.40), is a direct product state (orbital α on site 1 and orbital β on site 2), while the second, Eq. (1.5), is an entangled state

$$|\Psi_{\alpha\beta}\rangle = |\alpha\rangle \otimes |\beta\rangle \tag{1.40}$$

$$|\Phi_{\alpha\beta}\rangle = \frac{1}{\sqrt{2}}(|\alpha\rangle \otimes |\beta\rangle + |\beta\rangle \otimes |\alpha\rangle) \tag{1.41}$$

In the case of the direct product state, 'cutting' the system in two will result in two sub-systems characterized by pure quantum states ($|\alpha\rangle$ and $|\beta\rangle$, respectively). By contrast, 'cutting' the entangled state will result in sub-systems in mixed quantum states. In a large quantum system, this type of entanglement can be local (sites within a certain finite range are entangled) or long range. One can show that the

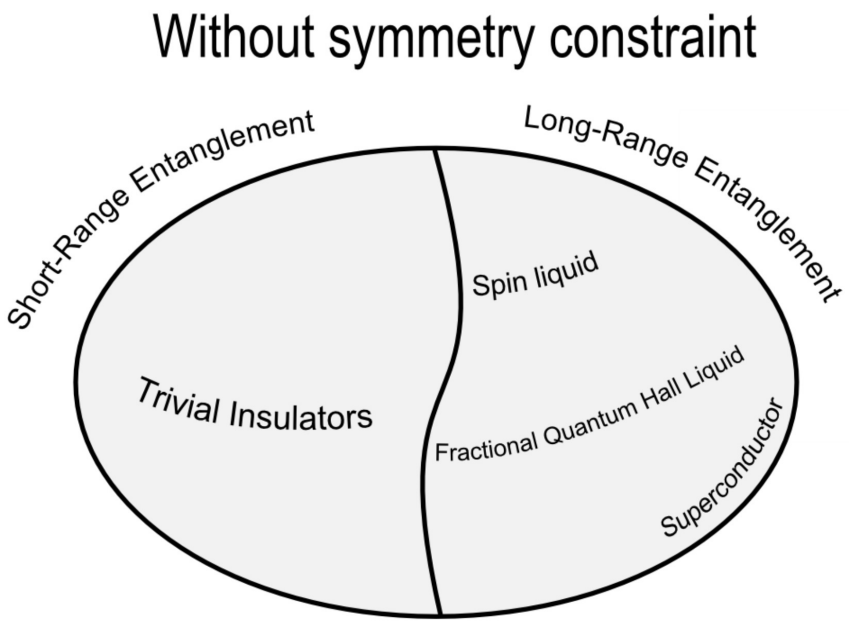

Figure 1.5: Gapped quantum phases of matter in the absence of symmetry constraints.

first type of entanglement, called *short-range entanglement*, can be essentially eliminated by performing some local unitary transformations. Consequently, short-range entangled states are, basically, similar to direct product states. By contrast, long-range entanglement cannot be removed by performing local unitary transformations. We note that, to characterize quantum entanglement in many-body systems, one can introduce various quantitative measures, such as the so-called *entanglement entropy*.

Long-range entanglement typically occurs in the presence of strong interactions. Gapped quantum states with long-range entanglement possess so-called *intrinsic topological order* and can be topologically distinct in the absence of any symmetry constraint. Two ground states corresponding to different sets of Hamiltonian parameters (e.g., coupling constant values and external fields) belong to the same phase if the two states can be connected continuously by varying these parameters (i.e. continuously deforming the Hamiltonian) *without closing the energy gap*. By

contrast, the states belong to distinct phases if connecting them continuously necessarily involves passing through a gapless state. The closing of the energy gap signals a topological quantum phase transition. Gapped quantum states with topological order are robust against *any* type of perturbation, in the sense that ground state will remain gapped for arbitrary (but, of course, small enough) perturbations of the Hamiltonian. The 'standard' example of long-range entangled quantum states with topological order are the *fractional* quantum Hall states. Other examples include superconductors (viewed as systems of charge particles interacting with dynamical gauge fields) and spin liquids. We note that in the absence of symmetry constraints (i.e. if we allow arbitrary deformations of the Hamiltonian), all short-range entangled states are topologically equivalent (i.e. can be continuously connected to each other without closing the energy gap) and, consequently, belong to the same phase: the trivial (atomic) insulator. The classification of gapped quantum states in the absence of symmetry constraints is illustrated schematically in Fig. (1.5).

In the presence of symmetries, an even more interesting picture emerges. If we only allow perturbations to the Hamiltonian that do not break certain symmetries (e.g., time reversal), even short-range entangled states become distinct. First, there are the standard (Landau-type) broken symmetry phases (i.e. phases having a lower symmetry that the Hamiltonian). In addition, phases that have the same symmetry as the Hamiltonian can be topologically distinct: two states belonging to different phases cannot be continuously connected without going through a topological quantum phase transition characterized by the vanishing of the energy gap. These phases, called *symmetry-protected* topological phases, include the now-famous (noninteracting) topological insulators and superconductor, as well as interacting quantum states, such as the Haldane phase of the spin-1 chain. The structure of strongly-interacting

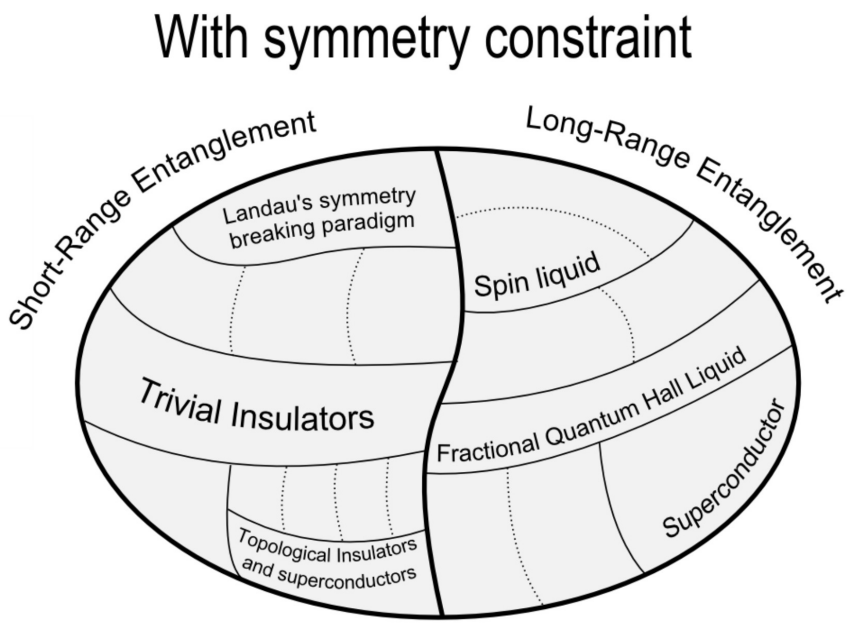

Figure 1.6: The 'big picture' of the of the topological classification of gapped quantum states in the presence of symmetry constraints.

long-range entangled phases also becomes more complex in the presence of symmetries. The classification of gapped quantum states in the presence of symmetry constraints is illustrated schematically in Fig. (1.6).

The classification of gapped quantum ground states was successfully described by Landau's theory of symmetry breaking until the discovery of the integer quantum Hall effect. Then, it was realized that states sharing the same symmetry can be qualitatively different, i.e. they can belong to distinct quantum phases. The properties that make these quantum states distinct are topological in nature. To fully classify the gapped quantum states, symmetry has to be supplemented by topology. In addition, quantum entanglement plays a key role in determining the topological properties of a quantum system. The 'topological quantum world' in the presence of symmetry constraints is schematically represented in Fig. (1.6). In the remainder of this thesis our attention will focus on the the small sub-class of non-interacting

topological phases, the so-called topological insulators and superconductors.

1.5 Generic symmetries

In the realm of topological quantum matter, topological insulators and superconductors represent the small subclass of noninteracting symmetry-protected topological (SPT) phases. These SPT phases correspond to gapped quantum ground states having non-trivial topological properties only in the presence of certain symmetry constraints imposed on the Hamiltonian that describes the system. Among various types of symmetries, there are three 'generic' symmetries that can be well defied even in the presence of disorder. These are the time-reversal, particle-hole, and chiral symmetries. To identify and classify the noninteracting SPT phases one has to i) classify all non-interacting Hamiltonians according to their generic symmetry properties and ii) classify the topologically distinct ground states corresponding to each symmetry class of Hamiltonians (for each given spatial dimension).

1.5.1 Time reversal symmetry

Time-reversal symmetry (TRS) is a symmetry of physical quantities and laws under a time-reversal (TR) transformation $t \to -t$. In classical mechanics, position and momentum change under a TR transformation as $\vec{r} \to \vec{r}$ and $\vec{p} \to -\vec{p}$, respectively. Consequently, if $\{\vec{x}\,(t)\,, \vec{p}\,(t)\}$ is a solution of the equations of motion for a particle, the time reversal symmetry of Newton's second law implies that $\{\vec{x}\,(-t)\,, -\vec{p}\,(-t)\}$ is also a solution. Consider, for example, a situation in which a ball is moving from A to B. If time is reversed $\vec{x}(t) \to \vec{x}(-t)$ and $\vec{p}(t) \to -\vec{p}(-t)$, and the ball, starting at B, would get back to the point A along the same the same trajectory [20]. Note

that this requires the Hamiltonian to be an even function of p,

$$H\left(\vec{x},\vec{p}\right)=H\left(\vec{x},-\vec{p}\right) \tag{1.42}$$

In quantum mechanics, the TR transformation is represented by an operator, $\mathcal{T}$, called time reversal operator. Consider the evolution of a quantum states $|\phi\rangle$ described by the time-dependent Schrödinger's equation

$$i\hbar\frac{\partial}{\partial t}|\phi\rangle=H|\phi\rangle. \tag{1.43}$$

Under TR, $|\phi\rangle\rightarrow\mathcal{T}|\phi\rangle$ and $H\rightarrow\mathcal{T}H\mathcal{T}^{-1}$ and the system is time-reversal symmetric if $\mathcal{T}H\mathcal{T}^{-1}=H$. Applying a TR transformation to Eq. (1.43) for a TR invariant Hamiltonian (i.e. changing t into $-t$ and applying the operator $\mathcal{T}$), leads to the following condition

$$\left(-iH\right)\mathcal{T}\left|\phi\right\rangle=\mathcal{T}\left(iH\right)\mathcal{T}^{-1}\mathcal{T}\left|\phi\right\rangle \tag{1.44}$$

which means that the TR operator is proportional to the complex conjugation operator, i.e. transforms i into $-i$. In the position representation, the time reversal operator acting on Schrödinger's equation yields

$$i\hbar\frac{\partial}{\partial t}\phi^{*}\left(x,-t\right)=H\phi^{*}\left(x,-t\right). \tag{1.45}$$

Consequently, if $\phi(x,t)$ is a solution of the Schrödinger equation with a TR symmetric Hamiltonian, $\psi^{*}\left(x,-t\right)$ is also a solution. Note that, under TR, the inner product of two states has the property

$$\langle\mathcal{T}\psi\mid\mathcal{T}\phi\rangle=\langle\phi\mid\psi\rangle=\langle\psi\mid\phi\rangle^{*}, \tag{1.46}$$

which means that the time reversal operator is an *anti-unitary* operator. This type of operators can be written in the form

$$\mathcal{T} = U_T \mathcal{K} \tag{1.47}$$

where U_T is a unitary operator and $\mathcal{K}$ is a complex conjugation operator.

Time-reversal changes the sign of the angular momentum. Consequently, when acting with $\mathcal{T}$ on a spin state we have

$$\mathcal{T} \left|\uparrow\right\rangle = e^{i\theta} \left|\downarrow\right\rangle , \tag{1.48}$$

where θ is a phase to be determined. Intuitively, reversing the spin corresponds to a π rotation, hence

$$\mathcal{T} = e^{i\theta} e^{-i\hat{S}_y \pi/\hbar} \mathcal{K} \tag{1.49}$$

where $\hat{S}_i$ is the spin angular momentum operator. For any spin state $|s, m_s\rangle$, acting with $\mathcal{T}$ twice yields

$$\mathcal{T}^2 \left|s, m_s\right\rangle = e^{-2\pi i \hat{S}_y/\hbar} \left|s, m_s\right\rangle = (-1)^{2s} \left|s, m_s\right\rangle . \tag{1.50}$$

It can be concluded that

$$\mathcal{T}^2 = \begin{cases} 1 & \text{integer spin} \\ -1 & \text{half} - \text{integer spin} \end{cases} . \tag{1.51}$$

The phase θ can be determined by considering the action of $\mathcal{T}$ on the spherical harmonics,

$$\mathcal{T} \left|l, m\right\rangle = (-1)^m \left|l, -m\right\rangle , \tag{1.52}$$

and generalizing this expression to spin states $|s, m_s\rangle$ with half-integer spin by. This can be done by selecting $\theta = \frac{\pi}{2}$. Hence the time reversal operator for half-integer spin can be expressed as

$$\mathcal{T} = ie^{-i\hat{S}_y\pi/\hbar}\mathcal{K}. \tag{1.53}$$

Alternatively, it can written as

$$\mathcal{T} = -i\sigma_y\mathcal{K} \tag{1.54}$$

where σ_i is the Pauli matrix. The presence of TRS in a half-integer spin system leads to the so-called Kramer's degeneracy [39]. If $\psi_{n,k,\sigma}$ is an eigenstate of the system, then

$$\mathcal{T}\psi_{n,k,\sigma} = \psi^*{}_{n,-k,-\sigma} \tag{1.55}$$

is also an eigenstate with the *same energy* and $\psi_{n,k,\sigma} \neq \psi_{n,-k,-\sigma}$. For a translation-invariant system, the Bloch Hamiltonian possesses TR symmetry if it satisfies the condition,

$$H(-k) = \mathcal{T}H(k)\mathcal{T}^{-1}. \tag{1.56}$$

In presence of spin-orbit coupling (SOC), the spin degeneracy will be lifted. However, as a consequence of Kramer's theorem, there will be a degeneracy at TR invariant momenta, e.g., $k = 0$ and $k = \pi/a$ in one dimension. Note that $-\pi/a$ and π/a represent the same momentum, as they differ by a reciprocal lattice vector. The characteristic signature of the energy bands of a Hamiltonian possessing TRS is $E_n(\boldsymbol{k}) = E_n(-\boldsymbol{k})$.

1.5.2 Particle-Hole symmetry

Particle-hole symmetry (PHS) has its origin its high energy physics, particularly in relation to the Dirac equation, which describes the behavior of both particles and antiparticles. The particle-hole transformation is also called charge conjugation, due to the fact that the corresponding operator turns a particle with charge q into its antiparticle with charge $-q$. Consider the Dirac equation

$$\left[\gamma^{\mu}\left(i\partial_{\mu} - eA_{\mu}\right) - m\right]\psi = 0, \tag{1.57}$$

where ψ is a spinor that describes the behavior of a particle of mass m with charge e in the presence of a potential A_{μ}. The charge conjugation operator, C, acting on ψ yields

$$C\psi = \psi^{c}. \tag{1.58}$$

Applying C to the Dirac equation, we have

$$\left[\gamma^{\mu}\left(i\partial_{\mu} + eA_{\mu}\right) - m\right]\psi^{c} = 0. \tag{1.59}$$

where ψ^{c} is the spinor describing the behavior of a particle with the same mass m but with opposite charge, $-e$.

In a Hamiltonian describing a (non-interacting) condensed matter system, the particle-hole (PH) operator switches the places of particles and antiparticles (holes). Superconductors provide the 'standard' example. Within the BCS theory of superconductivity, the mean-field (second quantized) Hamiltonian can be written using

the Bogoliubov de-Gennes (BdG) formalism as [5],

$$\hat{H} = \frac{1}{2} \begin{pmatrix} c^\dagger & c \end{pmatrix} \begin{pmatrix} h & \Delta \\ -\Delta^* & -h^T \end{pmatrix} \begin{pmatrix} c \\ c^\dagger \end{pmatrix} + \text{const.}, \tag{1.60}$$

where c and $c^\dagger$ are the fermion annihilation and creation operators, respectively, h is the single-particle Hamiltonian describing the normal (i.e. non-superconducting) state, and Δ is the superconducting pair potential. Note that for spin-1/2 fermions we have $c = (c_\uparrow, c_\downarrow)^T$ and h, Δ become 2×2 matrices. The single-particle Hamiltonian

$$\mathcal{H} = \begin{pmatrix} h & \Delta \\ -\Delta^* & -h^T \end{pmatrix}$$

called the *Bogoliubov-de Gennes* (BdG) Hamiltonian, describes the dynamics of the quasiparticles that emerge above the superconducting ground state.

For a system with spin-orbit coupling placed in an external electromagnetic field we have

$$h = \left(\vec{p} - e\vec{A}\right)^2 / 2m + V + \vec{U}_{SO} \cdot \vec{\sigma} \times \left(\vec{p} - e\vec{A}\right) - \mu \tag{1.61}$$

where

$$\begin{aligned} \vec{A} &= \text{vector potential, breaks time-reversal symmetry} \\ V &= \text{a scalar potential} \\ \vec{U}_{SO} &= \text{spin orbit field, breaks electron spin rotational symmetry} \\ \mu &= \text{chemical potential.} \end{aligned}$$

In the presence of translation invariance, the action of the PH operator on the c-

operator spinor results in the transformation

$$\begin{pmatrix} c_{k\uparrow}^\dagger & c_{k\downarrow}^\dagger & c_{-k\uparrow} & c_{-k\downarrow} \end{pmatrix}^T \rightarrow \begin{pmatrix} c_{-k\uparrow} & c_{-k\downarrow} & c_{k\uparrow}^\dagger & c_{k\downarrow}^\dagger \end{pmatrix}^T. \tag{1.62}$$

This result can be obtained by acting with the Pauli matrix τ_x on the particle-hole blocks. Hence, in this case (which corresponds to having triplet pairing), the PH operator is is proportional to τ_x and the condition for having particle-hole symmetry takes the form

$$\mathcal{H} = -\tau_x \mathcal{H}^* \tau_x. \tag{1.63}$$

This suggests that C can be represented as

$$C = \tau_x \mathcal{K} \tag{1.64}$$

where $\mathcal{K}$ is a complex conjugation operator. Note that $C^2 = 1$.

If the Hamiltonian contains spin rotational symmetry in the z-direction, the BdG Hamiltonian will commute with the z component of the spin operator,

$$[\mathcal{H}, J_z] = 0 \tag{1.65}$$

where

$$J_z = \begin{pmatrix} S_z & 0 \\ 0 & -S_z^T \end{pmatrix}. \tag{1.66}$$

In this case, the BdG Hamiltonian can be written as [55]

$$\hat{H} = \frac{1}{2} \begin{pmatrix} c_\uparrow^\dagger & c_\downarrow \end{pmatrix} \begin{pmatrix} h_\uparrow & \Delta \\ \Delta^* & -h_\downarrow^T \end{pmatrix} \begin{pmatrix} c_\uparrow \\ c_\downarrow^\dagger \end{pmatrix} + \text{const.} \tag{1.67}$$

where $h_\uparrow$ ($h_\downarrow$) is the single particle Hamiltonian for spin-up (spin-down) electrons in the normal state. Following the argument outlined above, we conclude that in this case (corresponding to singlet pairing) the charge conjugation operator can be represented as

$$C = -i\tau_y \mathcal{K}, \tag{1.68}$$

which squares to -1. To summarize, the particle-hole transformation is obtained by acting with an operator C that can be represented as in Eqns. (1.64) and (1.68) and has the property

$$C^2 = \begin{cases} -1 & \text{singlet} \\ 1 & \text{triplet} \end{cases} \tag{1.69}$$

In the presence of particle-hole symmetry, the energy dispersion satisfies the condition $E_-(-k) = -E_+(k)$, where E_- and E_+ represent the negative and positive energy bands of the BdG spectrum.

1.5.3 Chiral symmetry

The last generic symmetry that will be taken into this consideration can be viewed as a product of the TRS and PHS, $\mathcal{S} = \mathcal{T} \cdot \mathcal{C}$. Note that $\mathcal{S}$ does not represent an 'ordinary' symmetry, since it does not commute but rather *anti-commutes* with the Hamiltonian $\mathcal{S}H\mathcal{S}^{-1} = -H$. This symmetry, called *chiral symmetry*, is typically realized in solid state systems as a sub-lattice symmetry (SLS) in bipartite lattice systems.

A Hamiltonian possessing chiral (or *sublattice*) symmetry can always be arranged to have the form

$$H = \begin{pmatrix} 0 & T \\ T^\dagger & 0 \end{pmatrix}, \tag{1.70}$$

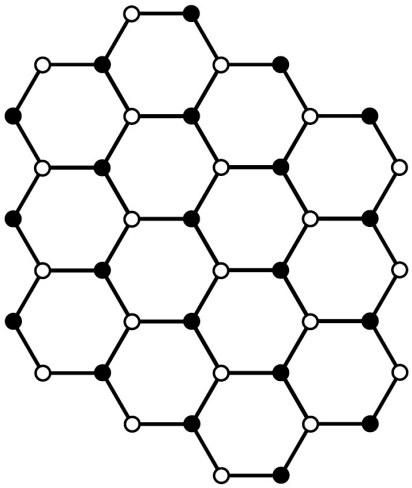

Figure 1.7: Bipartite lattice representing the honeycomb lattice structure of graphene.

where T is a hopping matrix that contains hoppings t_{AB} between sites on the two sublattices. Note that the tight-binding Hamiltonian in Eq. (1.70) is written in a sublattice basis of the form $\left\{ \begin{array}{cc} \psi_A & \psi_B \end{array} \right\}$. Note that the square of the chiral symmetry always equals to 1, $\mathcal{S}^2 = 1$. The consequence of a Hamiltonian possessing chiral symmetry is reflected in the energy spectrum as the property $E_+(k) = -E_-(k)$.

1.6 Symmetry Classification of Noninteracting Hamiltonians

To complete the topological classification of non-interacting gapped phases, the first task is to classify the non-interacting Hamiltonians according to their properties under generic (i.e. time-reversal, particle-hole, and chiral) symmetries. Why do we focus on this type of Hamiltonians? Because they are quite easy to work with and because they are relevant to understanding the physics of topological insulators (TIs)

and topological superconductors (TSCs). Typically, a *non-interacting* Hamiltonian describes a system where the interaction energy scale is much smaller than other relevant energy scales, for example the band gap. A *gapped phase*, on the other hand, refers to quantum ground states characterized by a bulk energy gap between an occupied (valence) band and an empty (conduction) band. Note that the energy gap characterizes the *bulk* of the system and not its boundaries (which may support gapless modes). For a superconductor treated at the mean field level, the gap represents the superconducting gap characterizing the quasiparticle spectrum.

Trivial insulators (such as the atomic insulators) are topologically equivalent, since the corresponding Hamiltonians can be continuously deformed among different systems without closing the bulk gap. Hence, in the absence of broken symmetries, all these insulators belong to the same phase. Can we conclude that all insulators are topological equivalent? The answer is no. A very good example is the IQHE, which has distinct states with the same symmetry and different values of the Hall conductance. The Hamiltonian of the system cannot be smoothly deformed (e.g., by varying the magnetic field) between quantum Hall states with different values of the Hall conductance without closing the gap (i.e. passing through a quantum phase transition). Hence, the distinct gapped phases are separated by gapless quantum states. Consequently, IQHE fluids are not equivalent to a typical insulator (e.g., a solid noble gas) and are not equivalent to each other. Note that the quantum Hall states require the presence of a perpendicular magnetic field, which breaks TRS. This suggests that symmetry properties play an important role in the emergence of topologically distinct phases. Let us briefly discuss the classification of non-interacting Hamiltonians according to their symmetry properties.

		TRS	PHS	SLS	d=1	d=2	d=3
Standard	A	0	0	0		$\mathbb{Z}$	
	AI	+1	0	0			
	AII	-1	0	0		$\mathbb{Z}_2$	$\mathbb{Z}_2$
Chiral	AIII	0	0	1	$\mathbb{Z}$		$\mathbb{Z}$
	BDI	+1	+1	1	$\mathbb{Z}$		
	CII	-1	-1	1	$\mathbb{Z}$		$\mathbb{Z}_2$
BdG	D	0	+1	0	$\mathbb{Z}_2$	$\mathbb{Z}$	
	C	0	-1	0		$\mathbb{Z}$	
	DIII	-1	+1	1	$\mathbb{Z}_2$	$\mathbb{Z}_2$	$\mathbb{Z}$
	CI	+1	-1	1			$\mathbb{Z}$

Table 1.2: Symmetry classification of non-interacting Hamiltonians and topological classification of topological insulators and superconductors in one-, two-, and three-dimensions.

Generic symmetry operators can be classified into two types [55],

$$\begin{aligned} P &: H = -PHP^{-1}, \quad PP^\dagger = 1, \quad P^2 = 1, \\ C &: H = \varepsilon_c C H^T C^{-1}, \quad CC^\dagger = 1, \quad C^T = \eta_c C, \end{aligned} \tag{1.71}$$

where ε_c and η_c can take values ± 1. The pair (ε_c, η_c) represents different realizations of the time-reversal or particle-hole symmetry, which can be summarized as follows:

$$\begin{aligned} (1,1) &= \text{TRS for spinless or integer spin} \\ (1,-1) &= \text{TRS for spinful, half (or odd) integer spin} \\ (-1,1) &= \text{PHS for triplet pairing} \\ (-1,-1) &= \text{PHS for singlet pairing} \end{aligned}$$

The P-type symmetry refers to the sublattice (chiral) symmetry. Note that, although superconductivity ensures the presence of PHS, particle-hole symmetry does not necessary imply superconductivity. An example is 1D polyacetylene, which can be described by a Hamiltonian in symmetry class class BDI, i.e. a hamiltonian that

has TRS with $\mathcal{T}^2 = +1$ and PHS with $\mathcal{C}^2 = +1$. Note that the presence of both TRS and PHS implies the presence of chiral symmetry with $\mathcal{S} = \mathcal{T} \cdot \mathcal{C}$. In general, a Hamiltonian can have TRS with $\mathcal{T}^2 = +1$, TRS with $\mathcal{T}^2 = -1$, or no TRS. Similarly, it can have PHS with $\mathcal{C}^2 = +1$, PHS with $\mathcal{C}^2 = -1$, or no PHS. Combining these possibilities results in nine different symmetry classes. In addition, if a Hamiltonian has no TRS and no PHS it may have chiral symmetry or not. This leads to a total of ten symmetry classes – the so-called '10-fold way' – summarized in Table (1.2) (left side of the table).

The symmetry classification shown in Table(1.2), was realized by Altland and Zirnbauer [5] and represents an extension of previous work by Wigner and Dyson on random matrix theory [70, 19]. A "0" in columns 3-5 means the absence of the corresponding symmetry, while $+1, -1$ in the TRS column refer to the presence of time-reversal symmetry for integer-spin and half integer-spin, respectively. Similarly, $+1, -1$ for PHS refers to the presence of particle-hole symmetry in systems with triplet and singlet pairing, respectively.

1.7 Topological Classification of Gapped Quantum Ground States

In the absence of spontaneous symmetry breaking, all physical systems described by Hamiltonians from a given symmetry class have the same symmetry. However, this does not mean that they belong to the same phase. Focusing on gapped phases, the next task is to classify all topologically distinct (gapped) ground states that correspond to Hamiltonians from a given symmetry class and have a specified spatial dimension. However, we note that the quantum ground state may have a different

symmetry that the Hamiltonian. This case falls into the standard framework of Landau's symmetry breaking theory and does not represent our main concern. The fundamental question here is the following: how many *distinct phases* are there that have the *same symmetry* as the Hamiltonian?

To answer this question one has to take into account that the (gapped) quantum states of matter are characterized by the topological properties of the ground state [69, 55]. In the case of non-interacting systems (and, more generally, for SPT phases), these topological properties are protected by the symmetries of the system. In the other words, the constraint imposed by the presence of certain symmetries (that correspond to the specific symmetry class of the Hamiltonian) ensures the existence of distinct topological properties. Any disorder or other type of perturbation that does not destroy these symmetries will not affect the topological properties of the system.

Having two different (gapped) ground states Ψ_1 and Ψ_2 corresponding to two Hamiltonians H_1 and H_2 from a given symmetry class, when do they belong to the same phase and when to different phases? Basically, the two ground state belong to the same phase if one can continuously connect them (by smoothly changing the Hamiltonian from H_1 to H_2) without closing the energy gap. Since a continuous evolution in the presence of a finite gap does not change the topological properties of the ground state, the states Ψ_1 and Ψ_2 are topologically equivalent. Hence all topologically equivalent ground states belong to the same phase and can be uniquely characterized by a certain topological invariant. By contrast, if Ψ_1 and Ψ_2 are not topologically equivalent, they belong to distinct phases. Connecting them requires passing through (at least) one state characterized by a vanishing energy gap.

Generically, one can imagine three different scenarios, as shown schematically

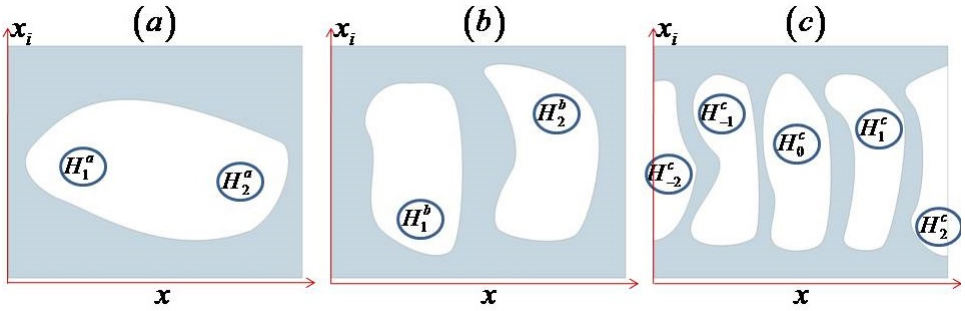

Figure 1.8: The three possible scenarios for the existence of topologically distinct phases within a given symmetry class. The Hamiltonian can be changed (without breaking the symmetries) by varying certain parameters $\{x, x_1, x_2, \dots\}$. The shaded areas correspond to gapless ground states, while the white areas are gapped phases. (a) One distinct phase. All gapped ground states can be smoothly transformed into each other by varying the parameters of the Hamiltonian. (b) Two distinct gapped phases classified by a $\mathbb{Z}_2$ topological invariant. The transition from one phase to the other must go through a quantum phase transition in which the bulk gap vanishes. (c) Many distinct gap phases classified by a $\mathbb{Z}$ (integer) invariant. A transition between any two distinct phases will involve crossing the gapless shaded area.

in Fig. 1.8. The first scenario, panel (a), corresponds to all gapped phases being topologically equivalent, hence belonging to the same phase. In the second, panel (b), the gapped states can be divided into two equivalence classes corresponding to the topological trivial and non-trivial phases, respectively. A topological invariant taking two possible values (called a $\mathbb{Z}_2$ topological invariant) allows us to distinguish the two phases. In the third scenario, there are many distinct topological phases classified by an integer topological invariant (a so-called $\mathbb{Z}$ invariant). Determining which of these three scenarios is realized within each symmetry class and spatial dimension was first carried out independently by Kitaev [35] and by Schnyder , *et al.* [55] using different methods. The results are shown in the right-half of Table 1.2.

As shown in Table 1.2, the realization of a specific scenario depends on i) the symmetry class of the Hamiltonian and ii) the spatial dimension. A blank in columns 6-8 signifies the realization of the first scenario: all gapped ground states belong

to a single phase (the trivial insulator). $\mathbb{Z}_2$ and $\mathbb{Z}$ correspond to the realization of the the other two scenarios. For example, if we consider symmetry class A, there is no topologically nontrivial insulators in one-dimension (1D) and in three-dimensions (3D). By contrast, in 2D there are (infinitely) many topologically distinct ground states characterized by the different values of a $\mathbb{Z}$ (i.e. integer) topological index. Specifically, this topological invariant is the sum of the first Chern numbers corresponding to the occupied bands. The integer quantum Hall states are the best known representatives of these equivalence classes.

Chapter 2

Majorana fermions in topological insulator nanoribbons coupled to superconductors

The classification of different phases of matter based on the entanglement - symmetry - topology paradigm provides us with a the "big picture" represented schematically in fig.(1.6). Most of this territory is still unexplored experimentally. If we focus our attention on non-interacting systems, we can classify the distinct, gapped phases of a matter by considering the topological properties of the filled bands corresponding to Hamiltonians with generic symmetries. Based on this scheme, we have ten symmetry classes of noninteracting Hamiltonians, each class containing one, two, or more topologically-distinct phases, as shown in the classification table of topological insulators and superconductors (1.2). This chapter and the next are devoted to the realization of a particular symmetry class and spatial dimension, more specifically class D in one-dimensional systems. Hamiltonians from this symmetry class support two topologically-distinct phases (a trivial and a topological superconductor), which

are characterized by distinct values of the $\mathbb{Z}_2$ topological invariant.

The interest in studying the one-dimensional (1D) topological superconductors (TSCs) from class D is to realize Majorana fermions in a solid state system. Majorana fermions, which are particles that are identical to their antiparticles, are predicted to emerge naturally in a TSC phase as zero-energy modes localized at the ends of the 1D system. These Majorana zero modes could be used as a platform for topological quantum computation. Unfortunately, there are no (known) intrinsic 1D TSCs. However, there are several types of *heterostructures* proposed for the realization of topological superconductivity and Majorana bound states, in particular, topological insulator (TI) nanowires proximity-coupled to a (conventional) superconductor and semiconductor-superconductor (SM-SC) hybrid structures. A characteristic signature of the Majorana bound state – the emergence at a finite magnetic field of a zero-bias peak in the differential conductance for tunneling into the end of the wire – was recently reported in semiconductor-based structures [48]. However, many experimental features observed in this type of system are not completely understood. Furthermore, no clear signature of Majorana modes was reported so far in TI-based structures. Our goal is to provide a better theoretical understanding of these heterostructures, which could help optimize them. This condition is essential to ensure the unambiguous demonstration of Majorana bound states and to facilitate their robust manipulation, which is a requirement for quantum computation. The investigation starts with the topological insulator-superconductor (TI-SC) system, which is the main topic of this chapter; the SM-SC structure will be discussed in the next chapter.

One key aspect that impacts the stability of a topological superconducting phase is the magnitude of a proximity-induced superconducting gap. In both TI-SC and

SM-SC structures the induced superconducting phase at zero magnetic field is topologically trivial. Applying a magnetic field parallel to the wire/nanoribbon reduces the quasiparticle gap, which vanished at a certain critical field. The vanishing of the quasiparticle gap signals a topological quantum phase transition. At even larger values of the magnetic field the gap reopens and the wire becomes a topologically-nontrivial superconductor. In SM-SC structures, realizing the topological condition at relatively low fields (so that the magnetic field does not destroy the conventional superconducting phase that provides the proximity-induced pairing in the wire) requires fine tunning of the chemical potential. Cook and Franz [15] argued that the TI-based system does not have this (potentially restrictive) disadvantage. The TI-based system was further investigated by Sitthison and Stanescu [58] to better clarify the argument of Cook and Franz. Before going deeper into details related to specific realizations TSC, we briefly summarize the mathematical model that inspired these proposals – the so-called Kitaev chain model. Besides being the first model of a 1D TSC, this is also a good framework for introducing the concept of Majorana fermion.

2.1 Kitaev's toy model

Kitaev's chain model is a theoretical model of major importance in the fields of topological quantum computation, topological superconductivity, and Majorana bound states. It was proposed on a purely mathematical basis as a 1D model for a p-wave superconductor [36]. The model is characterized by the emergence of Majorana modes localized at the ends of the chain. These modes are predicted to obey non-Abelian statistics and were proposed as a possible platform for topological quantum computation. Discussing quantum computation, even at an introductory level, is rather technical and is beyond the purpose of this thesis. However, understanding

the concept of "Majorana fermion" is essential for our subsequent discussion. Hence, we ask, "*what is a Majorana fermion?*".

2.1.1 Getting to know the Majorana fermion

In 1937, Ettore Majorana obtained a real solution to the Dirac's equation for spin$-1/2$ [72]. The consequence of being a real solution is that $\gamma^\dagger = \gamma$, where $\gamma^\dagger$ and γ represent particle creation and annihilation operators, respectively. Note that $\gamma^\dagger$ and γ can be viewed as creation operators for particles and antiparticles, respectively. Hence, the Majorana fermion (MF) is identical to its own antiparticle. Originally, the Majorana fermion was believed to be realized as one of the neutral fundamental particles. One possible candidate suggested by the standard model is the neutrino. However, the experimental evidence concerning the Majorana nature of the neutrino is still incomplete. For example, the detection of neutrino-less double beta decay would provide evidence that neutrino is its own anti-particle [1], but no such detection was reported so far.

Let us recall the key properties of a regular (Dirac) fermion, for example, an electron. In the second quantization descriptions, for a system defined on a lattice, $c_j^\dagger$ represents a creation operator in the Fock space. The operator will create an electron at a lattice site j. On the other hand, c_j represents an annihilation operator. Note that annihilating a (charge $-e$) particle at site j can be viewed as creating a (charge $+e$) hole at that location. Fermi statistics requires the operators to obey the anti-commutation relation $\{c_j^\dagger, c_j^\dagger\} = \{c_j, c_j\} = 0$ and $\{c_i, c_j^\dagger\} = \delta_{ij}$, where the curly bracket denotes the anticommutator, $\{A, B\} = AB + BA$. Note that $c_j^\dagger \neq c_j$, which is equivalent to saying that an ordinary fermion is not its own antiparticle. Hence, the electron is an example of complex fermion represented by non-Hermitian

creation/annihilation operators. Their wave function corresponds to a complex solution of the Dirac equation.

Majorana operators can be expressed mathematically as linear combinations of complex fermion operators, $\gamma_{j1} = (c_j^\dagger + c_j)/2$ and $\gamma_{j2} = (c_j^\dagger - c_j)/2i$. The two Majorana operators γ_{j1} and γ_{j2} obey the fermionic commutation relations. One may think that the mathematical trick of expressing the Majorana operators in terms of complex fermion operators does not yield any new physics. However, the idea of mixing the creation and annihilation operators of the complex fermions suggests that superconductors, which have quasiparticles that are spuerpositions of particles and holes, may be a good place to look for Majorana fermions in condensed matter systems [47]. Thus, the Majorana fermion could be realized as an emergent excitation in a condensed matter system, rather than a fundamental particle.

According to the BCS theory, the ground state of an s-wave superconductor (s-SC) is characterized by the formation of a condensate of singlet pairs. The quasiparticle excitations have finite energy and are represented by quasiparticle operators that can be expressed as $d = uc_\uparrow^\dagger + vc_\downarrow$ and $d^\dagger = v^* c_\downarrow^\dagger + u^* c_\uparrow$, i.e., superpositions of particles and holes. Note that the operators d and $d^\dagger$ are distinct and, consequently, a quasiparticle in an s-SC system is not its own antiparticle, i.e., it is not a MF [4]. Consider now, following Kitaev's proposal, a spinless system. The pairing mechanism cannot involve spin singlets, hence it cannot have s-wave symmetry. However, one can have non-local spinless pairing, which yields p-wave superconductivity (p-SC). One can show that this "exotic" type of superconductivity can realize a topologically nontrivial superconducting phase characterized by the emergence of zero-modes at the boundary. The first experimental evidence consistent with the existence of such Majorana zero-modes was reported in 2012 [48]. The details of this discovery will be

discussed in Chapter 3. But first, let us look at the mathematical model that captures the key physics of a 1D p-wave superconductor, the most promising hunting ground for MF in condensed matter physics.

2.1.2 The toy model

A realization of a one-dimensional p-wave superconductor can be obtained by considering a fully spin-polarized (i.e., *effectively spinless*) fermion system defined on an N-site atomic chain described by a simple tight binding model. With the superconductivity treated at mean-field level, the Hamiltonian has the form

$$H_1 = -\mu \sum_{n=1}^{N} c_n^\dagger c_n - \sum_{n=1}^{N-1} \left(t c_n^\dagger c_{n+1} + \Delta e^{i\phi} c_n c_{n+1} + h.c. \right) \tag{2.1}$$

where

$$\begin{aligned} \mu &= \text{chemical potential,} \\ c_n &= \text{electron annihilation operator at site } n, \\ t &= \text{hopping parameter,} \\ \Delta &= \text{superconducting pairing potential (assumed to be real),} \\ \phi &= \text{superconducting phase.} \end{aligned}$$

Note that for simplicity the superconducting phase, ϕ, can be assumed to be zero without loss of generality. Expressing complex fermion operators in terms of Majorana operators provides an insight into the low-energy physics of the chain. Using

the notations in Ref [42], we have

$$c_n = \frac{1}{2}\left(\gamma_{n,1} + i\gamma_{n,2}\right), \tag{2.2}$$

$$c_n^\dagger = \frac{1}{2}\left(\gamma_{n,1} - i\gamma_{n,2}\right), \tag{2.3}$$

where $\gamma_{n,m}$ represents the Majorana operators of the index site n, and $m = \{1, 2\}$. This expression allows us to keep track of the complex fermion site index easily. Moreover, the "inverse" of Eqs. (2.2) - (2.3) allows us to express the Majorana operators in terms of complex fermion operators,

$$\gamma_{n,1} = c_n^\dagger + c_n \tag{2.4}$$

$$\gamma_{n,2} = i\left(c_n^\dagger - c_n\right). \tag{2.5}$$

Next, let us focus on the the special case characterized by $\Delta = t = 0$ and $\mu < 0$. The 1D atomic chain Hamiltonian in Eq. (2.1) reduces to

$$H_1 = -\mu \sum_{n=1}^{N} c_n^\dagger c_n \tag{2.6}$$

This Hamiltonian describes a topologically trivial state with the total energy of $H = |\mu|N$ corresponding to a collection of N particles localized at the sites of the chain, i.e., an atomic insulator, as illustrated in Fig. (2.1)-a. To realize a topological superconducting state (with the emergent Majorana physics), consider the limit $\Delta = t$ and $\mu = 0$. The Hamiltonian in Eq. (2.1), written in terms of Majorana operators, can be simplified to

$$H = -it \sum_{n=1}^{N-1} \gamma_{n,2}\gamma_{n+1,1}. \tag{2.7}$$

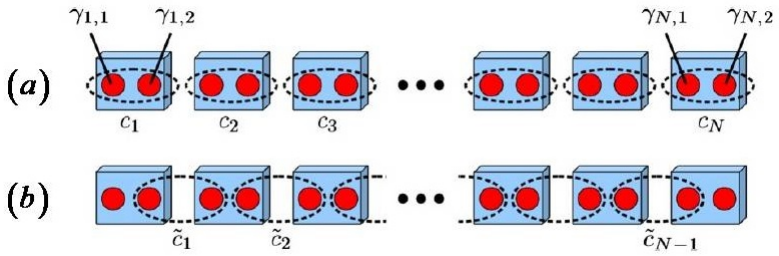

Figure 2.1: From Ref. [42]. A one-dimensional atomic chain realized in, (a) the topological trivial state by setting $\Delta = t = 0$, $\mu < 0$ and (b) the topological non-trivial state by setting $\Delta = t \neq 0$, $\mu = 0$. The blue boxes represent the physical realization of electrons. The red circles represent the physical realization of MFs following the relation $c_n = \frac{1}{2}(\gamma_{n,1} + i\gamma_{n,2})$. In (b), note the unpaired Majoranas localized at the ends of the chain.

The atomic chain is now in a non-trivial topological state, as illustrated schematically in Fig. (2.1)-b. To emphasize the non-triviality of the state and extraordinary nature of MF, let us introduce the new fermion operator,

$$\tilde{c}_n = \frac{(\gamma_{n+1,1} + i\gamma_{n,2})}{2}. \tag{2.8}$$

The Hamiltonian in Eq. (2.7) can be expressed as

$$H = 2t \sum_{i=1}^{N-1} \tilde{c}_i^\dagger \tilde{c}_i. \tag{2.9}$$

The Hamiltonian in Eq. (2.9) resembles the form of a regular atomic chain. The fascinating fact is that the number of atoms in the chain is $N-1$. This is because the Majorana operators $\gamma_{1,1}$ and $\gamma_{N,2}$ are missing from the expression in Eq. (2.9). The Majorana operators $\gamma_{1,1}$ and $\gamma_{N,2}$ correspond to a "regular" fermionic quasiparticle that is spatially localized at both ends of the quantum wire. This can be easily seen

by combining the two Majorana operators into a complex fermion operator

$$\tilde{c}_M = \frac{(\gamma_{N,2} + i\gamma_{1,1})}{2}. \tag{2.10}$$

A fermion associated with the expression in Eq. (2.10) is highly non-local, i.e., an electron occupying the Majorana modes exists at both ends of the wire at the same time. This mode emerges with no energy cost (since the corresponding operators are not present in the Hamiltonian and, therefore, commute with H). This fact can be shown explicitly by assuming that the system ground state is $|\mathcal{G}\rangle$ with energy $E_{\mathcal{G}}$. Since $\gamma_{1,1}$ and $\gamma_{N,2}$ are missing from Eq. (2.6), $[H, \gamma_{1,1}] = [H, \gamma_{N,2}] = 0$. In other words,

$$H\gamma_{1,1}|\mathcal{G}\rangle = E_{\mathcal{G}}\gamma_{1,1}|\mathcal{G}\rangle \tag{2.11}$$

$$H\gamma_{N,2}|\mathcal{G}\rangle = E_{\mathcal{G}}\gamma_{N,2}|\mathcal{G}\rangle\,. \tag{2.12}$$

The Majorana zero-mode bounds to the boundaries of the 1D atomic chain. In a larger context, these Majorana zero modes can be viewed as a particular realization of *gapless boundary modes* characterizing a topologically nontrivial phase, similar to the gapless surface states in topological insulators.

In the standard BCS theory of superconductivity, the ground state consists of an even particle-number state. By contrast, the 1D p-wave superconductor model presented above allows an odd number ground state (for systems with boundaries). The simplest way to characterize the parity of the ground state is by defining the occupation number $n_M = \tilde{c}_M^\dagger \tilde{c}_M$: $n_M = 0$ corresponds to an even-parity state (i.e., the Majorana modes are not occupied), while $n_M = 1$ corresponds to odd parity (the Majorana zero modes are occupied by one electron).

The model parameters discussed above represent two particular cases. In general, an arbitrary set of parameters could correspond to one of the two possible phases: the trivial and the topological superconductor. The topological invariant that uniquely describes these phases is the so-called Majorana number,

$$\mathcal{M} = (-1)^{v}, \tag{2.13}$$

where v is 1 in the topological phase and 0 in the trivial phase. The Kitaev model is a simple and elegant model containing rich physics. The p-wave superconductor seems to be exceedingly rare in nature, yet it can be "engineered" using standard materials, such as semiconductors and conventional superconductors. The real challenge is to physically realize the conditions corresponding to the topological phase predicted by the model.

2.2 The Cook-Franz proposal

One of the proposals for a physical realization of Kitaev's model, made by Cook and Franz [15], is based on a topological insulator nanowire – superconductor hybrid structure. The main discussion of the model follows Ref. [15]. The original theory describing the proposed structure is based on using a generic 3D massive Dirac equation to capture the behavior of the surface states of topological insulators. Guided by the Kitaev's toy model, which shows that breaking time-reversal symmetry is a critical requirement, the Dirac equation was modified to handle an external magnetic perturbation. Explicitly, we have [51],

$$H = \frac{1}{2} v \left[\hbar \vec{\nabla} \cdot \hat{n} + \hat{n} \cdot (\vec{p} \times \vec{\sigma}) + (\vec{p} \times \vec{\sigma}) \cdot \hat{n} \right] \tag{2.14}$$

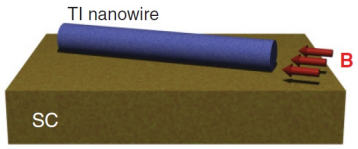

Figure 2.2: The TI-nanowire – superconductor setup proposed by Cook and Franz [15]. The TI (e.g., Bi_2Se_3) nanowire with the circular cross section is placed on top of an ordinary superconductor. A magnetic field is applied parallel to th wire to ensure the removal of spin degeneracy at $k = 0$.

where

$$\begin{aligned} \vec{p} &= \text{tcanonical momentum}, -i\hbar\vec{\nabla}, \\ v &= \text{Dirac velocity}, \\ \hat{n} &= \text{unit vector normal to the surface}, (\cos\varphi, \sin\varphi, 0), \\ \vec{s} &= \text{Pauli matrices in spin space}. \end{aligned}$$

In the presence of an external magnetic field, the canonical momentum changes into $\vec{p} \to \vec{p} - \left(\frac{e}{c}\right)\vec{A}$, where $\vec{A}$ is the vector potential. For this particular study, the vector potential corresponding to a magnetic field parallel to the cylindrical wire will be expressed as $\vec{A} = \eta\frac{\Phi_0(\hat{z}\times\vec{r})}{2\pi r^2}$, where η is a dimensionless factor and Φ_0 is the magnetic flux quantum. The total magnetic flux through the wire is $\Phi = \eta\Phi_0$.

The model takes advantage of the strong spin-orbit interaction in the TI wire, where the surface-like states can be considered as a fully spin-polarized system. The external magnetic field is applied longitudinally to lift the double degeneracy of the wire spectrum, as shown in Fig. 2.3. The wire is put into contact with an s-SC, so that it becomes a superconductor by proximity effect. The heterostructure is shown schematically in Fig. 2.2

Ideally, the TI nanowire can be consider a perfect 1D system. According to Ta-

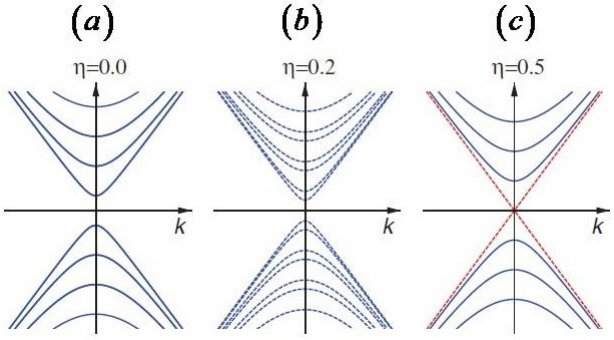

Figure 2.3: Energy spectrum of the TI surface-like states with varying amount of magnetic flux applied longitudinally to the wire. The solid blue lines show the spin degenerate band while the blue dashed lines represent the bands with spin degeneracy lifted. (a) At $\eta = 0.0$, external magnetic field is zero. Every energy band is doubly degenerate. (b) At $\eta = 0.2$, the presence of an external magnetic field induces a lifting of the degeneracy. (c) At $\eta = 0.5$, half-flux quantum, an odd number of pairs of Fermi points is realized for arbitrary values of the chemical potential. (From Ref [15])

ble (1.2), there is no topological distinction among the ground state wave functions of 1D structure in class AII. In other words, a wire made of TI material is in a topologically trivial phase, which is signaled by the fact that its spectrum is always gapped. However, in the presence of induced superconducting correlations the system has particle-hole symmetry and, therefore, belongs to symmetry class D. Note that symmetry class D requires breaking of TRS, which can be achieved by applying an external magnetic field. More physically, the role of the magnetic field is to remove spin degeneracy, thus providing the possibility of having an odd number of pairs of Fermi points (see Fig. 2.3). Note that one pair corresponds to an effectively spinless system, the requirement for realizing a p-wave superconducting state. One can show that for multi-band systems this condition generalizes to having an odd number of bands (partially) occupied. Tuning of the magnetic field strength is critical. According to the calculation, the critical value of the magnetic flux passed through the wire is $\Phi = 0.5\Phi_0$ where Φ_0 is the flux quantum.

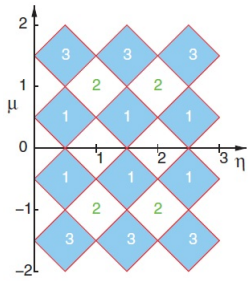

Figure 2.4: Topological phase diagram. The number within each box represents the number ν of bands crossed by the chemical potential. The odd numbers correspond to a topologically non-trivial phase, also indicated by a shaded area. (From Ref. [15].)

An interesting result is the topological phase diagram. Although the main ingredients to realize the topological superconducting phase are present (i.e., strong spin-orbit coupling and magnetic field to engineer effectively spinless fermions, plus proximity-induced superconductivity), there is another parameter that needs special attention: the chemical potential, μ_{TI}. Note that, theoretically, the realization of the non-trivial phase is signaled by topological invariant, i.e., the Majorana number $\mathcal{M} = (-1)^v$. In the limit of weak TI-superconductor coupling, v coincides with the number of Fermi points for $k > 0$, which can be determined directly by counting the number of bands crossing the chemical potential. The $\mathcal{M} = -1(1)$ refers to the non-trivial(trivial) topological phase. In the non-trivial phase, a pair of Majorana bound states will naturally emerge at the ends of the nanowire, as illustrated in Fig. 2.1-b. The topological phase diagram is shown in Fig. 2.4.

The non-trivial phase exhibits periodicity in both chemical potential and external magnetic field. The behavior illustrated in Fig. 2.4 leads to a very important claim: *fixing the strength of external magnetic field to half flux quantum* (i.e., $\eta = 0.5$), *the non-trivial topological superconducting phase can always be realized regardless of the value of the chemical potential*. Eq. (2.14), which captures only the behavior of the

surface-like states, describes a possible large range to realize the TSC, a range comparable with the bulk gap of Bi_2Se_3. If this claim were true, the TI-based structure would have a significant advantage over the semiconductor-based alternative, which require fine-tuning of the chemical potential.

The formal derivation of this result starts with Eq. (2.14) expressed as the Bogoliubov-de Gennes Hamiltonian,

$$H_1(k) = (k\sigma_y - \mu_{TI} + m\sigma_z)\tau_z - \Delta\tau_y\sigma_y \tag{2.15}$$

where τ_α and σ_α are the Pauli matrix in particle-hole space and in spin space, respectively. Note that v and $\hbar$ are set to be unity. When the magnetic field takes a value corresponding to half flux quantum, we have $m = 0$ and the energy spectrum becomes

$$E_k = \pm\sqrt{(k \pm \mu)^2 + \Delta_0^2} \tag{2.16}$$

Note that, regardless of μ, the quasiparticle gap is finite, signaling the fact that the system does not cross any phase transition. In other words, the non-zero value of the gap indicates the robustness of the topological phase.

To confirm the results based on the idealized Dirac equation approach, one can carry out a lattice model calculation to better capture the robustness of the topological phase. The effective Hamiltonian is [75],

$$h_k = M_k r_1 + \lambda r_3(\sigma_2 \sin k_x - \sigma_1) + \lambda_z r_2 \sin k_z \tag{2.17}$$

where $M_k = \varepsilon - 2t\sum_\alpha \cos k_\alpha$ and r_α is the Pauli matrix in the orbital space. The Hamiltonian incorporates the external magnetic field through the orbital effect de-

scribed by the Peierls' substitution,

$$t_{ij} \rightarrow t_{ij} e^{-\left(\frac{2\pi i}{\Phi_0}\right) \int_i^i \vec{A} \cdot d\vec{l}}. \tag{2.18}$$

The contribution from the Zeeman effect is expected to be small and is neglected. Note that the lattice model includes contributions coming from bulk-like state. Using this model it was found that the special value of the magnetic flux that guarantees the realization on the topological phase for a large range of chemical potentials is not exactly at the half flux quantum but vary slightly. This is due to the finite "thickness" of the surface-like states, "feel" a smaller effective magnetic flux. Nonetheless, the main conclusion concerning the robustness of the topological phases was confirmed. This motivates an even deeper critical analysis of the main assumptions behind this result, which is discussed in the next section.

2.3 Topological Superconductivity in Topological Insulator-Based Hybrid Structures

One of the attempts to realize Majorana bound states in solid states system focuses on the proximity-induced superconductivity obtained by coupling topological insulator materials and ordinary superconductors. Such a structure is predicted to host p-wave superconductivity. Moreover, in such system one expects the emergence of Majorana quasiparticles localized at the boundaries of the system or bounded to topological defects (such as 1D domain walls or vortices in two-dimensional systems). Of special interest are the zero-energy Majorana modes bound to the ends of a 1D wire or to the vortex cores of a 2D superconductor. We will call them *Majorana bound states* (MBS) or *Majorana zero modes* (MZM). Note that a topological defect

carrying a Majorana zero mode obeys non-Abelian statistics, hence its significance in the context of quantum computation. Therefore, a MZM is not exactly a "fermion", in the sense that it does not obey fermionic statistics. However, in the literature it is sometimes referred to as a *Majorana fermion* (MF). Below, we always assume that MF actually designates a MZM/MBS.

Several theoretical studies [15, 16, 22] have explored the possibility of realizing MBSs in TI-based systems. The superconducting proximity effect has been explicitly addressed by Sitthison and Stanescu [58]. The robustness of the topological phase is critically reconsidered using the tight binding formalism from Ref. [30], which is based on the $k \cdot p$ calculation of Zhang *et al.,* [75], and explicitly taking into account the superconducting proximity effect, as well as electrostatic effects due to the presence of substrates and gate voltages.

2.3.1 Model Hamiltonian for a Topological Superconductor

The Hamiltonian of a topological superconductor consists of several parts. The first ingredient is the model Hamiltonian for TI, e.g., Bi_2Se_3, which can be defined on a lattice. This Hamiltonian also includes the contribution of an electrostatic field, which includes the external perturbation due to gate potentials and the interfaced-induced potential. The second ingredient is an external magnetic field that is incorporated through the Peierls substitution to capture the orbital effect. The last component is the superconducting proximity effect, which is introduced as an interface self-energy contribution to the Green function of the wire.

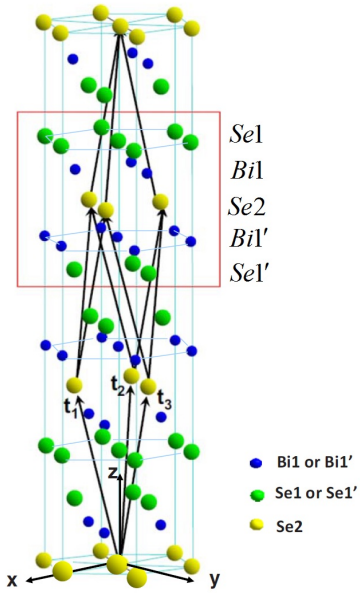

Figure 2.5: Rhombohedral unit cell of Bi_2Se_3 with three primitive lattice vectors: $\vec{t}_1 = \left(-\frac{a}{2}, -\frac{\sqrt{3}a}{6}, \frac{c}{3}\right)$, $\vec{t}_2 = \left(\frac{a}{2}, -\frac{\sqrt{3}a}{6}, \frac{c}{3}\right)$, $\vec{t}_3 = \left(0, \frac{\sqrt{3}a}{3}, \frac{c}{3}\right)$ where (a, c) are the lattice parameter with the values $(4.138\text{Å}, 28.64\text{Å})$ respectively. In the box there is a quintuple layer consisting with five-atomic layers denoted as $Se1 - Bi1 - Se2 - Bi1' - Se1'$. (From Ref. [77])

Low-energy effective Hamiltonian of the TI nanoribbon

The topological insulator Bi_2Se_3 has a well-defined bulk gap and robust surface states. Its possible gapped phases are characterized by $\mathbb{Z}_2$ topological index. The bulk gap is about 0.3 eV, larger than the gap of another Bi-based TI, the Bi_2Te_3, which has bulk gap of about 0.21 eV. The relatively large bulk gap makes Bi_2Se_3 an ideal material for engineering a robust topological superconducting state. Moreover, the energy band structure of Bi_2Se_3 is very simple, providing a low computational cost for accurate predictions. By comparison, the first 3D TI material discovered, the $Bi_{1-x}Sb_x$, has a more complicated energy band structure [76].

The Bi_2Se_3 has a layered structure with an alternation of covalent and van der Waals-type bonding. The five atomic layers strongly bounded together form a so-

called *quintuple layer* (QL) [77]. The QL consisting of $...-Se-Bi-Se-Bi-Se-...$, as shown in Fig. 2.5, can be viewed as $...-A-B-C-A-B-...$ staking. The bonding between the QLs is governed by van der Waals interactions. Since the QL can be used as a unit cell, connecting the Se at the center of each QL reveals a rhombohedral structure with a space group $D_{3d}^5(R\bar{3}m)$. The $Se2$ in the middle acts as a center of inversion. The inversion operator switches $Se1 \leftrightarrow Se1'$ and $Bi1 \leftrightarrow Bi1'$ and the presence of inversion symmetry allows the system to have definite parity eigenstates.

The low-energy band structure of Bi_2Se_3 can be constructed by considering the p-orbitals of Bi and Se. The total orbital degree of freedom produces a 15-band model, with 3 p-orbitals from each of the five atomic layers within the QL. By including the hybridization among the Bi and Se orbitals, the inversion symmetry of the QL, the crystal field splitting, and the spin-orbit coupling, the valence electron states of Bi and Se become mixed together. Thus, the effective low energy Hamiltonian can be obtained by taking into account only the states that are closest to the chemical potential. In the vicinity of $k = 0$ the low-lying states can be constructed as [43]

$$\begin{aligned} |\lambda, \uparrow\rangle &= u_\lambda \, |\lambda, p_z, \uparrow\rangle + v_f \, |\lambda, p_+, \downarrow\rangle \,, \\ |\lambda, \downarrow\rangle &= u_\lambda^* \, |\lambda, p_z, \downarrow\rangle + v_\lambda^* \, |\lambda, p_-, \uparrow\rangle \,, \end{aligned} \tag{2.19}$$

where $\lambda = \pm 1$ represents the parity, $p_\pm = p_x \pm p_y$, and u_λ, v_λ, with $|u_\lambda|^2 + |v_\lambda|^2 = 1$, are coefficients that depend on the spin-orbit coupling strength and will be treated as model parameters.

The resulting states, $|\lambda, \sigma\rangle$, have parity λ, while σ labels the total angular momentum along z-direction with eigenvalues $\frac{\sigma\hbar}{2}$. Note that the states $|\lambda, \sigma\rangle$ extend across a QL and can be viewed as molecular orbitals. The resulting states, $\{|+, \uparrow\rangle, |-, \uparrow\rangle, |+, \downarrow\rangle, |-, \downarrow\rangle\}$, form the basis for a four-band tight-binding model.

The corresponding effective low-energy tight binding Hamiltonian is given by [30]

$$H_{TI} = \sum_{\lambda,i,j} \left(\varepsilon_0^{(\alpha)} \delta_{ij} + t_{ij}^{(\alpha)} \right) c_{i\lambda}^{\dagger} c_{j\lambda} + i\alpha_{ij} c_{i\lambda}^{\dagger} \left(\vec{\boldsymbol{\delta}} \cdot \vec{\boldsymbol{\sigma}} \right) c_{j\bar{\lambda}} \tag{2.20}$$

where

$\alpha, \bar{\alpha}$ = band index, with $\alpha \neq \bar{\alpha}$,

i, j = the lattice site index,

$c_{i\lambda}^{\dagger}$ = $\left(c_{i\lambda\uparrow}^{\dagger}, c_{i\lambda\downarrow}^{\dagger} \right)$, the creation operator,

$\vec{\boldsymbol{\sigma}}$ = $(\sigma_x, \sigma_y, \sigma_z)$, the Pauli matrix in spin space,

$\vec{\boldsymbol{\delta}}_{ij}$ = $(\vec{r}_j - \vec{r}_i)/a$, the next nearest neighbor vector scaled by the lattice constant, a,

$t_{ij}^{(\lambda)}$ = $(t_{1\lambda}, t_{2\lambda})$, the next nearest neighbor hopping for in-plane and out-of-plane respectively,

α_{ij} = (α_1, α_2), the spin- and direction-dependent interband hopping
for in-plane and out-of-plane respectively.

The effective parameters can be determined by matching the long-wavelength spectrum of the tight-binding model and the the continuum model of Zhang *et al.,* [75], which has the same basis set and is obtained within the $k \cdot p$ theory in the $k \to 0$ limit. An explicit expression of the continuum model Hamiltonian is given by,

$$H(k) = \epsilon_0(k) I_{4\times 4} + \begin{pmatrix} \mathcal{M}(k) & A_1 k_z & 0 & A_2 k_- \\ A_1 k_z & -\mathcal{M}(k) & A_2 k_- & 0 \\ 0 & A_2 k_+ & \mathcal{M}(k) & -A_1 k_z \\ A_2 k_+ & 0 & -A_1 k_z & -\mathcal{M}(k) \end{pmatrix} + o\left(k^2\right), \tag{2.21}$$

where

$$\begin{aligned} k_{\pm} &= k_x \pm ik_y, \\ \epsilon_0(k) &= C + D_1 k_z^2 + D_2 k_{\perp}^2, \\ \mathcal{M}(k) &= M - B_1 k_z^2 - B_2 k_{\perp}^2. \end{aligned}$$

In turn, the parameters of the continuum model were obtained by fitting the energy bands obtained using an *ab initio* calculation. We have [75] $M = 0.28eV, A_1 = 2.2eV\text{Å}, A_2 = 4.1eV\text{Å}, B_1 = 10eV\text{Å}^2, B_2 = 56.6eV\text{Å}^2, C = -0.0068eV, D_1 = 1.3eV\text{Å}^2, D_2 = 19.6eV\text{Å}^2$. The parameters of the tight binding Hamiltonian in Eq. (2.20) are related to those of the $k \cdot p$ Hamiltonian in Eq. (2.21) as follows

$$\varepsilon_{\pm} = C_0 \pm M_0 + \frac{12}{c^2}(C_1 \pm M_1) + \frac{4}{a^2}(C_2 \pm M_2), \tag{2.22}$$

$$t_{1\pm} = -\frac{3}{c^2}(C_1 \pm M_1), \tag{2.23}$$

$$t_{2\pm} = \frac{1}{c^2}(C_1 \pm M_1) - \frac{2}{3a^2}(C_2 \pm M_2), \tag{2.24}$$

$$\alpha_1 = \frac{3}{2}\frac{aA_1}{c^2}, \tag{2.25}$$

$$\alpha_2 = \frac{A_2}{3a} - \frac{aA_1}{2c^2}. \tag{2.26}$$

For convenience, the electrostatic effect is combined with the chemical potential term, both representing local contributions. The Hamiltonian that describes the electrostatic effect and the chemical potential can be expressed as

$$H_v = \sum_{i,\lambda} \left[V(i) - \mu_{TI}\right] c_{i\lambda}^{\dagger} c_{i\lambda}, \tag{2.27}$$

where $V(i)$ is a position-dependent effective electrostatic potential. This electrostatic

potential accounts for the contribution of an external gate potential and that of the interface-induced potential.

Magnetic field

The magnetic field is necessary to ensure the odd number of pairs of Fermi points, i.e. the condition for having an effectively spinless system. In the presence of the TRS, Kramer theorem protects the degeneracy at Γ, ($k = 0$). Generally, an external magnetic field breaks the TRS and lifts the degeneracy. The Hamiltonian for an electron in magnetic field is [14]

$$H_{\vec{B}} = -\frac{\mu_B}{\hbar}\left(g_L\hat{L} + g_S\hat{S}\right)\cdot\vec{B}, \tag{2.28}$$

where μ_B is the Bohr magneton and g_L, g_S are the g-factors for total orbital momentum and spin, respectively. The first term is the orbital contribution of an external magnetic field, while the interaction with the spin is described by the Zeeman splitting (the second term). Note that the relative strengths of the two terms in TI- and SM-based heterostructures are completely different. Since the g-factor in TIs is relatively small, the Zeeman term is negligible in the TI-based system, as compared with the orbital effect. By contrast, in semiconductor wires g can be very large (e.g., $g \approx 50$ in InSb wires) and the Zeeman term is dominant. To incorporate the orbital effect one can use the Peierls substitution [28], which can be expressed in the tight-binding formalism as [21, 46]

$$t_{mn} \Rightarrow t_{mn}e^{-i\frac{e}{\hbar}\vec{A}\cdot\vec{\delta}} \Rightarrow t_{mn}e^{-i\frac{e}{\hbar}\int_{r_n}^{r_m} d\vec{r}\cdot\vec{A}(\vec{r},t)}, \tag{2.29}$$

where t_{mn} represents the matrix element $t_{ij}^{(\lambda)}$ or α_{ij} in the tight binding Hamiltonian (2.20) and $\vec{A}$ is the magnetic vector potential.

Proximity effect

Despite being a key ingredient, proximity-induced superconductivity was not investigated in any detail in the original proposal. Instead, it was simply assumed that the TI Hamiltonian acquires a pairing term. The proximity effect induces superconductivity in the TI-nanowire by coupling it to an s-wave superconductor. Whether the induced superconductivity is topologically trivial or nontrivial depends on the value of the magnetic field. It is rather remarkable that an exotic pairing mechanism can be engineered using an "ordinary" superconductor. In this approach, the s-wave superconductor will be treated at a mean-field level and modeled by the tight binding Hamiltonian

$$H_{SC} = \sum_{i,j,\sigma} \left(t_{ij}^{SC} - \mu_{SC}\delta_{ij} \right) a_{i\sigma}^{\dagger} a_{j\sigma} + \Delta_0 \sum_{i} \left(a_{i\uparrow}^{\dagger} a_{i\downarrow}^{\dagger} + a_{i\downarrow} a_{i\uparrow} \right) \tag{2.30}$$

where

$a_{i\sigma}^{\dagger}$ = the creation operator for a state localized at lattice site i with spin σ,

μ_{SC} = the chemical potential of the superconductor,

t_{ij}^{SC} = the next nearest neighbor hopping parameter,

Δ_0 = the local pairing amplitude (set to 1.5 meV throughout this study).

Intuitively, the superconducting proximity effect can be understood in terms of states from the wire liking into the bulk SC across the TI-SC interface. Consequently, electrons from TI-nanowire spend part of their time into superconductor and acquire

pairing correlations. To capture this physics, the TI and SC Hamiltonians have to be coupled. The term that describes the coupling between the two materials has the form

$$H_{TI-SC} = \sum_{i_0,j_0} \sum_{\lambda\sigma} \left(\tilde{t}_{\lambda\sigma} c^{\dagger}_{i_0\lambda\sigma} a_{j_0\sigma} + \text{H.c.} \right) \tag{2.31}$$

where

$$\begin{aligned} i_0 &= \text{site at the interface in the TI region,} \\ j_0 &= \text{site at the interface in the SC region,} \\ \tilde{t}_{\lambda\sigma} &= \text{coupling constants that depend on spin and orbital labels.} \end{aligned}$$

The basis set used in the TI Hamiltonian explicitly contains a p_z component. This component will couple strongly with SC states across the interface. By contrast, the $p_{\pm}$ components will couple weakly because of the alternating sign of the different lobes. To obtain the coupling matrix between TI and SC, three majors assumptions are introduced, which will greatly simplifies the calculation:

- perfect lattice matching across the interface,
- $|\lambda, p_z, \sigma\rangle$ is the only state having nonzero coupling matrix element with the SC,
- the hopping across the interface is independent of the spin orientation.

These assumptions lead to a coupling matrix of the form

$$\tilde{t}_{\lambda\sigma} = \delta_{\sigma,\sigma'} \begin{pmatrix} \tilde{t}_+ & 0 \\ \tilde{t}_- & 0 \\ 0 & \tilde{t}_+ \\ 0 & \tilde{t}_- \end{pmatrix}_{\lambda\sigma,\sigma'} . \tag{2.32}$$

Instead of treating $\tilde{t}_+$ and $\tilde{t}_-$ as unknown parameters, it is more convenient to have the relative strength $\xi = \frac{\tilde{t}_-}{\tilde{t}_+}$ and the "total" strength $\sqrt{\tilde{t}_+^2 + \tilde{t}_-^2}$ as independent model parameters.

The superconductor can be considered as a charge reservoir. Also, within a Green function formalism we can integrate out the superconducting degrees of freedom. As a result, the bulk SC will enter to the effective low-energy theory of the TI subsystem as a surface self-energy term [58, 42, 61]. Since the relevant physics happens at the low-energy and long wavelengths, a further approximation can be made: the Green's function of the superconductor can be approximated as a purely local contribution. Thus, the surface superconductor self-energy term can be expressed as

$$\Sigma_{\lambda\sigma,\lambda'\sigma'}(\omega; i_0) = \tilde{t}_{\lambda\sigma} G^{SC}_{\sigma,\sigma'}(\omega; j_0)\, \tilde{t}_{\lambda'\sigma'}, \tag{2.33}$$

where (i_0, j_0) is a pair of a nearest neighboring site across the TI-SC interface. For a planar interface the local contribution is independent of position. Thus, the SC Green's function can be expressed as

$$G^{SC}(\omega) = -\nu_F \left[\frac{\omega + \Delta_0 \sigma_y \tau_y}{\sqrt{\Delta_0^2 - \omega^2}} + \varsigma \tau_z \right], \tag{2.34}$$

where

σ_α = Pauli matrices in the spin space,

τ_α = Pauli matrices in the particle-hole space,

ν_F = surface density of states for the bulk SC in the normal phase at the Fermi energy,
$= \frac{1}{|t^{SC}|}\sqrt{1 - \left(1 - \frac{\mu_{SC}}{2t^{SC}}\right)^2}$,

$\varsigma\tau_z$ = a proximity-induced bias potential at the interface, which is included in H_v.

If we focus on the low-energy physics characterized by $|\omega| \ll \Delta_0$, the superconducting proximity effect can be treated within the *static approximation*, $\sqrt{\Delta_0^2 - \omega^2} \approx \Delta_0$. This approximation provides an accurate description of the low-energy spectrum up to about $0.4\Delta_0$ [60].

The low-energy eigenvalues of the proximity-coupled TI subsystem can be obtained by solving the Bogoliubov-de Genned(BdG) equation,

$$\det\left[G_{TI}^{-1}(\omega)\right] = 0 \tag{2.35}$$

with the TI Green's function expressed as

$$G_{TI}(\omega) = \left[\omega - \bar{H}_{TI} - \bar{H}_v - \bar{H}_z - \Sigma(\omega)\right]^{-1}, \tag{2.36}$$

where

$\bar{H}_{TI}$ = Hamiltonian of the TI nanoribbon,

$\bar{H}_v$ = Hamiltonian describing the electrostatic effect,

$\bar{H}_z$ = Hamiltonian describing the magnetic orbital effect.

The structure of BdG Hamiltonians in Eq. (2.36) is

$$\bar{H}_X = \begin{pmatrix} H_X & 0 \\ 0 & -H_X^T \end{pmatrix} \tag{2.37}$$

where $X = TI, v, z$. Focusing on the self energy term, within the approximations discussed above we have

$$\Sigma = -\frac{\gamma}{\Delta_o}\left[\omega\left(I \otimes M_0\left(\xi\right) \otimes \hat{K}\right) + i\Delta_o\left(\tau_y \otimes M_1\left(\xi\right) \otimes \hat{K}\right)\right] \tag{2.38}$$

where

$$\begin{aligned}
\gamma &= \left(\tilde{t}_+^2 + \tilde{t}_-^2\right)\nu_F, \text{the effective coupling strength at the TI-SC interface,} \\
\hat{K} &= \text{interface matrix with elements 1 for sites at the interface and 0 otherwise,} \\
M_0(\xi) &= \text{proximity-induced normal self-energy corrections,} \\
M_1(\xi) &= \text{proximity-induced anomalous self-energy corrections.}
\end{aligned}$$

Note that $M_0\left(\xi\right)$ and $M_1\left(\xi\right)$ have the following explicit forms

$$M_0\left(\xi\right) = \frac{1}{1+\xi^2}\begin{pmatrix} 1 & \xi & 0 & 0 \\ \xi & \xi^2 & 0 & 0 \\ 0 & 0 & 1 & \xi \\ 0 & 0 & \xi & \xi^2 \end{pmatrix}, \tag{2.39}$$

$$M_1\left(\xi\right) = \frac{1}{1+\xi^2}\begin{pmatrix} 0 & 0 & -1 & -\xi \\ 0 & 0 & -\xi & -\xi^2 \\ 1 & \xi & 0 & 0 \\ \xi & \xi^2 & 0 & 0 \end{pmatrix}. \tag{2.40}$$

Putting together all these ingredients, the Green's function of the TI subsystem becomes

$$G_{TI}\left(\omega\right) = \omega\left(1 + \frac{\gamma}{\Delta_o} I \otimes M_0\left(\xi\right) \otimes \hat{K}\right) - \bar{H}_X + i\Delta_o\left(\tau_y \otimes M_1\left(\xi\right) \otimes \hat{K}\right). \tag{2.41}$$

Next, we introduce the "renormalization matrix"

$$\tilde{Z} = 1 - \hat{K} + \frac{1}{\sqrt{1+\xi^2}} \begin{pmatrix} \beta & \beta\xi & 0 & 0 \\ -\xi & 1 & 0 & 0 \\ 0 & 0 & \beta & \beta\xi \\ 0 & 0 & -\xi & 1 \end{pmatrix} \tag{2.42}$$

where $\beta = \frac{1}{\sqrt{1+\frac{\gamma}{\Delta_0}}}$. $\tilde{Z}$ maps the first term of the TI Green's function in Eq. (2.41), i.e., the matrix multiplying ω, to the unit matrix:

$$\tilde{Z}\left[1 + \frac{\gamma}{\Delta_0} I \otimes M_0(\xi) \otimes \hat{K}\right] \tilde{Z}^T = 1. \tag{2.43}$$

Consequently, the BdG equation can be rewritten as an eigenvalue problem corresponding to an effective low-energy Hamiltonian,

$$\det\left[\omega - H_{eff}\right] = 0 \tag{2.44}$$

where

$$H_{eff} = \tilde{Z}\left[\bar{H}_{TI} + \bar{H}_V + \bar{H}_Z\right]\tilde{Z}^T + i\tau_y \begin{pmatrix} \Delta_{ind} & 0 \\ 0 & 0 \end{pmatrix} \hat{K} \tag{2.45}$$

with

$$\Delta_{ind} = \frac{\gamma\Delta_0}{(\gamma + \Delta_0)}$$

Solving Eq. (2.44) is equivalent to finding the eigenvalues of the effective Hamiltonian (2.45). The solution captures the low-energy physics of a TI nanoribbon proximity coupled to ordinary s-wave superconductors. This effective Hamiltonian will be used throughout the remainder of this chapter.

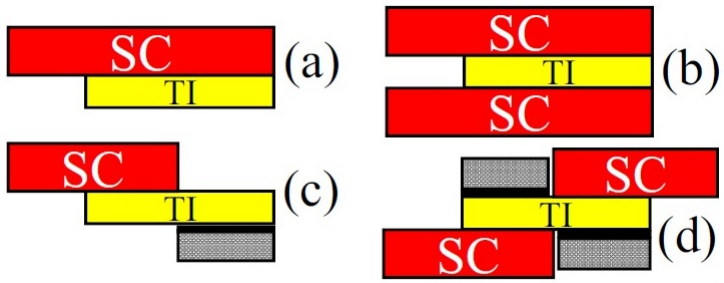

Figure 2.6: Cross section view of the setups that will be discussed in this study. The TI-nanoribbons, the s-wave superconductors, and the potential gates are shown in yellow, red, and gray respectively. (From Ref. [58])

2.3.2 Numerical study of superconducting TI nanoribbons

Equipped with the mathematical model that was introduced above, let us discuss the results of the numerical diagonalization of H_{eff} corresponding to several different situations. The main ingredients to realize a TSC are the TI-nanoribbon, the gate potential, the magnetic field, and the conventinal s-SC. There are numerous ways to put them together. The discussion below concerns the specific setups shown in Fig. 2.6. The TI-nanoribbons assumed to be infinitely long in the y-direction (i.e., perpendicular to the page in Fig. 2.6). The ribbon cross section has dimensions described by $(L_z, L_x) = \left(\frac{N_z c}{3}, N_x a\right)$, where N_z is an integer representing the number of the QLs, while N_x indicates the width of the ribbon; a and c are the lattice constant. In this study, the dimensions are chosen to be 60×9.5nm, unless otherwise stated. We will map out the phase diagram of the system, studying the dependence of the phase boundaries on the control parameters. This pave the way to identifying the optimization condition that maximizes a stability of the topological superconducting phase. Maximizing the proximity-induced gap is the key element that determines the stability of the TSC and the robustness of the Majorana zero mode.

Spectrum and low-energy state

The basic properties of the model Hamiltonian will be discussed in following sections. The energy spectrum of a bare TI-nanoribbon will be presented first. The energy dispersion in the presence of an electrostatic field is also discussed. Next, we will include the SC proximity-coupling. At the time of writing this thesis, there are no experimental results that could test the validity of the effective low-energy theory.

Normal state of TI-nanoribbons. Since the parameters of tight binding model were obtained using a fitting procedure, they are not unique. There are different sets of parameters that can generate similar low-energy dispersion. Experimental results using angle-resolved photoemission spectroscopy (ARPES) measurements on Bi_2Se_3 thin films can be used as a benchmark in the 2D case. The parameters employed in the study are obtained by initially assigning values corresponding to those used by H. Zhang *et al.* [75] and later optimizing them by comparison with first-principle calculations by W. Zhang *et al.* [77]. Note that the initial parameters are for a 3D TI, which may not guarantee that they are optimal for the low-dimensional cases. The final parameters show good agreement with the band structure of Bi_2Se_3 revealed by the ARPES measurement, as shown in Fig. 2.7.

The main physics, which the model is able to capture, is the appearance of the gapless surface state at the thickness of 6 QL, as shown in Fig. 2.7-a. More importantly, when an electrostatic field is turned on (see the 3 QL case), the band structure shows a Rashba-type splitting. As pointed out in Ref.[78], this effect can be caused by a substrate-induced asymmetric potential profile. The appearance of this effective spin-orbit coupling (SOC) cannot be easily obtained from first-principle calculations, due to the symmetry of the structure implicitly assumed in the formal-

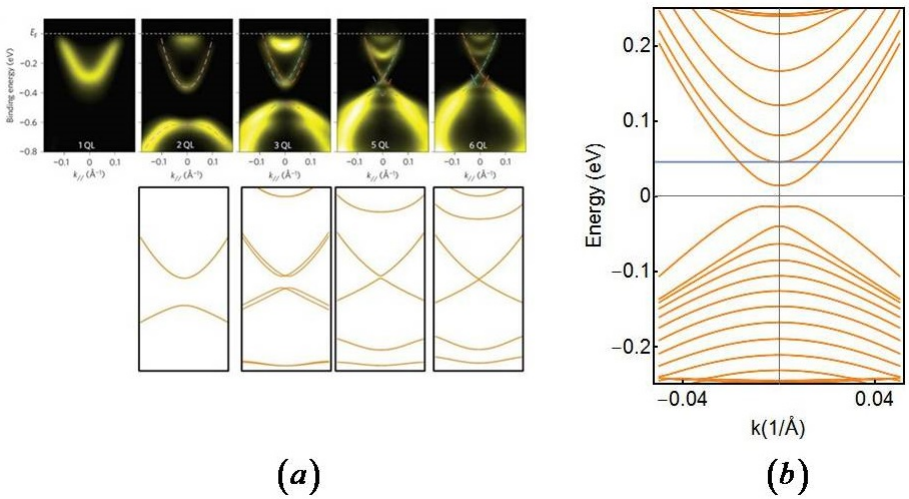

Figure 2.7: (a) Comparison of the band structure dependence on the TI-film thickness obtained by (a-top) ARPES measurements [78] and by (a-bottom) tight binding calculations using the Hamiltonian in Eq. (2.20) with parameters $\{t_{1a}, t_{1b}, t_{2a}, t_{2b}, \lambda_1, \lambda_2, \varepsilon_{0a}, \varepsilon_{0b}\}$={ 0.15, −0.47, 0.62, −0.08, 0.08, 0.16, −1.02, 2.99 }. Note that the result of the calculation includes the electrostatic effect in the case of a 3 QL. (b) Band structure of TI-nanoribbons without any external perturbation.

ism. However, a good agreement of the model calculations with the experimental results validates the effective low-energy model and demonstrates the important role of the electrostatic term.

The optimized parameters are employed in the 1D case to construct a Hamiltonian for the TI-nanoribbon. To obtain an odd number of Fermi points, a longitudinal magnetic field is required. A magnetic flux with a value around half flux quantum is expected to induce a Dirac cone-like (gapless) band dispersion. The evolution of the 1D energy spectrum with the applied magnetic field is illustrated in Fig. 2.8. Panel (c) shows that the energy spectrum of the TI-nanoribbon becomes gapless for an external magnetic flux $\Phi = 0.583\Phi_0$. This critical value of the magnetic flux is remarkable, since for an arbitrary value of the chemical potential (inside the bulk gap) the number of pairs of Fermi points $\left\{-k_F^{(n)}, k_F^{(n)}\right\}$ is always odd. This confirms

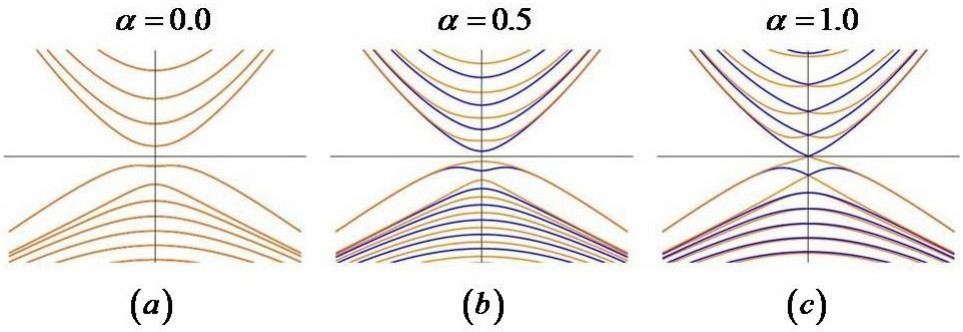

Figure 2.8: Energy band dispersion for different values of the magnetic flux, $\Phi = \alpha \times 0.583\Phi_0$. (a) No external magnetic field. (b) External magnetic field with a flux $\Phi = 0.5 \times 0.583\Phi_0$. (c) $\Phi = 0.583\Phi_0$.

the original claim that for special values of the magnetic field the topological phase can be realized without fine-tuning the chemical potential.

To explore the effect of an electrostatic field on the TI-nanoribbon, consider a linear position-dependent potential of the form

$$V(i) = \frac{V_{\max}}{2}\left(i_z - \frac{N_z + 1}{2}\right) \tag{2.46}$$

where

$$\begin{aligned} i &= (i_x, i_y, i_z), \text{the position of a lattice site,} \\ N_z &= \text{the number of quintuple layers,} \\ V_{\max} &= \text{the potential difference between the top and bottom surfaces.} \end{aligned}$$

Note again that the potential in Eq. (2.46) represents the overall effect due to external gate potentials and interface-induced biases. In the absence of the external magnetic field, the contribution of the electrostatic potential is illustrated in Fig. 2.9)-b. It is reasonable to argue that the profile of $V(i)$ is only marginally signifi-

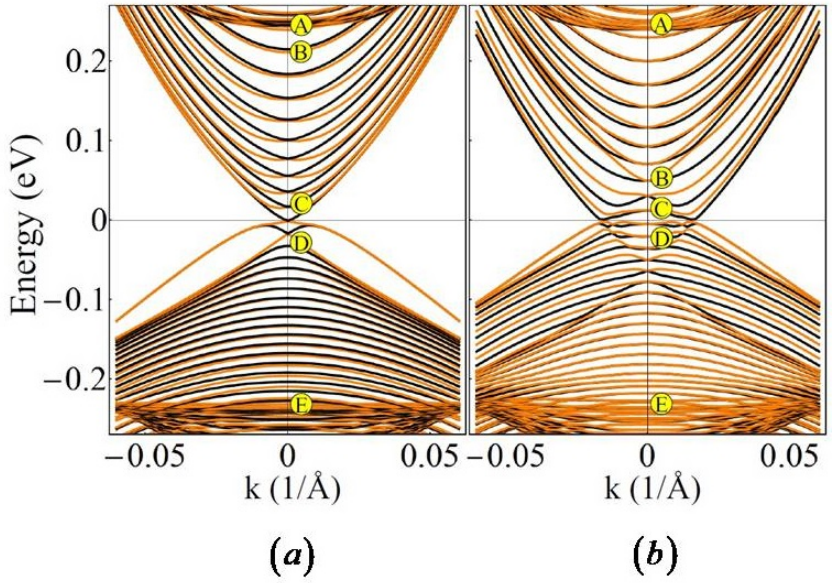

Figure 2.9: (a) Energy spectrum under an influence of the external magnetic field applied longitudinally with total flux through the ribbon $\Phi = 0.583\Phi_0$. (b) Energy spectrum under an influence of an electrostatic field described by the profile in Eq. (2.46) with $V_{\max} = 0.05$ eV. The states marked A-E are shown in Fig. 2.10. (From ref.[58].)

cant, because the relevant physics happens near the interface. The key results are determined by the potential difference across the ribbon, $V_{\max}$. The electric field does not break the TRS, hence the degeneracy at Γ is still protected. Due to the degeneracy, an even number of pairs of a Fermi points characterizes the system, see Fig. 2.9-b.

As a final topic for the normal state of TI-nanoribbon, we discussed is the amplitude of the low-energy wave functions, $|\psi_n(i_0)|^2 = \sum_{\lambda,\sigma} |\psi_{n\lambda\sigma}(i_0)|^2$. More specifically, we are interested in transverse profile of $|\psi_n(i_x, i_z)|^2$. Our interest is motivated by the fact that the strength of the superconducting proximity effect is determined by amplitudes of the wave functions at the TI-SC interface. Note that these wave function are normalized, $\sum_{i_x,i_z} |\psi_n(i_x, i_z)|^2 = 1$. Because the amplitude profiles depend weakly on k (for non-degenerate bands), the spatial profile for a given sub-band

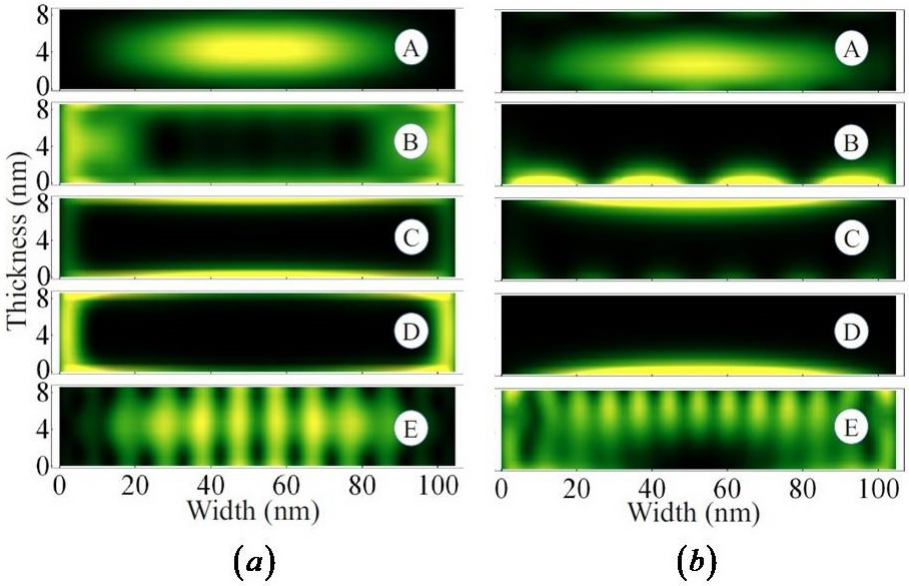

Figure 2.10: Transverse profiles $|\psi_n(i_x, i_z)|^2$ for the low-energy states marked in Fig. 2.9. The yellow regions represent the maxima of the wave functions. Panels A and E show bulk-type states whose energies correspond to the bottom of the conduction band and the top of the valence band, respectively. Panels B, C and D illustrate surface-type states with energies within the bulk gap. (a) Profiles corresponding to Fig. 2.9-a (no electrostatic field). (b) Profiles corresponding to Fig. 2.9-b. (From Ref. [58])

can be determined by looking at the $k = 0$ state.

A few typical profiles are shown in Fig. 2.10. Surface-type states, like the that in Fig. 2.10-a panel B, have maxima localized in the vicinity of the boundaries. However, applying an electrostatic potential modifies the spatial distribution of the wave function, as shown in Fig. 2.10-b. While the bulk-type state profiles (panels A and E) are only slightly distorted, the profiles of the surface-type states are significantly affected. More specifically, the amplitude of the wave function is non-zero near one of the surfaces and vanishes at the opposite surface, as shown in panels B, C, and D. If the proximity coupling with SC is away from the region where the amplitude is large, the proximity-induced gap will be suppressed. Considering the interface-

induced potential alone, we can already conclude that the structure in Fig. 2.6-a is not favorable for stabilizing topological superconductivity, because the induced gap will by vanishingly small for some sub-bands. This conclusion is based on the fact that $|\psi_n(i_x, i_z)|^2$ in Fig.2.10-b panel C and D localizes near the opposite side of the ribbon. Instead, the structure in Fig. 2.6-b, where the superconductors are sandwiching the TI, is immune to the asymmetric potential profile due to the symmetric nature of the setup. The following discussion about the superconducting state of the nanoribbon will be carried out by considering the structure in Fig. 2.6-b.

The superconducting state Let us consider the structure (b) in Fig. 2.6 and focus on the emergence of proximity-induced quasiparticle gap. Due to the symmetry of the structure, the asymmetric interface-induced potential vanishes. Thus, the electrostatic potential can be excluded from this calculation. The nanoribbon cross section is still fixed at $L_z = 9.5$ nm and $L_x = 60$ nm. The geometry of the setup raises two important issues. First, we have to consider a possible phase differences between the two superconductors. This phase difference impacts the proximity-induced pair potential. To capture this phenomenon, we introduce a new parameter ϕ_{SC} and assign the order parameter Δ_{ind} to the lower SC and $\Delta_{ind}e^{i\phi_{SC}}$ to the top SC. Second, we have to carefully incorporate the Peierls substitution that captures the physics of the magnetic orbital effect. A curl of vector potential is associated with the presence of a magnetic flux passing through the TI-nanoribbon. Ideally, there should be no magnetic field within the SCs. The absence of the magnetic field is described by a constant vector potential. This corresponds to $\vec{A} = 0$ for $z < 0$ and $\vec{A} = (BL_z, 0, 0)$ for $z > L_z$. For the SC on the bottom, the value of the vector potential is set to be zero and there is no need for additional modifications. However, the constant vector potential for the SC on the top requires some extra attention.

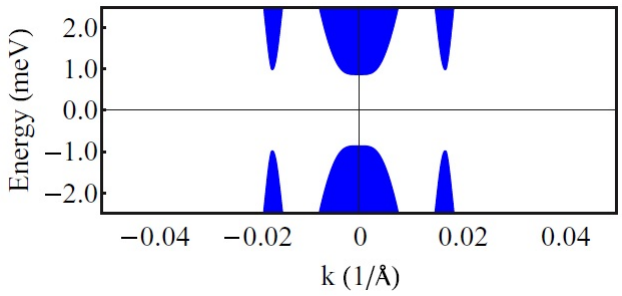

Figure 2.11: Spectrum of the superconducting ribbon with no external magnetic field, $\vec{B} = 0$ and $\mu_{TI} = 0.046\,eV$ (indicated by the blue line in Fig. 2.7). The parameters are $\Delta_0 = 1.5\,meV$, $\phi_{SC} = 0$, $\gamma = 4\Delta_0$ and $\xi = 0.5$. (From Ref. [58])

This constant potential will generate an x-dependent phase factor. The additional phase factor for a lattice site with $i_z = N_z$ will lead to an induced pair potential of the form $\Delta_{ind} e^{i[\phi_{SC} - 2BL_z(i_x - 1)a]}$.

After including all these ingredients, the effective Hamiltonian (2.44) is diagonalized numerically. First we consider the case with no external magnetic field and a chemical potential fixed at the bottom of the second positive-energy band, which corresponds to the blue line in Fig. 2.7. As shown in Fig. 2.11, the gap with a minimum at $k_F^{(1)} \approx 0.017/a$ represents a contribution from the first band, while the gap with a minimum at $k = 0$ is from the second band. For the parameters used in this calculation, a superconductor with a pairing potential of $\Delta_0 = 1.5\,meV$ induces a quasiparticle gap, Δ_{qp}, of magnitude $\approx 1meV$ at the Fermi points. For a generic band n one should expect the size of the induced gap to be about $\Delta_{qp}^{(n)} \approx \Delta_{ind} |\psi_n(i_0)|^2$, where i_0 denotes interface sites. For this particular case, $\Delta_{qp}^{(n)} \approx 0.8\Delta_{ind}$ and we can conclude that the surface-type states of the two relevant bands are similar to the state in Fig. 2.6-b panel C and have about 80 % of their weight localized on the top and bottom surfaces.

Next, we consider a nonzero magnetic field and a chemical potential that crosses multiple bands. The quasiparticle gaps opening at various Fermi points have different

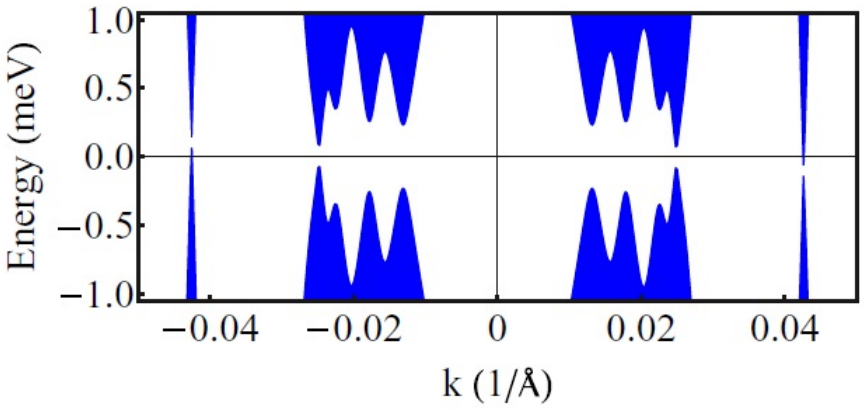

Figure 2.12: BdG spectrum in the presence of an external magnetic field corresponding to $\Phi = 0.8\Phi_0$; the chemical potential is $\mu_{TI} = -0.086\ eV$. Note that $E_{\pm}(-k) \neq E_{\pm}(k)$ because the magnetic field breaks time-reversal symmetry. However, $E_{+}(-k) = -E_{-}(k)$, as required by particle-hole symmetry. (From Ref. [58])

values due to the difference in the transverse profiles. The Hamiltonian in Eq. (2.44), which is constructed within the BdG formalism, ensures the presence of particle-hole symmetry (PHS). The consequence of this symmetry is manifest in the spectrum shown in Fig. 2.12: $E_{+}(-k) = -E_{-}(k)$, where E_{+} and E_{-} represent positive- and negative-energy bands, respectively. The presence of the magnetic field breaks time-reversal symmetry (TRS), which is signaled by the property $E_{\pm}(-k) \neq E_{\pm}(k)$. For this particular set of parameters (i.e., $\Phi = 0.8\Phi_0$ and $\mu_{TI} = -0.086\ eV$), the spectrum becomes gapless. The TI-SC hybrid structure could still host Majorana quasiparticles (which are associated with the band characterized by the lowest values of k_F), but these MBSs will not be robust against disorder, as they can mix with other low-energy states that are present in a gapless system.

The topological phase diagram

The effective Hamiltonian (2.44) depends on several model and control parameters. Our strategy is to systematically determine the influence of each variable on

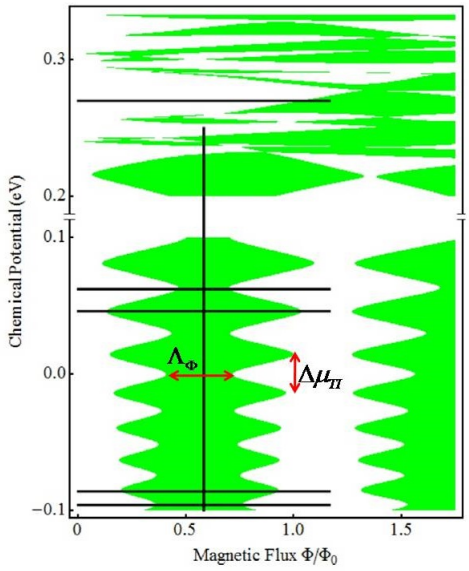

Figure 2.13: Topological phase diagram of the TI nanoribon-SC structure form Fig. 2.6 (b). The green areas represent the non-trivial phase, while the white ones indicate the trivial phase. The parameters used in the calculation are $L_x \times L_z = 60 \times 9.5\ nm$, $\gamma = 8\Delta_0$, $\xi = 0.5$ and $\phi_{SC} = 0$. The evolution of the quasiparticle gap along the cuts corresponding to the black lines are discussed below. $\Delta\mu_{TI}$ is the chemical potential difference between two adjacent maximum width region, Λ_Φ is the minimum width of a magnetic flux separation of the non-trivial topological phase. (From Ref.[58])

the stability of the topological superconducting phase, i.e. on the size of the induced quasiparticle gap. We note that in the absence of an interface-induced potential, the structures shown in Fig. (2.6) (a) and (b) (with $\phi_{SC} = 0$) have similar phase diagrams. Here, we focus on the topological phase diagram of structure (b) with $\phi_{SC} = 0$, $\gamma = 8\Delta_0$ and $\xi = 0.5$. Below, we discuss in detail the effect of each relevant parameter, more specifically γ, ξ, ϕ_{SC}, and the size of the nanoribbon. Note that the possible superconducting phases are characterized by a $\mathbb{Z}_2$ topological index, which can be determine, for example, by calculating the Majorana number($\mathcal{M} = (-1)^v$. A change $\mathcal{M} = 1 \leftrightarrow \mathcal{M} = -1$ indicates a phase boundaries and reflects the fact of the quasiparticle gap closes at $k = 0$. In practice, it is more convenient to determine the phase boundaries from the gap closing condition than to calculate the topological in-

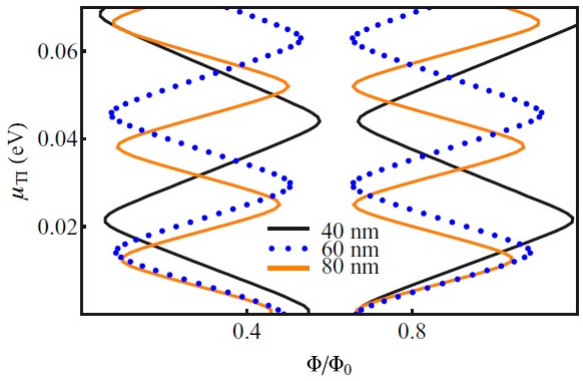

Figure 2.14: Dependence of the phase boundaries on the width of the nanoribbon. L_x = 40, 60, and 80 nm correspond to black, blue dotted, and orange lines, respectively. (From Ref. [58])

variant. Finally, we define two quantities that are useful in characterizing the phase diagram: $\Delta\mu_{TI}$ – the chemical potential difference separating adjacent maximum width regions and Λ_Φ – the minimum width of the topological nontrivial phase (see Fig. 2.13).

First, we study the dependence of the phase diagram on the dimensions of the nanoribbon cross section. More specifically, we vary the width, L_x, while the thickness is fixed at $L_z = 9.5\,nm$. Three sizes of L_x are selected, 40, 60, and $80\,nm$. The corresponding phase diagrams are compared in Fig. 2.14. Note that increasing the width of the wire reduces $\Delta\mu_{TI}$, which is a consequence of reducing the energy separation between two consecutive confinement-induced bands. In addition, a wider ribbon results in the increasing Λ_Φ, i.e. the minimum width of the topological region. Finally, we note that the "center" of the "checkerboard" pattern in Fig. 2.14 shifts to the left (more precisely, toward $\Phi/\Phi_0 = 0.5$) as the ribbon becomes wider. In other words, the center of the nontrivial topological phase moves closer to the value of the magnetic flux equal to half flux quantum. As explained above, the deviation from $\Phi/\Phi_0 = 0.5$ is a finite size effect, which becomes less important as the area

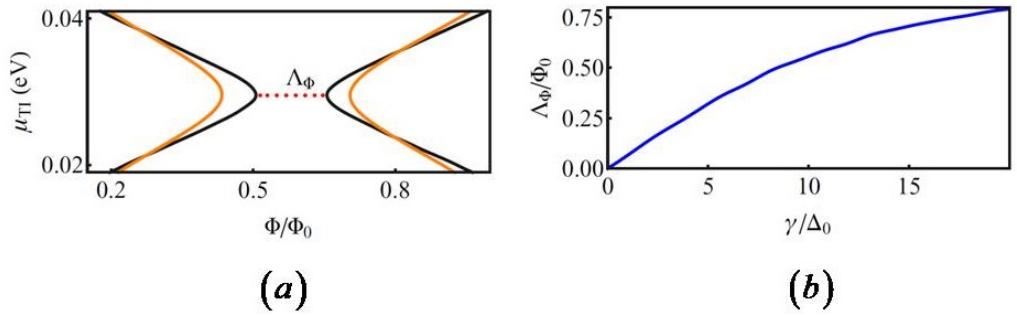

Figure 2.15: (a) The effect of the coupling strength γ on Λ_Φ; black $\gamma = 4\Delta_0$ and orange $\gamma = 8\Delta_0$. (b) The dependence of Λ_Φ on the effective coupling γ. (From Ref. [58])

of the cross section increases.We conclude that using wider ribbons enhances the robustness of the topological superconductor.

Next, we consider the effective TI-SC coupling strength $\gamma = \left(\tilde{t}_+^2 + \tilde{t}_-^2\right)\nu_F$, which was introduced in Eq. (2.38). We note that measuring γ or calculating it from a microscopic model are extremely difficult tasks. Instead, we will treat it as a model parameter. Assuming a perfect interface, we then study the effect of γ on the topological phase diagram. As shown in Fig. 2.15, Λ_Φ increases with increasing the strength of the TI-SC coupling. We conclude that a strong TI-SC coupling enhances the stability of the topological phase.

While the effect of γ is very intuitive, less so is the effect of varying the relative amplitudes of the $\tilde{t}_-$ and $\tilde{t}_+$ couplings, i.e., the parameter $\xi = \tilde{t}_-/\tilde{t}_+$. We note that this parameter provides information about the relative strengths of the couplings of different parity TI bands to the SC. The result, shown in Fig. 2.16, demonstrates that the phase boundaries depend weakly on ξ. This behavior can be interpreted in terms of surface-type states containing approximately equal contributions from the $\lambda = +1$ and -1 molecular orbitals from Eq. (2.19).

The last parameter that requires attention is the superconducting phase difference, ϕ_{SC}. Note that this parameter is relevant in the case of hybrid structures

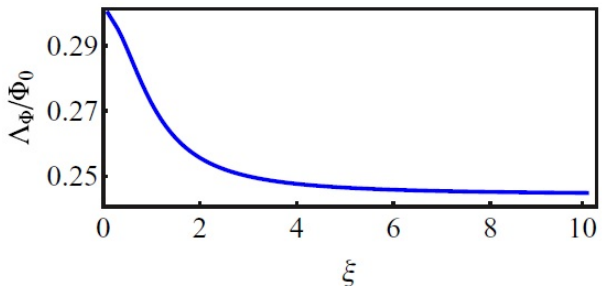

Figure 2.16: The effect of $\xi = \tilde{t}_-/\tilde{t}_+$ on the minimum width Λ_Φ of the topological phase. (From Ref. [58])

involving multiple superconductors, for example structures (b) and (d) in Fig. 2.6. Again, we focus on the effect on the minimum width, Λ_Φ. As illustrated in Fig. 2.17, there is a very strong dependence of Λ_Φ on ϕ_{SC}. More specifically, Λ_Φ exhibits an oscillatory dependence on the phase difference, with nearly zero values of Λ_Φ for $\phi_{SC} \approx (0.8 + 2n)\,\pi$. This behavior is observable for an arbitrary TI-SC coupling strength, but the amplitude of the oscillations increases with γ, as shown in Fig. 2.17. With other parameters being fixed, adjusting ϕ_{SC} could cause a topological phase transition, which represents a rather interesting possibility. The strong dependence of the minimum width on the superconducting phase suggests an additional knob to experimentally control the topological phase.

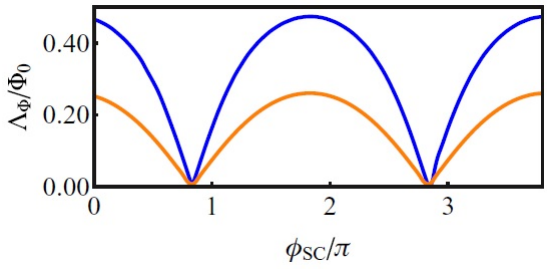

Figure 2.17: The relation of Λ_Φ to the bulk superconducting phase difference, ϕ_{SC}, for $\gamma = 8\Delta_0$ (blue) and $\gamma = 4\Delta_0$ (orange). (From Ref. [58])

The proximity induced gap

In the previous section we discussed the dependence of the topological phase diagram on various parameters. Having a large topological region would, in general, be favorable for the stability of the topological phase. However, this stability depends, ultimately, on the size of the quasiparticle gap. In other words, the existence of a large topological region is (practically) useless if the induced gap that protects the topological phase is small throughout this region.

In this section, the discussion will focus on the magnitude of the proximity-induced superconducting gap in the topologically-nontrivial phase, i.e., on the so-called topological gap. However, we begin with a comment on the induced gap in an absence of an external magnetic field, i.e., in the topologically trivial phase. We note that this gap depends strongly on the wave function amplitude at the TI-SC interface, $|\psi_n(i_0)|^2$. This fact raises a concern about electrostatic fields (e.g., caused by interface-induced type potentials), which can significantly modify the wave function amplitude at the interface. By contrast, the structure (b) in Fig. 2.6 is an ideal case, because of its symmetry and because of the double contacts with superconductors, which maximizes the effective TI-SC coupling, γ. We begin with an analysis of this tructure.

The dependence of the induced gap on the chemical potential is shown in Fig. 2.18. There are three important aspects that we want to address. First, we note the suppression of the quasiparticle gap in the region $\mu > 0.24\,eV$. The reason for this collapse is that the chemical potential reaches the bulk-like bands. A bulk-like state has most of its weight, $|\psi_n(i_0)|^2$, away from the interfaces, which results in a severe reduction of the effective TI-SC coupling. The second aspect is the decay-like profile of the quasiparticle gap at negative chemical potentials. The smaller gap

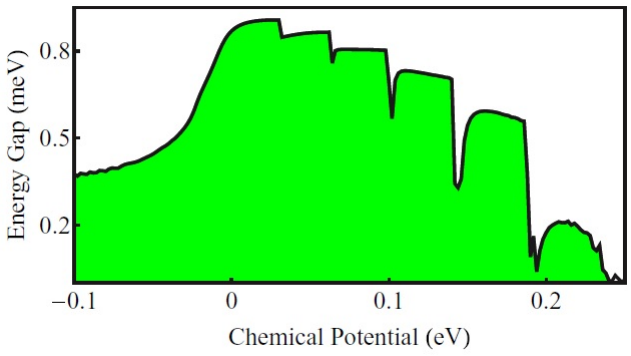

Figure 2.18: Proximity induced gap as a function of the chemical potential. The magnetic flux is fixed at $\Phi = 0.583\Phi_0$ corresponding to the vertical line displayed in Fig. 2.13. This plot is for structure (b) in Fig. 2.6; the model parameters are $L_x \times L_z = 60 \times 9.5\,nm$, $\gamma = 4\Delta_0$, $\xi = 0.5$, $\phi_{SC} = 0$. (From Ref. [58])

in this region is associated with the top-most negative-energy band. This band is almost doubly degenerate away from $k = 0$, as can be seen is Fig. 2.9-a. However, in the actual system, the Dirac point is located near the top of the valence band, which suggests that this region is of little practical importance. The third aspect concerns the sharp drops of the induced gap at certain values of μ_{TI}. These drops are driven by the chemical potential crossing the bottom of different bands (at $k = 0$). The bands come in pairs, but they are not exactly degenerate at $k = 0$. The small separation between the bands at $k = 0$ results in a suppressed induced gap.This phenomenon is a finite-size effect. As a result, the degeneracy condition at $k = 0$ cannot be realized for all bands at the same value of the magnetic flux. In the limit of large cross sections, the degeneracy condition at $\Phi = 0.5\Phi_0$ is band-independent and the sharp drops disappear. Fig. 2.19 suggests that, indeed, a wider ribbon produces weaker drops and the overall quasiparticle gap profile is smoother.

Next, we study the dependence of the induced gap on the Zeeman field at fixed chemical potential. Specifically, we determine the quasiparticle gap along the cuts in Fig. 2.13. Although the region $\mu_{TI} < 0$ has little practical importance, it is included

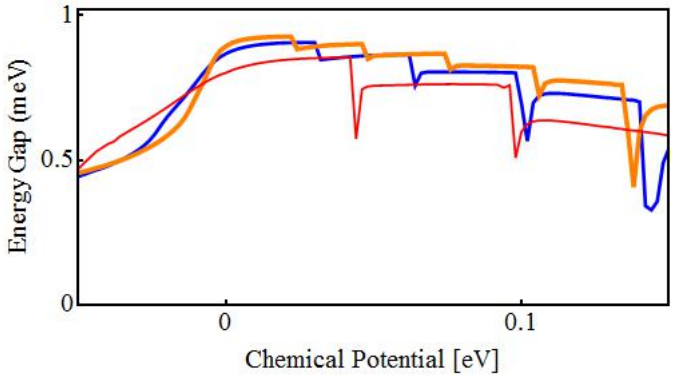

Figure 2.19: Comparison of the gap dependence along the vertical cut in three TI nanoribbons of different sizes. Red, blue, and orange for correspond to Ł$_x$ = 40, 60, and 80 nm, respectively.

for comparison and to point out some interesting physics.

The dependence of the quasiparticle (qp) gap on the magnetic field is shown in Fig. 2.20. The vanishing of the gap signals either a topological quantum phase transition (TQPT), or a gapless superconducting phase. The TQPTs can be easily identified by the characteristic V-shape dependence of the qp gap in the vicinity of the phase transition. Note that around the transition point, the (minimum) gap is determined by the energy at $k = 0$ of the top occupied band. We would like to emphasize three points. The first point is the existence of finite regions with zero induced gap (for $\mu_{TI} < 0$), for example in Fig. 2.20 (d) and (e). This vanishing of the induced gap is not related to a topological phase transition but to a gapless superconducting state, as discussed in relation to Fig. 2.12. The second aspect concerns the "pointy" shape of the non-trivial topological phase in Fig. 2.20-b, where $\mu_{TI} = 0.062\,eV$. This represents a cut through a minimum width region of the topological phase. Any slight deviation of the external magnetic field results in a severe change of the magnitude of the proximity-induced gap. The peak position can be determined by the $k = 0$ degeneracy condition. Since the flux that yields

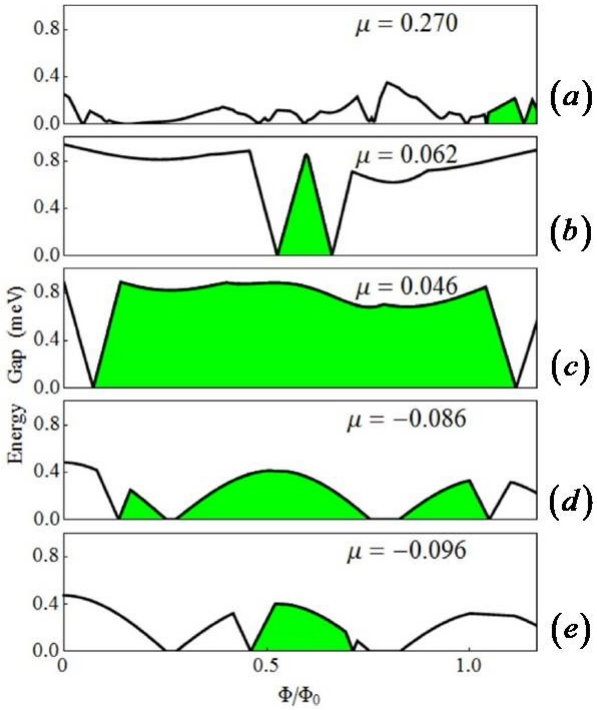

Figure 2.20: Proximity-induced gap as a function of the magnetic flux at different values of μ_{TI}. The green regions represent the topological superconducting phase. The parameters are the same as in Fig. 2.18. (From Ref. [58])

the $k = 0$ degeneracy is not exactly the same for all bands (due to finite size effects, as discussed above), the peak will not line up in the vertical cut in Fig. 2.13. This misalignment causes the characteristic sharp drops illustrated in Figs. 2.18 and 2.19. The third point is a comment about the plateau of the non-trivial phase in Fig. 2.20-c where $\mu_{TI} = 0.046\, eV$. While the (minimum) gap in the vicinity of a TQPT is controlled by the state at $k = 0$, away from the phase boundaries the magnitude of the gap is determined by states with $k \neq 0$. These states depend weakly on the magnetic field, hence the flat-top shape in Fig. 2.20-c.

Next, we focus on structure (a) from Fig. 2.6, i.e., on the single interface TI-SC structure. Due to the asymmetric nature of the setup, an intrinsic electrostatic field will be present. The electrostatic field includes the contribution from the proximity-

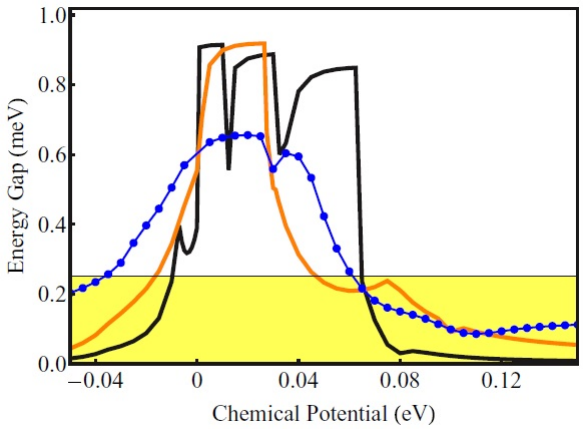

Figure 2.21: Magnitude of the proximity induced gap as a function of chemical potential for a single interface TI-SC structure [structure (a) in Fig. 2.6]. The bias parameters are $V_{max} = 0.0, 0.03, 0.06\,eV$ (blue dots, orange and black respectively). The yellow region represents a reference value of $0.25\,meV$. (From Ref. [58])

induced bias potential, which is described by H_v in Eq. (2.27). Since the surface-type states have their amplitude $|\psi_n(i_0)|^2$ localized mostly on the top and bottom boundaries, the details of the dependence of the potential profile on each quintuple layer, i_z, are not important. The effect of the electrostatic potential is, basically, controlled by the potential difference between the top and bottom surfaces, i.e., the parameter $V_{max} = V_{N_z} - V_1$. We consider three different bias parameters: $V_{max} = 0, 0.03$, and $0.06\,eV$.

A common feature is the drastic drop in the magnitude of the induced gap at negative and large positive values of the chemical potential, as shown in Fig. 2.21, in contrast with the results for the "double interface" setup shown in Fig. 2.19. Note that the reference value (yellow region in Fig. 2.21) represents the magnitude of the induced gap already observed in SM-based systems [48]. The physics of the phenomenon can be explained by examining the spatial profiles of the states (see Fig. 2.10-b). The effect of the interface-induced potential is to modify the spatial profile so that for some bands the states are localized away from the TI-SC interface and,

consequently, the proximity-induced gap is very weak. For example, the top negative energy bands, represented in panel D of Fig. 2.10-b, have their spatial weight mostly away from the interface, which explains the decay-like drop for $\mu_{TI} < 0$. The drop in the $\mu_{TI} > 0$ region can be explained using the same argument, as illustrated by the behavior of the wave function in panel B of Fig. 2.10-b. The drop for the case $V_{max} = 0$ needs additional explanations. In the absence of the bias potential, the state spatial profile is expected to be symmetric, as shown in Fig. 2.10-a. However, away from $\mu_{TI} = 0$, the bands are almost doubly degenerated for both $\mu_{TI} > 0$ and $\mu_{TI} < 0$. When coupled to the SC, these nearly degenerate states combine into linear superpositions that are localized either on the top or the bottom boundaries. Although the top mode couples strongly to the superconductor, the bottom one is weakly coupled and, consequently, acquires only a small induced gap.

Usually, Bi_2Se_3 is not a topological insulator, but rather an n-type semiconductor. The chemical potential, μ_{TI}, is typically placed at the bottom of the (bulk) conduction band. To control μ_{TI}, one can apply a gate potential in an attempt to drain the excess charge away from the sample. When the μ_{TI} lies close to the bulk states or inside the bulk band, there will be bulk-like states with low amplitudes at the interface, which results in a weak superconducting proximity effect. These bulk states will severely suppress the proximity coupling producing a small induced gap. The desired situation is that the chemical potential be close to the middle of the Bi_2Se_3 bulk gap. We investigate the possible manipulation of the chemical potential using two setups: structures (c) and (d) in Fig. 2.6.

The potential profiles are obtained as solutions of a classical Laplace-type electrostatic problem. We note that, more rigorously, these potentials should be determined as self-consistent solutions of the Poisson-Schrödinger equation. This aspect will be

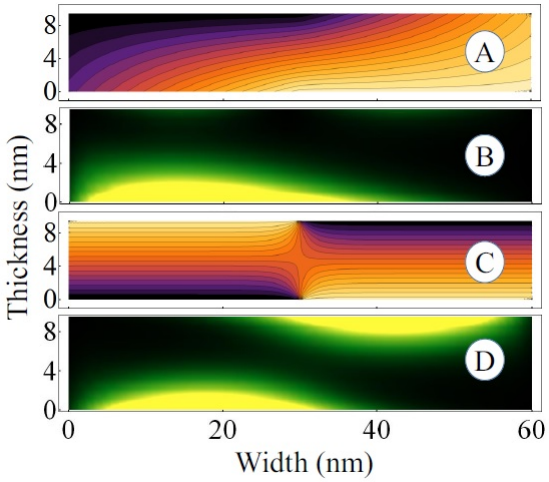

Figure 2.22: Panels A and C show the potential profiles for structures (c) and (d) in Fig. 2.6, respectively. Panels B and D represent the transverse profiles of some particular states in the presence of the potential in A and C, respectively. The dark regions represents the minima. (From Ref. [58])

discussed in more detail in the next chapter. The calculated potential profiles are shown in Fig. 2.22 panels A and C, which correspond to the structures (c) and (d) in Fig. 2.6, respectively. For structure (c), most of the surface-type states form strongly coupled-modes, except the state shown in Fig. 2.22-B (which is localized on the surface opposite to the superconductor). By contrast, due to the more symmetric nature of structure (d), all occupied bands are characterized by strongly coupled-modes.

To examine the effect of the gate potential, consider a system with a chemical potential $\mu_{TI} = 0.22\,eV$, which is just under the bulk conduction band. This value is chosen to mimic the situation of a very lightly doped Bi_2Se_3 nanowire. We apply a gate potential with a profile as shown in Fig. 2.22 and calculate the proximity-induced gap. The results are shown in Fig. 2.23. Without a gate potential, the (minimum) induced gap is expected to be small due to contributions from bulk-type states. Applying a gate potential the induced gap becomes larger. However, the single contact structure always yields a relatively small gap, below the reference level

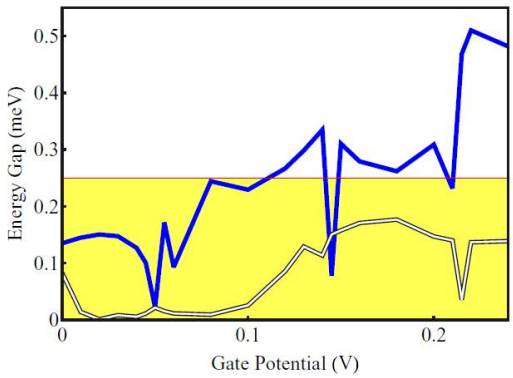

Figure 2.23: Magnitude of the proximity induced gap as a function of the applied gate potential. The double thin line corresponds to strucutre (c) and the solid blue line corresponds to structure (d) (see Fig. 2.6). The yellow region represents the "reference" induced gap. (From Ref. [58])

of $0.25\,eV$. This result is due to the fact that there is always at least one occupied band that corresponds to a weakly coupled mode (see the spatial profile shown in panel B of Fig. 2.22). By contrast, the double contact structure could provide a large induced gap, as shown in Fig. 2.23. This result stems from the symmetry of the setup, which favors the emergence of strongly-coupled modes.

The key ideas presented throughout this chapter can be summarized as follows. An effective Hamiltonian for studying the low-energy physics of TI-SC hybrid structures is constructed using the Bogoliubov–de Gennes formalism. The effective low-energy theory incorporates explicitly the SC proximity effect through a self-energy term. The numerical study of the low-energy effective model reveals that the amplitude of the low-energy wave functions at the TI-SC interface(s) controls the effective TI-SC coupling and, consequently, the strength of the SC proximity effect. The low-energy surface-like states can be localized on both surfaces, or just on the top or the bottom surface of the TI nanoribbon. Consequently, the effective TI-SC coupling is strongly band-dependent. A single-interface TI-SC heterostructure has limited potential to realize a robust topological superconducting phase and host Majorana

bound states. In contrast with the original prediction of Cook and Franz based on an idealized model, tunning the chemical potential may be required in a real system. A symmetric double contact structure seems to be better suited for the realization of robust topological superconductivity and Majorana bound states and provides flexibility in manipulating the chemical potential.

Chapter 3

Electrostatic effects in semiconductor-superconductor hybrid structures

In this chapter we present the proposal for realizing Kitaev's model that has received most attention so far: the semiconductor-superconductor hybrid structure. The basic idea is to realize the condition for effectively spinless fermions by exploiting the strong spin-orbit coupling and large g-factor that characterize narrow-gap semiconductors such as InAs and InSb. Replacing the still-problematic topological insulators with the most technologically-friendly materials (semiconductors) represents a potentially huge practical advantage. The experimental observations consistent with the presence of Majorana zero modes reported in recent years fueled the excitement regarding these hybrid structures. However, important open questions still remain. The answers to many of these questions depend critically on the transverse profiles of i) the single particle wave functions and ii) the effective electrostatic potential. These quantities control the strength of the superconducting proximity effect, the value of

the chemical potential, and the strength of the Rashba spin-orbit coupling, which are key elements of the low-energy physics of the hybrid system. Calculating these transverse profiles involves solving self-consistently a system of Poisson-Schrödinger equations. Typically, this task is extremely costly in a purely numerical approach. In this chapter we propose a new semi-analytical method for solving these equations. This method provides an efficient solution of the Poisson-Schrödinger equations, which, in turn, allows one to efficiently explore the large parameter space required to accurately characterize the low-energy physics of the hybrid system.

3.1 Topological superconductivity in semiconductor-superconductor hetrostructures

The semiconductor-superconductor (SM-SC) hybrid structure involves a setup that is very similar to the one discussed in the previous chapter. Basically, the TI nanoribbon is replaced by a semiconductor (SM) nanowire, which is proximity-coupled to a conventional superconductor. Note that the SM-based heterostructure was proposed in 2010 [54], before the TI nanoribbon proposal [15]. We will focus our attention on the 1D case. However, the original proposal involves a 2D heterostructure [53].

3.1.1 Model Hamiltonian for realizing TSC

The ingredients for realizing the topological superconducting phase in the SM-based hybrid structure are exactly the same as in the case of the TI-based setup: an effectively spinless electronic system proximity-coupled to s-wave superconductors. The spinless fermion system can be obtained by exploiting the strong spin-orbit

coupling of the semiconductor plus an additional Zeeman field, which removes the time-reversal-protected degeneracy at $k = 0$. Despite having the same requirement concerning the presence of an external magnetic field, the underlying physics is different, in the sense that the Zeeman splitting (rather than the orbital effect) is the driving force that ensures the realization of the "effectively splinless" condition. Each component the contributes to the realization of topological superconductivity (TSC) will be discussed in the subsequent sections. The procedure for constructing the effective Hamiltonian will be presented by focusing on three main steps: obtaining an effective Hamiltonian of the SM nanowire, including an external magnetic field, and introducing the superconducting proximity effect.

Low-energy effective Hamiltonian of the SM nanowire

To realize effectively spinless fermions, one can fully spin-polarize the system by applying a strong magnetic field. However, inducing superconducting correlations in a spin-polarized system by proximity-coupling it with a conventional s-wave superconductor is virtually impossible. Two electrons can be paired by proximity-effect (with s-SC) only if their spins are not exactly parallel. This can be realized by combining the polarizing effect of the magnetic field with a strong spin-orbit coupling, which favors opposite spin orientations for electrons with wave vectors k and $-k$.

The spin-orbit coupling in semiconductors can be studied within an 8-band Kane model [34]. The model parameters can be specified for InSb or InAs, which are the materials currently used to realize MBSs [18, 48]. We note however, that, due to the significant number of degrees of freedom, using an 8-band model may not be convenient for addressing certain problems, such as, for example, studying the proximity effect in finite wires. In these cases it is more economical to consider

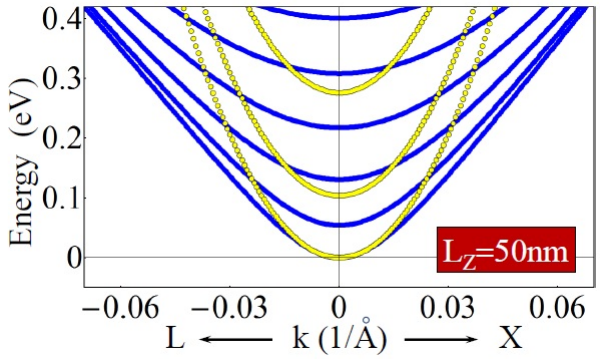

Figure 3.1: Comparison between the energy band structures for a SM thin film with thickness of $50\,nm$ obtained using the 8-band Kane-type model (in blue) and the 2-band model (in yellow). (From Ref. [59])

a two-band effective low-energy Hamiltonian, which corresponds to the conduction bands of the 8-band model. Let us consider the following 2-band tight binding Hamiltonian for electron-doped semiconductors [59],

$$H_{SM} = -t_0 \sum_{i,\delta,\sigma} c^{\dagger}_{i+\delta\sigma} c_{j\sigma} - \mu \sum_{i,\sigma} c^{\dagger}_{i\sigma} c_{i\sigma}, \tag{3.1}$$

where i, δ, σ denote the lattice site, the next-nearest-neighbor, and the spin, respectively. Note that in the long-wavelength limit, $\vec{k} \to 0$, the hopping parameter can be approximated by $t_0 = \hbar^2/2m^*a$ where m^* is the effective mass and a is the lattice constant. Using the 2-band Hamiltonian captures (only) qualitatively the low-energy physics of the semiconductor, as shown in Fig. 3.1. Also, due to the simplicity of the 2-band model, the Rashba spin-orbit coupling (SOC) is not a direct consequence of applying a transverse electric field, but has to be considered as an independent parameter. The effective Rashba-type SOC can be incorporated as

$$H_{SOC} = \frac{i\alpha}{2} \sum_{i,\delta} \Big[c^{\dagger}_{i+\delta_x} \sigma_y c_i - c^{\dagger}_{i+\delta_y} \sigma_x c_i + h.c. \Big], \tag{3.2}$$

where α is the Rashba coefficient. Physically, the Rashba-type SOC is generated by the presence of a transverse field that destroys the structural inversion symmetry of the semiconductor. Introducing the Rashba SOC "manually" is one of the disadvantages of the 2-band model. On the other hand, if the SM were described by the 8-band model, the Rashba-type SOC would naturally emerge when the asymmetric transverse field is applied. The coefficient α can be determined by fitting the spin-split energy bands of the 8-band model in the presence of an asymmetric electrostatic potential.

Incorporating an electrostatic field can be done using the same approach as in the TI case. The corresponding Hamiltonian is

$$H_v = \sum_{i,\sigma} \left[V\left(i\right) - \mu_{TI}\right] c_{i\sigma}^{\dagger} c_{i\sigma}, \tag{3.3}$$

where $V(i)$ is a position dependent function. Note that $V(i)$ represents the "effective" electrostatic field due to gate potentials, interface bias potentials, and the charge of the conduction electrons. Determining this last contribution requires solving the Poisson-Schrödinger equations.

Magnetic field

In the presence of SOC, the SM bands are non-degenerate, except at $k = 0$ where the degeneracy is protected by Kramers theorem. Lifting the degeneracy of the bands at $k = 0$ requires applying an external magnetic field. A gap is opened due to the strong Zeeman effect that characterizes the SM (note that the g-factor can be 50 or

larger in InSb). The corresponding Hamiltonian has the form

$$H_Z = \lambda \sum_{i,\sigma,\sigma'} c^{\dagger}_{i\sigma} (\hat{\sigma}_x)_{\sigma\sigma'} c_{i\sigma'} \tag{3.4}$$

where λ is the Zeeman splitting, $\lambda = \frac{g\mu_B B}{2}$, with g and μ_B denoting the Lande g-factor and the Bohr magneton, respectively. As mentined before, the role of the magnetic field in both TI and SM structures is to lift the degeneracy at $k = 0$. Note, however, that in the TI case this is done through the orbital effect, while in the SM system the Zeeman splitting is the dominant effect. The Zeeman splitting and the Rashba-type SOC combine into realizing an effectively spinless system, which is a key condition in Kitaev's chain model. In addition, in the case of the SM-based system it is required that the chemical potential be within the gap generated by the Zeeman field, so that only one band is occupied. For a multi-band system this condition can be generalized to an odd occupancy requirement. The rather narrow chemical potential window that is favorable for realizing topological superconductivity is a potential drawback of an SM-based structure.

Proximity effect

The last ingredient necessary for realizing Kitaev's model is superconducting paring. The procedure for introducing the superconducting proximity effect follows the same steps as in the case of the TI-based system. The effective low-energy Green function for the SM wire has the form

$$\left[G^{-1}\right]_{nn'}(\omega) = \omega - H_{nn'} - \Sigma_{nn'}(\omega) \tag{3.5}$$

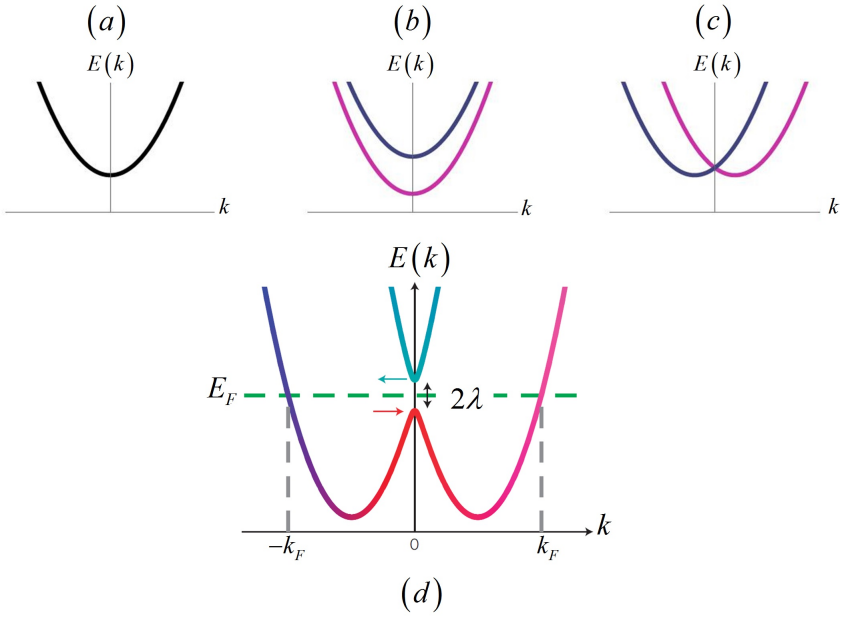

Figure 3.2: Schematic semiconductor band structures under various conditions: (a) SM without SOC and Zeeman splitting (the double degenerate band is described by H_{SM}). (b) SM with Zeeman splitting ($H_{SM} + H_Z$); the spin degeneracy is lifted. (c) SM with Rashba-type SOC ($H_{SM} + H_{SOC}$). (d) (from [17]) SM with both Rashba-type SOC and Zeeman field ($H_{SM} + H_Z + H_{SOC}$).

where $H_{nn'}$ is the effective low-energy Hamiltonian for the SM nanowire expressed in Nambu space and $\Sigma_{nn'}(\omega)$ is the self-energy term capturing the effect of the bulk superconductor. The coupling between SM nanowire and s-wave superconductor is described by

$$H_{SM-SC} = \sum_{i_0,j_0} \sum_{m,\sigma} \left[\tilde{t}^{m\sigma}_{i_0 j_0} c^{\dagger}_{i_0 m} a_{j_0 \sigma} + h.c. \right], \tag{3.6}$$

where $\tilde{t}^{m\sigma}_{i_0 j_0}$ is an element of a coupling matrix between the orbital m on site i_0 of SM and the state σ on site j_0 of the SC. Note that in the case of the 8-band model couplings between the SC and both s-type and p-type SM orbitals have to be consider, which may result in a large number of parameters.

The low-energy states can be obtained by finding the poles of the Green function,

th]

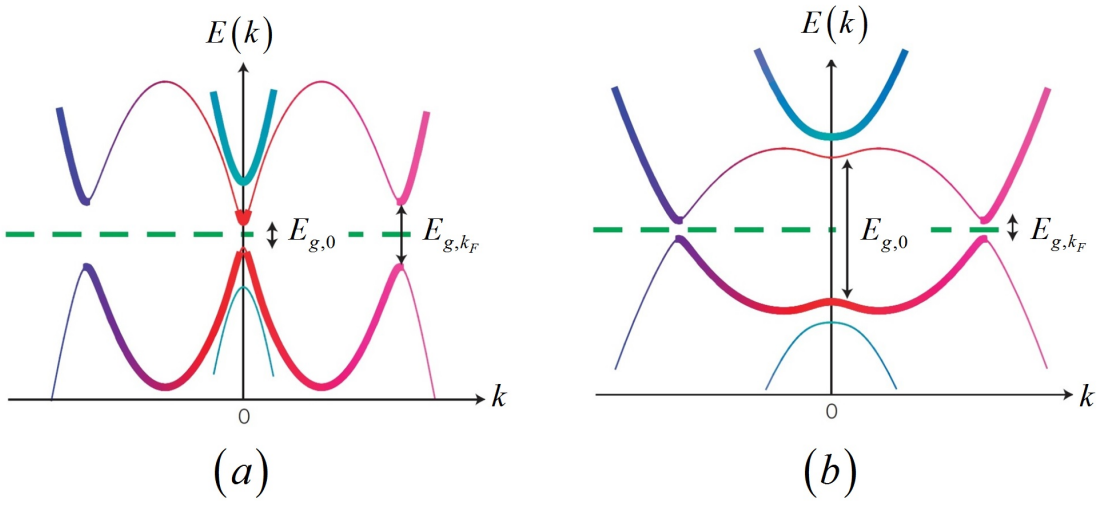

Figure 3.3: Opening of a proximity-induced superconducting gap at the chemical potential. (a) No Zeeman field. (b) Strong Zeeman field. (From [17])

i.e., solving the equation

$$\det\left[\omega - H_{eff}\right] = 0 \tag{3.7}$$

where

$$H^{eff}_{nn'} = \tilde{Z}_{nm} H_{mm'} \tilde{Z}_{m'n'} - \Delta_{nn'}\sigma_y\tau_y - \delta\mu_{nn'}\tau_z.$$

The first term describes the Hamiltonian of semiconductor, which already includes the Rashba SOC and the Zeeman field, while $\tilde{Z}$ is a renormalization matrix. The second term captures the contribution of the proximity-induced pairing potential. The last term describes a proximity-induced inter-band coupling and energy shift.

At zero magnetic field the proximity coupled nanowire is a topologically-trivial superconductor characterized by a finite quasiparticle gap. Applying a Zeeman field reduces the gap at $k = 0$, i.e., the value of $E_{g,0}$ in Fig. 3.3. Eventually, the gap vanishes ($E_{g,0} = 0$) at a certain critical field λ_c signaling a topological quantum phase transition. For $\lambda > \lambda_c$ the gap reopens (see Fig. 3.3-b) and the wire is in a

topological superconducting state that supports Majorana zero modes localized at the ends of the system. For a single-band system (i.e., in the one-dimensional limit) the critical field is

$$\lambda_c = \sqrt{\Delta_{ind}^2 + \mu^2}, \tag{3.8}$$

where Δ_{ind} is the induced superconducting gap and μ is the chemical potential (defined relative to the state $k = 0$ in the absence of a magnetic field).

3.1.2 The topological phase diagram

Realizing the topological superconducting phase at relatively low magnetic fields requires that the chemical potential be in a window of Zeeman splitting with a magnitude of 2λ, as expressed by Eq. (3.8) and depicted in Fig. 3.2. This condition realizes the single band (or, more generally, odd band) requirement necessary for having effectively spinless fermions. For a given value of the chemical potential, the odd band occupancy condition is realized in certain intervals of magnetic fields. The resulting topological phase diagram is shown in Fig. 3.4.

While the odd occupancy condition looks simple, strictly speaking it is relevant only in the weak coupling regime. Indeed, the shape of the phase boundaries depends strongly on the SM-SC coupling, as illustrated in Fig. 3.4. Note that the equivalent study of the dependence on the coupling strength for the topological phase diagram in TI-based systems was shown in Fig. 2.15-a. While theoretically the coupling parameter $\tilde{t}$ can be simply viewed as another unknown variable in the model, physically it characterizes the quality of the SM-SC interface. A larger value of the parameter corresponds to a better interface quality. The consequences of having a larger effective hopping parameter are deep. In essence, this leads to a stronger proximity effect, hence a larger induced gap. In addition, the effective coupling enters the

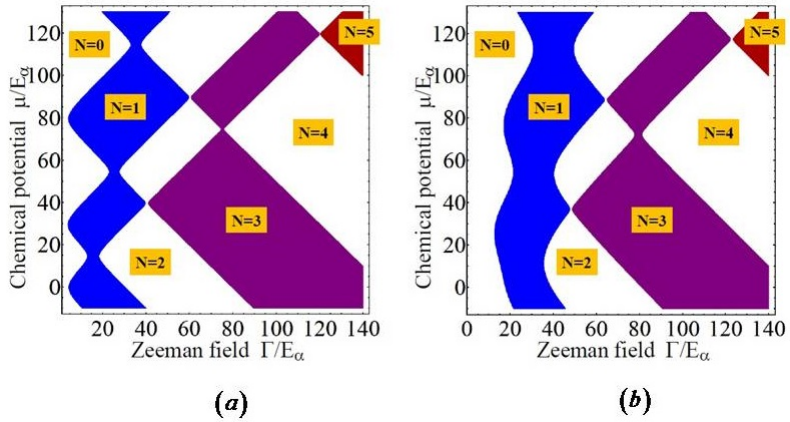

Figure 3.4: Topological phase diagram as a function of chemical potential Zeeman field.The characteristic spin coupling energy is $E_\alpha \approx 0.6K$ and the SM-SC effective coupling is $\bar{\gamma} = 0.25\Delta_0$ in (a) and $\bar{\gamma} = \Delta_0$ in (b). N indicates numbers of low-energy modes localized at each end of the wire. The colored areas denote a nontrivial phase while white indicates the trivial phase. (From [60])

renormalization matrix $\widetilde{Z}$. As a consequence, the low-energy physics of the hybrid system is renormalized by, roughly speaking, a factor $(1 + \gamma/\Delta_0)^{-1}$, where γ is the effective SM-SC coupling and Δ_0 the bulk SC gap. Note, however, that the effective coupling γ depends not only on the hopping parameter $\tilde{t}$ (i.e., on the quality of the interface), but also on the amplitude of the wave function at the interface (hence, on the profile of the effective electrostatic potential). This is one of the reasons for a systematic study of electrostatic effects in SM-based hybrid structures.

Fixing the chemical potential at $\mu = 0\,eV$ and varying the magnetic field provides some insight into the physics of the system near a phase transition. The dependence of the quasiparticle gap on the Zeeman field is shown in Fig. 3.5. The gap is finite everywhere, except at the phase transition. Note the V-shape dependence on the Zeeman field near the transition. This is a characteristic feature also seen in TI-based systems, as shown in Fig. 2.20. The critical Zeeman field at which the transition occurs depends on the induced gap – see Eq. (3.8) – hence, on the effective coupling

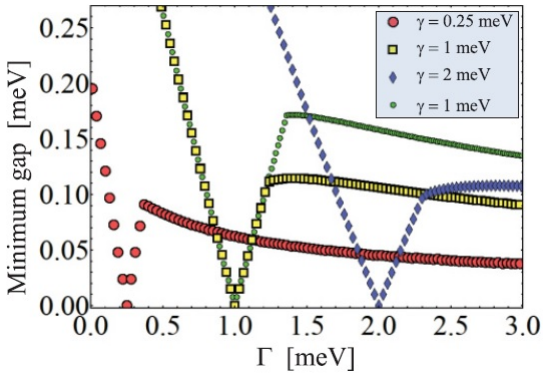

Figure 3.5: Minimum proximity-induced gap at $\mu = 0$ as a function of Zeeman field. The closing of the gap indicates a topological quantum phase transition (TQPT). Before the gap closing the system is in trivial phase, while after the TQPT the system is a topological superconductor. The effective SM-SC coupling modifies the position of the phase transition. All the plots have a Rashba coefficient $\alpha_r = 0.1\, eV$Å except the green dots, which correspond to $\alpha_r = 0.15\, eV$Å. (From [60])

γ. In addition, the size on the gap in the topologically nontrivial region ($\lambda > \lambda_c$) – which protects the Majorana bound states – depends on the Rashba coefficient, as shown in Fig. 3.5. In turn, the Rashba coefficient is controlled by the effective electrostatic potential in the wire – another important reason the motivates a careful study of the electrostatic effect.

3.1.3 Experimental results

Despite potential difficulties, such as, for example, fine-tuning the chemical potential, progress in the realization of SM-based structures is significant compared to TI-based systems. This is mostly due a better knowledge of the materials involved in fabrication of the nanostructures. The growth of high-quality semiconductor nanowires is a well-established field. More recently, advances in the epitaxial growth of aluminum (as bulk SC) on InAs nanowires were reported .

Observing Majorana bouns states involves finite systems, i.e., the presence of

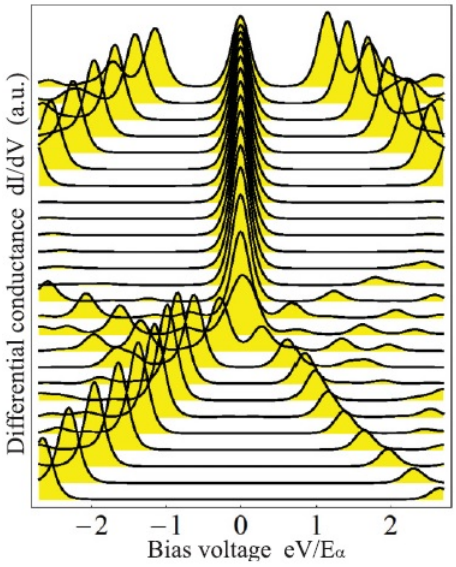

Figure 3.6: Predicted emergence of a zero-bias peak in the differential conductance. The dI/dV lines correspond to different values of the Zeeman field and are shifted for clarity (bottom line: $\Gamma = 11E_\alpha$; top line: $\Gamma = 36E_\alpha$). The peak at zero bias potential emerging at Zeeman fields larger that $\Gamma_c = 21E_\alpha$ represents the signature of the Majorana zero mode. (From [60])

boundaries. Detecting the Majorana bound state can be done by performing a differential conductance measurement. The Majorana zero mode is signaled by the emergence of a peak in dI/dV at zero-bias potential when the Zeeman field is larger than a certain critical value. A theoretical calculation of dI/dV is showed in Fig. 3.6. The signal at zero bias potential can be divided into two regions: a flat region (no signal) at low magnetic fields and a region characterized by a conductance peak (above the critical field). The flat region corresponds to a trivial phase characterized by a finite proximity-induced gap. With increasing the Zeeman field, the gap becomes smaller and eventually vanishes at the phase transition. After the gap reopens, the system is in a topological superconducting phase that supports zero-energy Majorana modes localized at the ends of the wire. Tunneling into these modes results in the zero-bias conductance peak shown in Fig. 3.6.

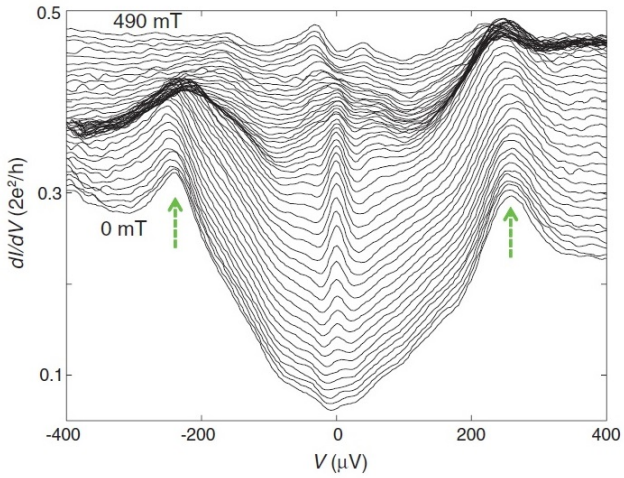

Figure 3.7: Experimentally measured differential conductance versus gate bias for different values of the magnetic field ranging from $0\,mT$ to $490\,mT$ with a $10\,mT$ step increment. The temperature $T = 70mK$. The green arrow indicates the induced gap ($0.25\,meV$). (From Ref. [48])

The first experiment results showing signatures consistent with the presence of Majorana bound states were reported by Mourik et al. in 2012 [48]. A characteristic zero-bias peak emerges at finite magnetic field, as illustrated in Fig. 3.7. The measurements were done on $InSb$ nanowires proximity coupled to niobium titanium nitride, $NbTiN$. The magnitude of a proximity-induced gap was $0.25\,meV$. Although the peak at zero bias is obvious, the signature associated with the closing of the proximity-induced gap is missing. In addition, the induced gap is "soft", i.e., the spectral weight inside the gap is nonzero signaling the presence of (unwanted) low-energy sub-gap states. This feature is associated with the presence of disorder, in particular with a low-quality SM-SC interface. Finally, the height of the zero-bias peak is significantly lower than the theoretical expectation.

Improved growing techniques allow the realization of better quality $InSb/NbTiN$ and $InAs/Al$ structures, as reported recently in the literature. One such example is the dI/dV measurement on an $InSb/NbTiN$ heterostructure shown in Fig.

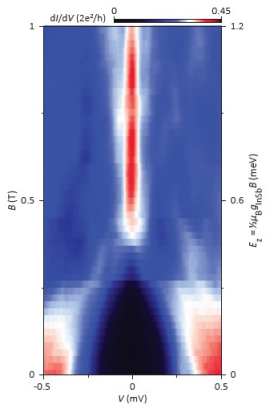

Figure 3.8: Differential conductance, dI/dV, as a function of the bias voltage and Zeeman field. The critical Zeeman field $\Gamma_c = 0.46T$ marks the topological quantum phase transition and the emergence of a zero-bias peak. (From Ref. [74])

3.8. Although the gap closing feature is not completely clear, the reduction of the proximity-induced gap is obvious. In addition, the induced gap much harder and the zero-bias peak stronger.

Despite the successful observation of zero-bias peaks by several different groups in many different SM-SC structures, important question regarding the realization of Majorana zero modes and their stability still remain. For example, one of the "smoking gun" signatures of Majorana modes are the energy splitting oscillations that occur in short wires as a result of the Majorana modes localized at the two ends having an exponentially small overlap. These energy splittings should be seen as splittings of the zero-bias peak. Tunneling into the wire should generate the same splitting when measured from the right or the left ends. This type of correlated splitting, the most basic consequence of the fact that the states responsible for the zero-bias peak are localized at the ends of the wire, has not been observed so far. A critical task is to better understand the dependence of the energy splitting on the Zeeman field. Most of the calculations are done at constant chemical potential. However, this is probably not a very realistic condition for the actual nanostructures. To understand

how the chemical potential depends on the Zeeman field one has to actually solve the full Poisson-Schrödinger problem for each value of the magnetic field. Having an efficient method to solve this problem is, therefore, of critical importance.

3.2 Electrostatic Effect

In both TI-based and SM-based heterostructures, the contribution from the electrostatic effect is formally captured by the term H_v in Eqs.(2.27) and (3.3), respectively. This term of the Hamiltonian represents the total contributions from interface-, gate- and disorder-induced potentials, as well as the electrostatic contribution from the charge associated with conduction electrons. The disorder-induced potential will be excluded from the present considerations. The contribution of the gate potential could be treated as a Laplace-type electrostatic problem. However, the potential generated by the charge in the wire has to be calculated using Poisson equation. Moreover, the charge distribution itself is determined by the spatial profiles of the occupied states, i.e., by the solution of the Schrödinger equation (which depends on the effective electrostatic potential). Hence, the two equations have to be solved self-consistently. Our goal is to obtain a realistic solution for the effective electrostatic potential in the presence of electric charge transfered to the wire due to an interface-induced-type potential. Note that incorporating a gate potential is, in principle, straightforward, but we will not address this aspect of the problem.

3.2.1 The Interface-Induced Potential.

When two materials are electrically connected, a charge transfer is driven by the work function difference. The charge migrates from the material with lower work

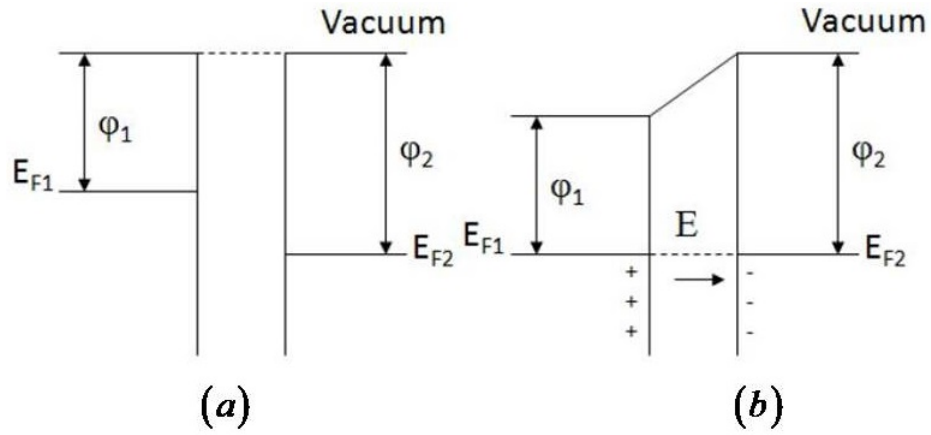

Figure 3.9: Two materials with work functions φ_1 and φ_2, respectively, are used to construct a heterostructure. (a) Isolated components; the vacuum is used as the energy reference and the work functions are related to the chemical potential. (b) Direct contact; charge transfer is allowed, so that the chemical potential is the same throughout the structure. The transfered charge accumulates in the vicinity of the junction creates an electric field. (From Ref. [50])

function to the material with higher work function, as illustrated schematically in Fig. 3.9 The transfer takes place until the chemical potential has the same value throughout the system, when equilibrium is reached. The charge piles up near the interface creating a build-in electric field in that region, which is a signature of the interface-induced potential.

Engineering p-wave superconductivity in an SM-based system involves the contact between a semiconductor and a metal. This results in a well-known problem in the field of semiconductor devices: the physics of metal-semiconductor (M-S) junctions. The strength of the electric field at the interface is determined not only by the work function difference but also by the quality of the interface. In addition, what we really care about is the electric field (or, equivalently, the electrostatic potential) *away* from the interface, i.e. inside the semiconductor. We assume that the characteristic length scale of the semiconductor (i.e., the thickness) is small and the charge density in the semiconductor is low (a few occupied sub-bands).

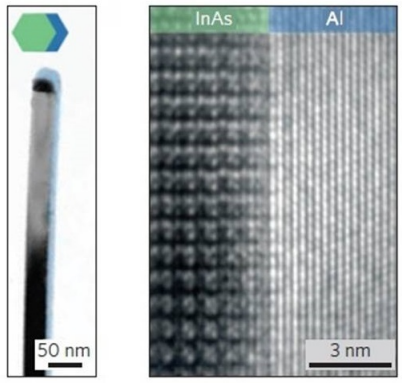

Figure 3.10: (a) TEM image of $InAs/Al$ 1D heterostructure where the aluminum (with thickness $\sim 8nm$) covers two facet of the $InAs$ hexagonal wire. The inset shows the cross section of the structure. (b) High-resolution TEM image at the $Al/InAs$ interface. Note the perfect lattice matching across interface. (From Ref. [40])

3.2.2 The metal-semiconductor junction.

Measuring the work function difference, $\Delta\phi_w$, is a difficult task; characterizing the interface quality is even more daunting. Consider, for example, InAs-Al heterostructures, which represent a recent advance in engineering Majorana devices [40]. The aluminum is grown epitaxially on the semiconductor nanowire, so that the quality of the interface is remarkable, as illustrated in Fig. 3.10-b. Note that the heterostructure can be grown in a various configurations [40], but we will focus on the geometry shown in Fig. 3.10. Even though the materials are specified, determining the $\Delta\phi_w$ is not straightforward. Al has a well-defined work function value of $4.08\,eV$. On the other hand, the work function of $InAs$ (or, more generally, any finite gap semiconductor) is not well-defined because the doping level is not unique and, in low-dimensional systems, there is a significant size dependence of this quantity. Hence, $\Delta\phi_w$ for the hybrid system is not known. We will treat it as a model parameter assuming that the work function of Al is lower than that of InAs. The electrons

will flow from Al into $InAs$. The total amount of charge that flows into the wire is determined by the equilibrium condition, which requires the chemical potential to be the same throughout the system. We will characterize the amount of charge that flows into the system by introducing the filling factor ν_t, which is defined as the ratio between the number of occupies states in k-space and the total number of states in the Brillouin zone. The typical range of interest for the filling factor is of the order of 0.02, or 2% of the whole Brillouin Zone.

The general process for obtaining the potential profile involves the following steps. A certain amount of charge migrates from Al into $InAs$. The chemical potential matching across the interface signals the equilibrium condition. The transfered charge distributes itself according to the Poisson equation. On the other hand, the charge distribution is determined by the spatial profile of the occupied states, which are determined by the Schrödinger equation. In turn, the Hamiltonian in the Schrödinger equation depends on the effective potential that is calculated based on the charge distribution given by the Poisson equation. To reduce the computational cost, the solution of the Poisson's equation is determined analytically for a simplified geometry and the Schrödinger equation is solved within a tight binding approach.

3.2.3 Schrödinger-Poisson equation

The amount and spatial distribution of the charge transfered across the interface has to be determined by solving the Schrödinger and Poisson equations self-consistently. The single particle Schrödinger's equation can be expressed in terms of simple tight binding Hamiltonian of the form

$$H_{SM} = -t_0 \sum_{i,\delta,\sigma} c^{\dagger}_{i+\delta,\sigma} c_{j,\sigma} - (\mu - V_i) \sum_{i,\sigma} c^{\dagger}_{i,\sigma} c_{i,\sigma}, \tag{3.9}$$

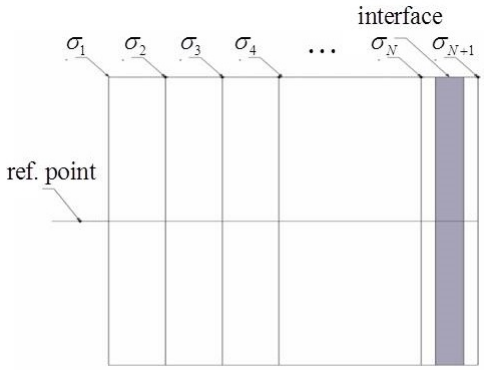

Figure 3.11: Cross section of the 2D system in the slab geometry. The system can be viewed as N uniformly charged layers. Each layer has charge density σ_i, where i denotes the layer index. The interface region between $Al/InAs$ is indicated by the shaded area. The (N+1)-th layer represents the metal, where the positive charge accumulates.

which is the same as the effective low energy Hamiltonian in Eq. (3.1). Note that Eq. (3.9) incorporates the electrostatic effect through the position-dependent local term proportional to V_i. The study will be carried out in both 2D and 1D systems. Due to the simplicity of the solution to Poisson's equation, the 2D case will be presented first.

The Schrödinger-Poisson equation in 2D

The Poisson part: The potential profile in the slab geometry can be consider as generated by a stack of infinite charged layers, each layer having a uniformly distributed charge density σ_i. The cross section of the structure can be depicted as shown in Fig. 3.11. The reference point, i.e., the zero of the electrostatic potential, can be chosen arbitrarily. For convenience, the reference point is chosen to be away from the first layer by half of the lattice constant, $a/2$. We assume charge neutrality,

$$\sum_{j=1}^{j=N+1} \sigma_j = 0, \tag{3.10}$$

where i is the layer index. The layers $i = 1$ to $i = N$ are inside the semiconductor, while the layer $i = N + 1$ is the surface layer of the metal. The charge neutrality condition in Eq. (3.10) and the fact the total number of carriers in the metal is much larger than the number of carries in the SM imply that the positive charge will be localized on the surface of the metal. This positively charged layer will exactly neutralize the negative charge transfered into the semiconductor.

According to Gauss' law, an electric field at a distance x away from an infinity large charged layer with charge density σ is

$$\vec{E} = \frac{\sigma}{2\varepsilon_0}. \tag{3.11}$$

With the reference point defined as in Fig. 3.11, the potential at the position of layer i due to the charged layer j can be expressed as

$$V_{i,j} = \frac{\sigma_j a}{2\varepsilon}\left[(j-1)+\frac{1}{2}\right]\left(1-\frac{|j-i|}{(j-1)+\frac{1}{2}}\right). \tag{3.12}$$

To account for the fact that the charge is not actually confined to strictly 2D planes, we express the potential as the average $V_i = \frac{1}{2}\left(V_{i+\frac{1}{2}} + V_{i-\frac{1}{2}}\right)$, where the contributions $V_{i\pm\frac{1}{2}}$ are calculated using Eq. (3.12) by summing over the j index. The final solution can be written in the form

$$V_i = -\frac{V_0\sigma_i}{4} - V_0\sum_{j=1}^{i-1}\sigma_j\,(i-j), \tag{3.13}$$

where

$$V_0 \;=\; \text{a constant with value determined by } \frac{e}{a\varepsilon}$$

$$\sigma_j \;=\; \sum_{n,\alpha} \gamma_n |\psi_{n\alpha}(j)|^2 \quad \text{where} \sum_n \gamma_n = \nu_t$$

The quantity V_i given by Eq. (3.13) is the analytic solution of the Poisson equation for the slab geometry and represents the effective potential V_i in in Eq. (3.9). The charge densities σ_i are determined by the wave functions of the occupied states and have to be determined by solving the Schrödinger equation.

The Schrödinger part: Since the range of relevant filling factors is of the order of 2%, we focus on the bottom of the conduction band. In the long wavelength limit, the system can be described using a simple cubic lattice, regardless of the actual underlying crystal lattice. The energy dispersion can be expressed as

$$E(k_x, k_y) = E_0 + 2t_0 \left(\cos(k_x a) + \cos(k_y a) + \cos\left(\frac{i_z \pi}{(N_z + 1)} \right) \right), \tag{3.14}$$

where $i_z = 1, ..., N_z$ denotes the index layer. We assume that the system is finite in the *'z-direction'* and that the thickness of the SM film is $N_z \times a$, where a denotes the lattice constant. The energy dispersion in Eq. (3.14) with $k_x = k_y = 0$ can be viewed as corresponding to a particle in a box. The hopping parameter, t_0, determines the curvature of the bands and dictates the inter-band spacing. In the low energy limit, t could be estimated in the effective mass approximation as

$$t_0 \simeq \frac{\hbar^2}{2 m_{eff} a^2} \tag{3.15}$$

where m_{eff} is the effective mass of the conduction electrons. Finally, the Schrödinger equation

$$H_{SM}(k_x, k_y)\psi_{k_x k_y}(z) = E(k_x, k_y)\psi_{k_x k_y}(z), \tag{3.16}$$

where $H_{SM}(k_x, k_y)$ is the Fourier transform of Eq. (3.9), is solved numerically and

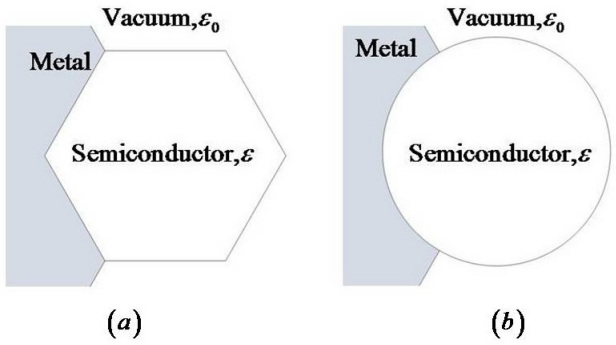

Figure 3.12: Cross section of the 1D heterostructure. (a) The "actual" cross section mimicking the geometry of Ref. [40]. (b) The cross section of the problem that is solved analytically. The two geometries are connected by a conformal transformation (see below). The shaded areas represent an infinitely large metal. The white area is the semiconductor with permittivity ε. The whole system is in vacuum.

the wave functions $\psi_{k_x k_y}(z) \to \psi_{n\alpha}(j)$ are used to calculate the charge densities.

The Schrödinger-Poisson equation in 1D

The Poisson part: The original problem concerns the realization of topological superconductivity and Majorana zero modes in SM wires proximity coupled to s-wave superconductors. A possible geometry is suggested by the $InAs/Al$ structures grown by Krogstrup *et al*, . [40]. The schematic cross section of such a heterostructure is shown in Fig. 3.12-a. This is a rather complex geometry. Instead of solving the Poisson problem directly for this geometry, it is more convenient to solve it for the cylindrical geometry shown in shown in Fig. 3.12-b. Then, we map the potential and the charge density profile from the disk onto the hexagon using a conformal mapping. Hence, the problem reduces to finding the potential for the setup shown in Fig. 3.13, which can be done analytically. The geometry of the problem suggests the use of cylindrical coordinates. First, consider two line charges with densities λ placed at $\{\rho, \phi\} = \{r, \pm\alpha\}$ in a neutral semiconductor of radius $\rho = R$. The metal contact defines the boundary $\rho = R$ and $|\phi| > \theta$, where $-\pi \leq \phi \leq \pi$. The goal is

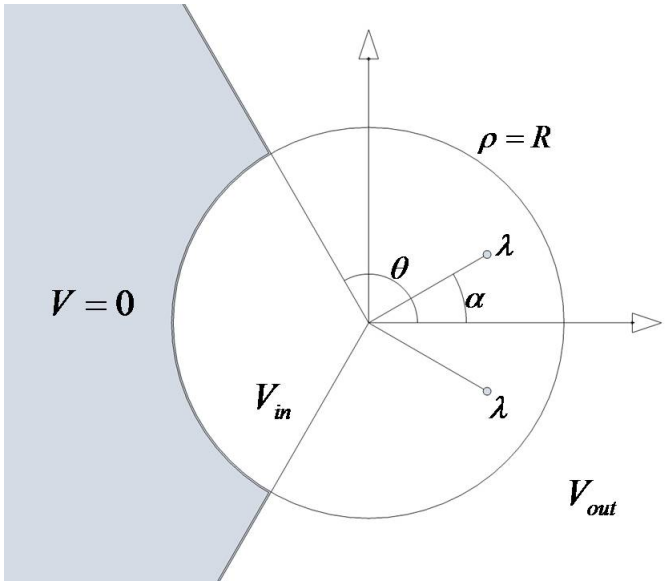

Figure 3.13: Shows the circular cross section nanowire with the radius $\rho = R$ is in contact with an infinitely large metal indicated by the shaded area. θ denotes an angle of a metal contact. α indicates a position of a line charge embedded in the SM. The setup has inversion symmetry respected to $\theta = 0$.

to determine the potential profile inside the wire. Note that the choice of two line charges (rather than one) is suggested by the symmetry of the problem, $\phi \leftrightarrow -\phi$.

The potential for a line charge in free space is

$$v(\rho) = -\frac{\lambda}{2\pi\varepsilon} \ln \rho$$

where ρ is the distance from the wire. The potential generated by two wires with charge densities λ at $(\rho = r, \phi = \pm\alpha)$ is

$$\begin{aligned} v_\lambda(\rho, \phi) &= \frac{\lambda}{4\pi\varepsilon} \left[\ln \frac{1}{\rho^2 + r^2 - 2r\rho\cos(\phi - \alpha)} + \ln \frac{1}{\rho^2 + r^2 - 2r\rho\cos(\phi + \alpha)} \right] \\ &= \frac{\lambda}{\pi\varepsilon} \ln \frac{1}{\rho_>} + \frac{\lambda}{\pi\varepsilon} \sum_{m=1}^{\infty} \frac{1}{m} \left(\frac{\rho_<}{\rho_>} \right) \cos(m\alpha) \cos(m\phi) \end{aligned}$$

Adding a general solution of the Laplace equation, we obtain the following general

solution of the Poisson equation

$$\begin{aligned} V_{in} &= \frac{\lambda}{\pi\varepsilon_i}\ln\frac{1}{\rho_>} + A_0 + \sum_{m=1}^{\infty}\left[A_m\Big(\frac{\rho}{R}\Big)^m + \frac{\lambda}{\pi\varepsilon_i}\frac{\cos(m\alpha)}{m}\Big(\frac{\rho_<}{\rho_>}\Big)^m\right]\cos m\phi, \\ V_{out} &= \sum_{m=1}^{\infty} B_m\Big(\frac{R}{\rho}\Big)^{\left(m-\frac{1}{2}\right)\frac{\pi}{\theta}}\cos\Big(m-\frac{1}{2}\Big)\frac{\pi\phi}{\theta}, \end{aligned}$$

where the constants can be determined from the boundary conditions. Imposing the continuity of the parallel component of the electric field, $E_{\parallel}$, and discontinuity of $E_{\perp}$ at the boundary between the semiconductor and vacuum, we have

$$\begin{aligned} i)\quad V_{in}(R,\phi) &= V_{out}(R,\phi) \quad ; \quad |\phi| < \theta \\ ii)\quad \varepsilon\frac{\partial V_{in}}{\partial\rho}\bigg|_{\rho=R} &= \varepsilon_0\frac{\partial V_{out}}{\partial\rho}\bigg|_{\rho=R} \quad ; \quad |\phi| < \theta. \end{aligned}$$

In addition, the potential at infinity is chosen to be zero, $V_\infty = 0$, and the potential at the surface of the metal is fixed, $V(R,\phi) = V_0 = 0$ for $|\phi| > \theta$ (i.e., we assume that the metal is grounded). The solution takes the form

$$V(\rho,\phi) = \begin{cases} A_0 + \frac{\lambda}{\pi\varepsilon_i}\ln\left(\frac{R}{\rho}\right) + \sum_{n=1}^{\infty}\left[A_n\left(\frac{\rho}{R}\right)^n + \frac{\lambda}{\pi\varepsilon_i}\frac{\cos(n\alpha)}{n}\left(\frac{r}{\rho}\right)^n\right]\cos(n\phi) & r \le \rho \cup \rho \le R \\ A_0 + \frac{\lambda}{\pi\varepsilon_i}\ln\left(\frac{R}{r}\right) + \sum_{n=1}^{\infty}\left[A_n\left(\frac{\rho}{R}\right)^n + \frac{\lambda}{\pi\varepsilon_i}\frac{\cos(n\alpha)}{n}\left(\frac{\rho}{r}\right)^n\right]\cos(n\phi) & r > \rho \cup \rho \le R \\ \sum_{n=1}^{\infty} B_n\left(\frac{R}{\rho}\right)^{\left(n-\frac{1}{2}\right)\frac{\pi}{\theta}}\cos\left[\left(n-\frac{1}{2}\right)\frac{\pi\phi}{\theta}\right]\times\Theta(\theta-|\phi|) & \rho > R \end{cases} \tag{3.17}$$

where

$$A_0 = \frac{1}{2\pi}\sum_{n}^{\infty} B_n\gamma_{n,0}$$

$$
\begin{aligned}
A_n &= \frac{\lambda}{\pi\varepsilon_o}\Gamma_{n0} - \frac{\lambda}{\pi\varepsilon_i}\frac{\cos(n\alpha)}{n}\left(\frac{r}{R}\right)^n + \frac{\lambda}{\pi\varepsilon_o}\sum_{m=1}^{\infty}\cos(m\alpha)\left(\frac{r}{R}\right)^m\Gamma_{mn} - \frac{\varepsilon_i}{\varepsilon_o}\sum_{m=1}^{\infty} mA_m\Gamma_{mn} \\
B_n &= \frac{\lambda}{\pi^2\varepsilon_0\left(n-\frac{1}{2}\right)}\gamma_{n,0} - \frac{\varepsilon_i}{\pi\varepsilon_0\left(n-\frac{1}{2}\right)}\sum_{m}^{\infty}\left(mA_m - \frac{\lambda}{\pi\varepsilon_i}\cos(m\alpha)\left(\frac{r}{R}\right)^m\right)\gamma_{n,m}
\end{aligned}
$$

with

$$
\begin{aligned}
\gamma_{g,n} &= \int_{-\theta}^{\theta}\cos\left(\left(g-\frac{1}{2}\right)\frac{\pi\phi}{\theta}\right)\cos(n\phi)\,d\phi \\
\Gamma_{mn} &= \Gamma_{nm} = \sum_{g=1}^{\infty}\frac{\gamma_{gm}\gamma_{gn}}{\pi^2\left(g-\frac{1}{2}\right)}.
\end{aligned}
$$

Eq. (3.17) gives the potential at (ρ,ϕ) due the presence of the line charges λ at $(r,\pm\alpha)$. The actual potential is created by the whole charge distribution inside the wire, which can be viewed as a collection of line charges. Instead of directly computing the potential at a given point (ρ,ϕ), we determine the values at some surrounding points (to incorporate the fact that the charge is actually distributed over the entire cross section). The final value of the potential at (ρ,ϕ) is obtained by averaging those values from the vicinity of the point.

Let us focus on the lattice shown in in Fig. 3.14-b. The blue points contain input information about the coordinates and the charge density. The output, i.e., the electrostatic potential, is calculated for the red points. Averaging six red points yields the potential at the central blue point. After completing this step of the calculation, the potential of the circular wire is determined. To obtain the potential of the wire with the hexagonal cross section requires a special relation between the coordinates of the circle and the hexagon – a so-called *conformal mapping*. Note that the positions of the points in Fig. 3.14-b are actually determined using this relation from the positions of the corresponding points in Fig. 3.14-a. The conformal

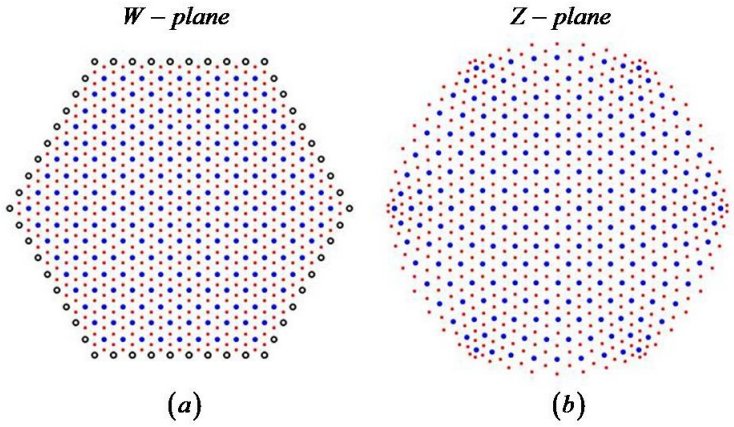

Figure 3.14: (a) Hexagonal nanowire cross section representing a model of the actual system. The small black circles indicate the physical boundary. (b) Circular nanowire cross section with the coordinates of the dots obtained by an inverse conformal transformation $w(z) \rightarrow z$. The blue dots represents a physical lattice site. The red dots are intermediate points where the potential is evaluated.

transformation that relates the two sets of points is given by

$$w = w(z) = w_c + C \int_0^z \frac{1}{(1-\varsigma^n)^{2/n}} d\varsigma, \tag{3.18}$$

where z is the (complex) coordinate of a point in the Z-plane and w is the corresponding coordinate in the W-plane (see Fig. 3.14). The integer n represents the number of sides of a regular polygon, with $n = 6$ for the case of the hexagon. Using the mapping in Eq. (3.18) and its inverse, the charge density is mapped onto the cylindrical wire, then the Poisson equation is solved analytically using Eq. (3.17) (after truncating the sums and retaining enough terms to ensure the desired numerical precision), and, finally, the electrostatic potential is mapped back ontu the hexagonal wire. Note that the inverse conformal mapping is implemented numerically using the procedure described in Ref. [66].

The Schrödinger part: In this study we focus on solving the Schrödinger-Poisson

problem at zero magnetic field. Consequently, we ignore the spin degree of freedom. The effective Hamiltonian describing the SM is a single orbital tight-binding Hamiltonian. Although $InAs$ has a zinc blende crystal structure, the model Hamiltonian is defined on a hexagonal lattice. The hopping in a z-direction (i.e., along the wire) is t_{out}. The in-plane hopping parameter is t_{in}, in general different from t_{out}. The triangular lattice corresponding to a cross section of the wire is shown in Fig. 3.14-a. The effective hopping parameters t_{in} and t_{out} are correlated with the corresponding lattice constants – see Eq. (3.15) – which have to be adjusted to fit the available computational resources. The renormalization of the hopping parameters must be done carefully because this will modify the inter-band spacing. The coarse-graining of the $InAs$ nanowire may also affect the potential profile, which is an issue to be further investigated. The model Hamiltonian describing the $InAs$ nanowire can be expressed as

$$H = -t_{in} \sum_{i,j} c^{\dagger}_{i+\delta} c_j - (\mu + t_{out}) \sum_i c^{\dagger}_i c_i, \tag{3.19}$$

where i and j denote neatest neighbor lattice sites. Note that the spin degree of freedom is excluded from our consideration. Hence, the Rashba-type SOC and the Zeeman field will not enter the calculation.

3.2.4 The Schrödinger-Poisson equation: Numerical results

The self-consistent calculation assumes a fixed density, i.e. a given filling factor. We assume an initial potential profile and solve the corresponding Schrödinger equation. Using the wave functions provided by this solution, we calculate the density profile. Note that the number of occupied states contributing to the charge density is determined by the (fixed) filling factor. The charge density is then introduced into the Poisson equation, which, in turn, will generate a new potential profile. The

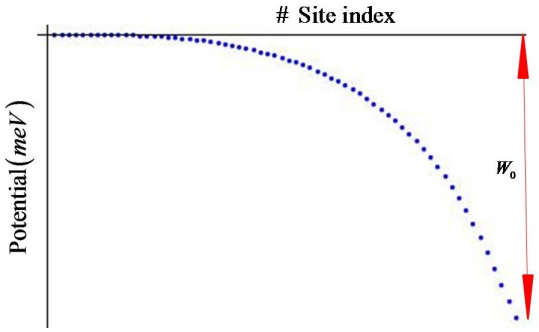

Figure 3.15: Typical 2D potential profile obtained by solving the Schrödinger-Poisson equation. The potential at the left boundary is zero, while the potential at the SM-metal interface is $W_0 \neq 0$.

cycle is repeated until the potential profile convergences. The converged potential represents the effective potential due to the interface-induced electrostatic effect.

The slab geometry

The simplicity of the analytic solution of the Poisson equation in the 2D case allows for a quick solution of the self-consistent problem. This grants easy access to investigating various aspects of the physics. Also, the interpretation of the results is very intuitive and provides a clear picture that shows the significance of the interface-induced potential.

The charge transfered from the metal is mostly distributed in the vicinity of the interface, where the effective potential has its minimum. The left of the semiconductor is exposed to the vacuum, as shown in Fig. 3.11. The charge neutrality condition dictates that the potential at this end of the structure be zero. The values W_0 in Fig. 3.15 representing a potential difference across the SM-metal interface, is related to the work function difference. The key elements of the potential profile are the value of W_0 and its overall shape.

Next, we investigate the dependence of the effective potential on the thickness of

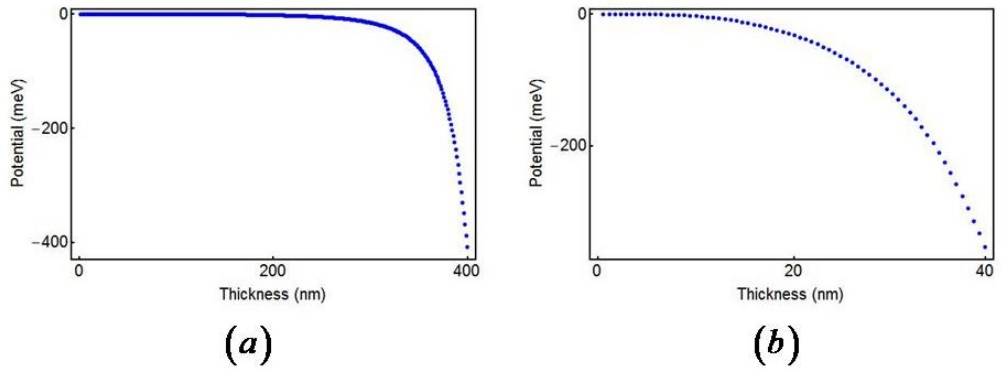

Figure 3.16: Potential profile for two different values of the film thickness: (a) The SM thickness is $\sim 200\,nm$ and $W_0 \sim 400\,meV$. (b) The thickness is $\sim 40\,nm$ and $W_0 \sim 350\,meV$. All other parameters (including the filling factor) are the same.

the semiconductor slab. Since the transfered charge accumulates near the interface, in thick slabs the potential away from the interface is, basically, flat. This behavior is in agreement with the intuition that the far-side of the SM (i.e., the region away from the metal) should not "know" about the presence of an interface. Fig. 3.16-a illustrates this behavior.

The second aspect that we want to address is the dependence on the filling factor. This parameter is an indicator of the amount of the charge trasnfered to the semiconductor and determines the value of the chemical potential (relative to the bottom of the conduction band). Note that the solution of the electrostatics problem is independent of the details of the coupling across the interface, e.g., the effective hopping parameters or the shape of a possible potential barrier that characterizes the interface. In other words, we do not care how "easy" or "difficult" is to transfer charge into the SM; the only relevant quantity is the amount of charge that is transfered. The filling factor is a convenient parameter that characterizes this charge transfer. As shown in Fig. 3.17, higher filling factors result in a sharper drop of the effective potential as one approaches the interface. Note that fixing the filling factor is a con-

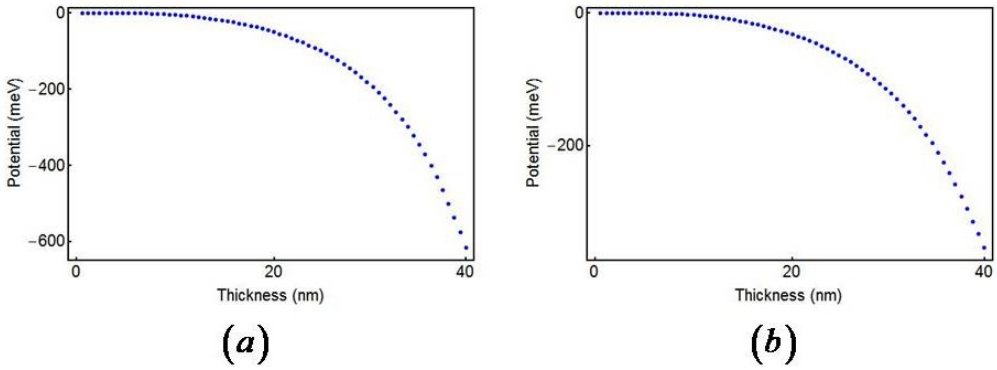

Figure 3.17: Comparison of the potential profiles for two hybrid structure systems with different filling factors: (a) filling factor = 0.02; (b) filling factor = 0.01.

venient way to solve the self-consistent problem, but the actual control parameter is the work function difference.

A useful piece of information concerns the relation between W_0 and the filling factor. For a 40nm-thick film, the dependence of W_0 on the filling factor is shown in Fig. 3.18. As expected, large filling factors generate deep potential wells, i.e., large values $|W_0|$. Note that for filing factors larger than 1% the dependence is almost linear.

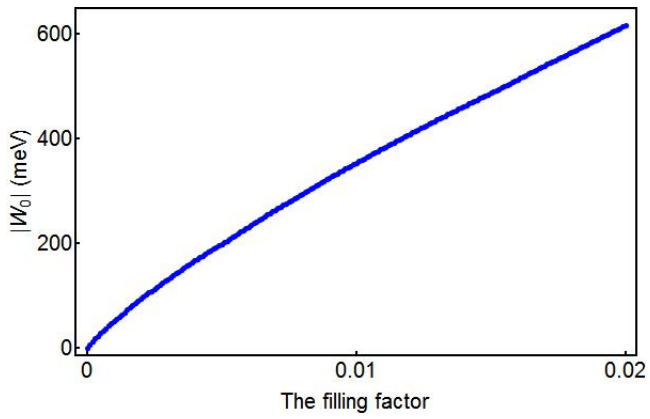

Figure 3.18: Potential difference across the interface, W_0, as a function of filling factor, ν_t. The dependence is almost linear for $\nu_t > 0.01$.

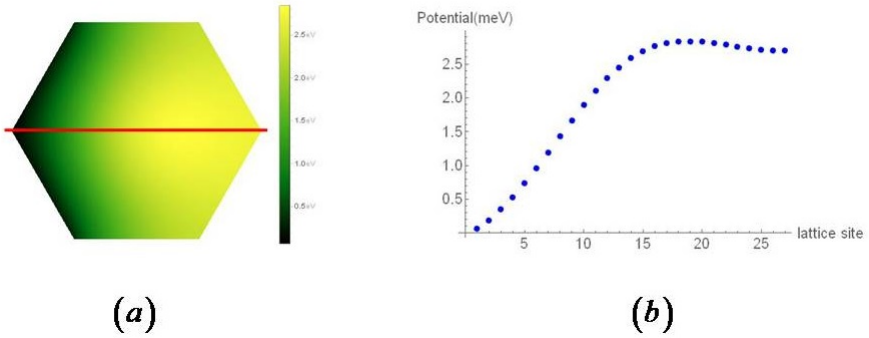

Figure 3.19: (a) A contour plot of the potential profile in the nanowire with a cross section width $50\,nm$. (b) A horizontal cut showing the potential profile according to the red line in (a).

The wire geometry

The solution of the 1D problem based on the analytical result for the Poisson equation, which is expressed as a series, requires significantly more computing time than the 2D case. However, despite involving different geometries and having different levels of mathematical complexity, the overall features of the solutions for the 1D and 2D problems are qualitatively similar. Indeed the shape of the effective potential that dictates the charge distribution across the wire is characterized by a sharp minimum near the interface with the metal and a nearly flat region on the opposite side. A typical profile is shown in Fig. 3.19. Note the similarities between the profile of the potential along a horizontal cut shown in panel (b) and the 2D result for the SM slab, Fig. 3.15.

In conclusion, we have developed a semi-analytical method for efficiently solving the Poisson-Schrödinger equation for semiconductor nanowires coupled to metals/superconductors. The key idea is to use a conformal transformation to map the physically-relevant Poisson problem into a problem that can be solved analytically. Using this method enables one to investigate the hybrid structures predicted to

host topological superconductivity and Majorana zero modes. Standard numerical methods to solve the Poisson-Schrödinger equation are extremely expensive (numerically), which makes the systematic investigation of the large parameter space associated with this problem virtually impossible. To enhance the usefulness of this approach, one has to incorporate the effect of external gate potentials, which can be done following the main ideas developed in this study.

Chapter 4

Conclusions

While the discovery of the integer quantum Hall effect marks the beginning of the "topological era" in condensed matter physics, the possibility of exploiting the topological properties of condensed matter systems for quantum computation seems to be "big prize". However, regardless of whether or not a quantum computer will be ever be built, exploring the topological world reveals a wealth of fascinating physics.

Conceptually, a significant step forward was the realization that the Hall conductivity can be expressed in terms of a topological invariant characterizing the so-called valence Bloch bundle – a vector bundle associated with the occupied states of a (non-interacting) gapped system. This discovery revealed the importance of topology in condensed matter physics and opened the horizon toward the possibility of novel quantum phases of matter. The classification of these quantum phases is based on a paradigm that combines symmetry, topology, and quantum entanglement, while the theoretical study of the topological phases uses a variety of field theoretic, tight-binding, and ab-intio methods, as well as the mathematical tools developed within the field of topology.

On the experimental front, the most significant recent advances are the discovery

of 2D and 3D topological insulators and the realization of hybrid structures that host topological superconductivity and Majorana bound states. Since zero-energy Majorana bound states are a possible platform for topological quantum computation, optimizing these hybrid structures and gaining the ability to manipulate the Majorana modes would represent significant advances toward a future quantum computer.

When investigating topological quantum phases, many valuable insights can be obtained based on model Hamiltonian studies, such as those described in this thesis. These studies provide valuable guidance for the experimental efforts in this area. However, the ultimate test for the validity of any effective low-energy approach comes from comparison with experiment.

4.1 Discussion on the TI-based heterostructure

The topological insulator – based structure was proposed as an alternative to the semiconductor nanowire-superconductor proposal as an attempt to address the potentially limiting requirement concerning the fine-tuning of the chemical potential. The original claim was that, for a certain value of the external magnetic field, the topological superconducting phase is realized regardless on the value of the chemical potential (within the bulk gap). The claim is based on a model calculation that does not include the superconducting proximity effect explicitly and does not consider electrostatic effects (e.g., due to interface-induced potentials and applied gate potentials). The work described in Chapter 2 of this thesis incorporates explicitly these effects. The study is carried out within an effective low energy theory based on a tight binding Hamiltonian. The resulting topological phase is compared with the "ideal" phase diagram in Fig. 4.1. We note that the "fuzzy" top region of the diagram in panel (b) is a result of including the bulk bands. Also, note the different

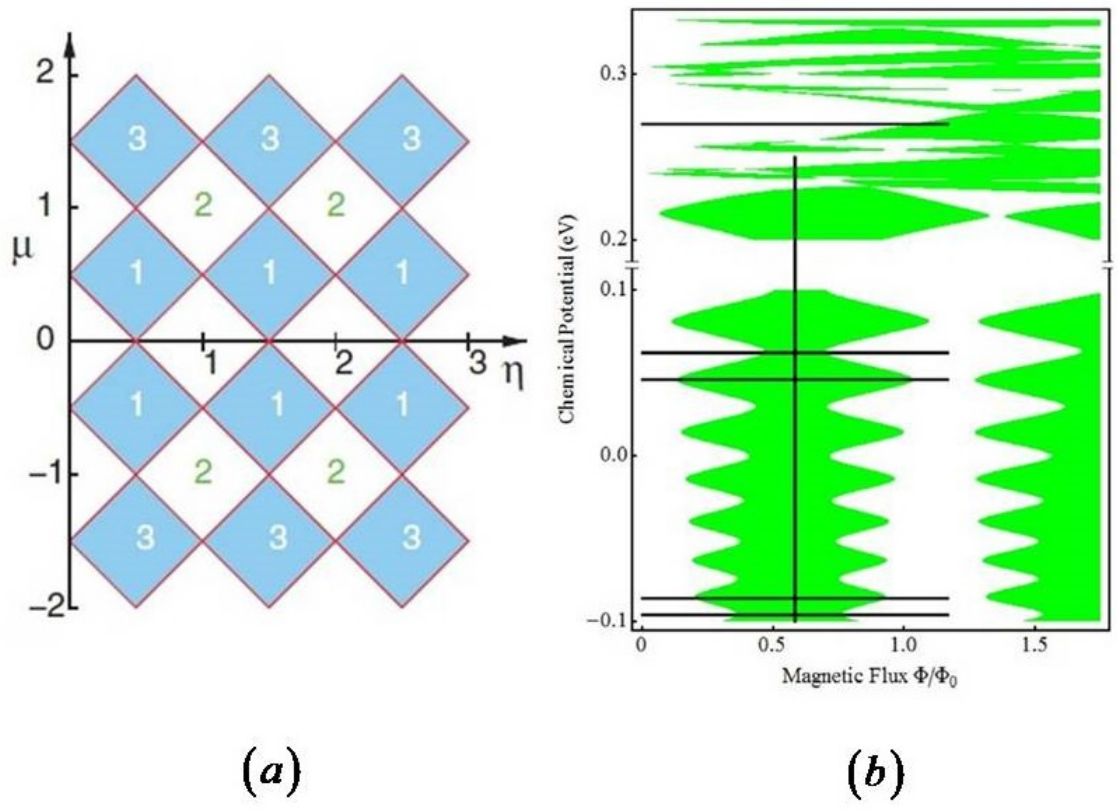

Figure 4.1: Comparison of the topological phase diagram produced by (a) Franz's model and (b) TBH model. The white areas denote the trivial topological phase while the non-trivial phase characterized by the shaded areas.

topology of the two phase diagrams. The key difference arises from the fact that the mimimum width Λ_Φ of the topological region is zero in panel (a) and finite in panel (b). In fact, we have shown (see Chapter 2) that this feature of the phase diagram can be controlled by changing the effective TI-superconductor coupling or the phase difference between the superconductors in a "symmetric" setup, the most favorable for stabilizing the topological phase.

Another element that is neglected in the "ideal" treatment is the fact that real TI materials are doped, e.g., Bi_2Se_3 is, typically, electron-doped. As a consequence, the chemical chemical potential is not within the bulk gap, but rather near the

bottom of the conduction band. Since the ideal place for the chemical potential (i.e., the range of values that ensure the most robust topological phase) is near the middle of the bulk gap, having a gate potential to control μ_{TI} is, in fact, a requirement for a TI-based structure, similar to the situation of semiconductor-based heterostructures. Thus, even in the absence of an interface-induced potential, the gate potential creates a serious problem: it modifies the spatial profile of the surface-like states and, consequently, suppresses the superconducting proximity effect for certain sub-bands. Consequently, the electrostatic effect should be treated with great care. Note that this type of effect also plays a crucial role in semiconductor-based structures. In particular, the electrostatic effect determines the value of the chemical potential of the wire, the strength of the Rashba spin-orbit coupling, and the transverse profile of the wave functions (hence, the superconducting proximity effect), which are key parameters of the system.

4.2 Effects of the electrostatic potential

The conclusions of chapter 2 are based on the assumption that the transverse profile of the effective potential is basically determined by a solution of the Laplace equation. This approximation does not take into account the electrostatic field generated by the electric charge transferred to the wire. A more rigorous treatment can be be obtained by solving self-consistently the Schrödinger-Poisson equations. Since finding the self-consistent solution is numerically expensive, a semi-analytical approach could provide a significant advantage. Such an approach was developed in chapter 3 based on two key ideas: i) solve the Poisson equation (with homogeneous boundary conditions) analytically within a cylindrical geometry and ii) map the solution onto the "realistic" wire cross section using a conformal transformation. We

note that incorporating gate potentials is straightforward. Indeed, one can write the total effective potential as a sum of two terms: one satisfying the Poisson equation and homogeneous boundary conditions and the other satisfying the Laplace equation and the boundary condition imposed by the gates. Since the second term is not modified by the self-consistency condition (because it does not depend on the charge density), it can be calculated numerically (once, for a given configuration) without affecting the efficiency of the scheme.

The study of the electrostatic effect presented in this thesis assumes infinitely long wires, i.e., translation invariance in the direction parallel to the wire. Of course, incorporating finite size effects, e.g., effects related to the presence of a potential tunnel barrier at the end of the wire, will require additional work. Also, while we have not discussed explicitly spin effects, such as sub-band splitting due to spin-orbit coupling and Zeeman interaction, these effects can be easily incorporated into the formalism. Below, we discuss in more detail some of the physical consequences of the electrostatic effect, more specifically: the inter-sub-band spacing, the chemical potential level, the strength proximity coupling, and the Rashba coefficient.

4.2.1 The inter-subband spacing

We consider a quasi-2D semiconductor in the slab geometry in the presence of an interface-induced potential generated by a work function difference. How is the band structure of the semiconductor affected by the electrostatic potential? Is the effect similar to that produced by a uniform electric field? The answers to theses questions are illustrated by the results shown in Fig. 4.2. Before discussing the results, we note that the confinement-induced inter-band spacing depends critically on the effective mass (i.e., on the hopping parameter) and on the slab thickness (i.e., thicker slabs

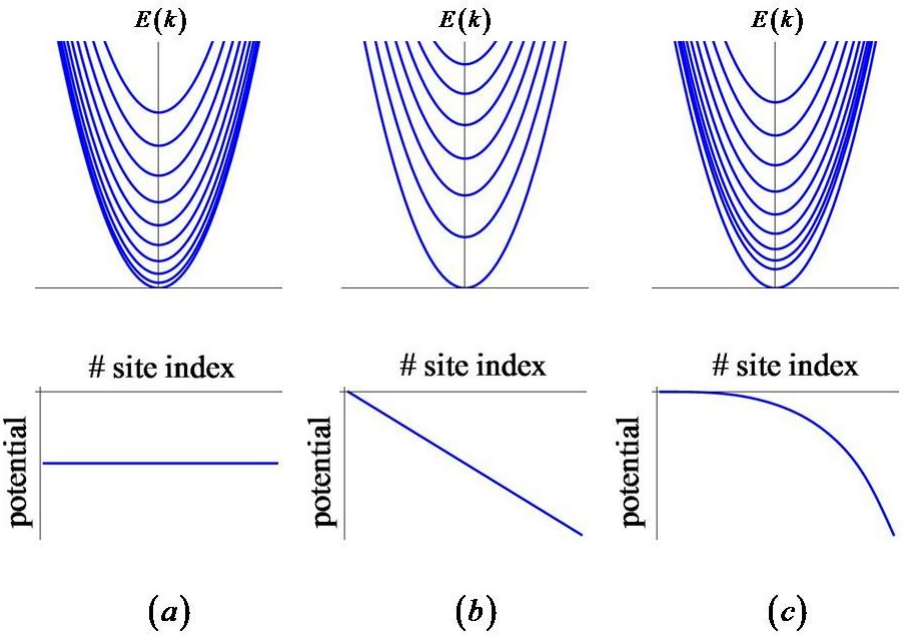

Figure 4.2: Two-dimensional sub-band structures (top) corresponding to different potential profiles (bottom). (a) Constant potential. (b) Linear potential profile. (c) Potential obtained by solving the Schrödinger-Poisson equation.

are characterized by smaller inter-band gaps). We assume that these parameters are fixed.

The band structure corresponding to a uniform potential background, which represents the reference for our potential-dependence analysis, is shown in Fig. 4.2-a. Consider now a uniform electric field corresponding to the linear potential profile shown in Fig. 4.2-b. In this case, all inter-band spacings increase as compared to the reference spectrum. Physically this corresponds to a reduced effective confinement for all confinement-induced sub-bands. Finally, Fig. 4.2-c shows the results based on the self-consistent solution of the Schrödinger-Poisson equations. The spacing between the first and the second bands increases significantly, while higher energy bands are less affected by the potential. Physically, this is due to the fact that the wave function associated with the lowest energy band is strongly confined in the region

where the potential has a minimum, while higher energy states are more delocalized and, consequently, acquire comparable energy shifts (of the order of the "average" potential). In general, we expect the inter-band spacing between low-energy bands to more strongly affected that the gaps between high energy bands. Note, however, that the specific values of the energy shifts depend on the chemical potential, i.e., on how much charge is transfered to the semiconductor. Consequently, the spectrum shown in Fig. 4.2-c will completely change, rather than simply shift rigidly, as additional charge is introduced into the system.

4.2.2 The chemical potential

To better understand the physics discussed in the previous section, let us consider a specific example. The spectra corresponding to two different values of the chemical potential are shown in Fig. 4.3. As discussed in chapter 3, the self-consistency condition is implemented, for convenience, by fixing the filling factor, σ, rather than the chemical potential. Hence, we choose $\sigma = 1\%$ [panel (a)] and $\sigma = 2\%$ [panel (b)], which corresponds to three and four partially occupied bands, respectively. The corresponding values of the chemical potential are shown in the figure. Note the significant change in the spectrum, in sharp contrast with the rigid band picture.

To gain some intuition about the impact of the nonuniform potential on the inter-band spacing, let us consider the transverse profiles of the wave functions associated with the three lowest bands, which are shown in Fig. 4.4. The wave function of the lowest energy band is strongly confined near the right boundary of the slab, where the potential has a minimum. Consequently, its energy will be shifted downwards (as compared to the flat potential case, $V_c = 0$). By contrast, the wave function of the second band has a lower amplitude in the minimum potential region and,

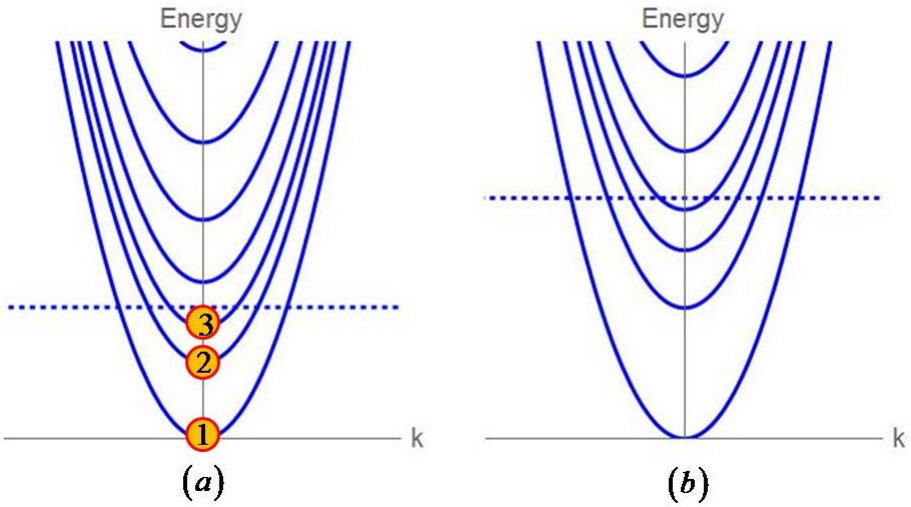

Figure 4.3: The response of the energy spectrum to a change in the filling factor: (a) $\sigma = 1\%$, (b) $\sigma = 2\%$. The horizontal dashed lines represent the chemical potentials.

consequently, will experience a smaller downward shift. For the third band the effect is even weaker. Consequently, The negative energy shifts are strongly band-dependent, which leads to a change of the inter-band spacing.

Another important step in this analysis is to determine the charge density inside the semiconductor slab. This quantity is given by the solution of the Schrödinger equation, more specifically by the wave function profiles and the energies of the states. The contribution of a given state (k_x, k_y) associated with band "i" to the total charge density is $e|\psi_i|^2$, where ψ_{i,k_x,k_y} is the wave function corresponding to that state. For simplicity we assume that the transverse profile of all the states from band "i" is the same, i.e., $|\psi_{i,k_x,k_y}| \equiv |\psi_i|$ independent of (k_x, k_y). In addition, we need to determine the chemical potential corresponding to a given filling factor σ. Note that the chemical potential defines the band filling factors $w_i = w_i(\mu)$, i.e., the fraction of occupied states corresponding to each band. Obviously, we have $\sigma = \sum_i w_i(\mu)$. By inverting this relation we can determine the chemical potential corresponding to a given (total) filling factor [52]. Finally, the total charge density can be written as

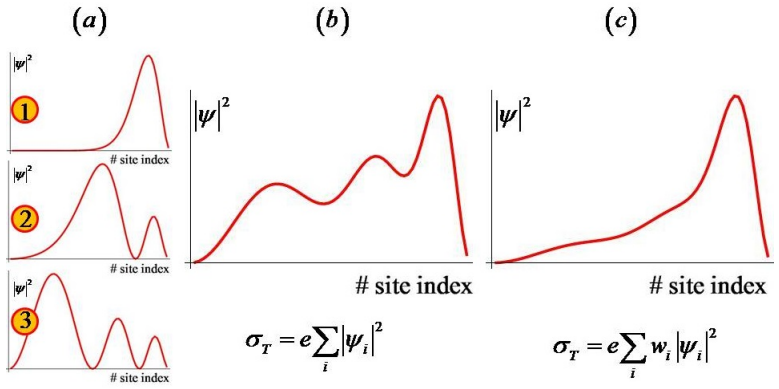

Figure 4.4: (a) Spatial profiles of states from the first three bands marked in Fig. 4.3-a. (b) Fictitious charge density $\sigma_T = e\sum_i |\psi_i|^2$. (c) Actual charge density $\sigma_T = e\sum_i w_i|\psi_i|^2$.

$\sigma_T = \sum_i w_i e|\psi_i|^2$. It is clear from Fig. 4.3 that the largest contribution to the charge density comes from the lowest energy band, since $w_1 > w_2 > w_3$. The charge density corresponding to the energy spectrum in Fig. 4.3-a is shown in Fig. 4.4-c. For comparison, in panel (b) we show a fictitious charge density that would correspond to equal contributions from the first three bands.

4.2.3 The proximity-induced gap

So far, the subsystem in contact with the semiconductor that acts as charge reservoir was assumed to be a normal metal. What happens when this metal turns into a superconductor. As discussed in chapter 2, the semiconductor will pick up superconducting correlations via the proximity effect. Physically, this can be understood in terms of a nonzero probability to find the electrons from the semiconductor inside the superconductor. As a result of this effect, a proximity-induced gap opens in the semiconductor spectrum at the chemical potential. The question is how is this proximity-induced gap affected by the interface-induced potential? Here, we

focus on the magnitude of the proximity-induced gap in a thin film at zero magnetic field in the presence of an interface-induced potential. Since the magnetic field and the Rashba spin-orbit coupling are not included, the induced superconducting state discussed here is topologically trivial.

The superconducting proximity effect can be formally incorporated into the theory as a surface self-energy term. A self-energy term is naturally obtained in the Green function formalism once we integrate out the degrees of freedom associated with the superconductor. Our simplifying working assumption is that the nonlocal contributions to the self-energy are negligible on length scales $1/k_F$ relevant to the low-energy problem, where k_F is the typical Fermi momentum of the semiconductor system. Consequently, we approximate the self-energy by a purely local contribution. Note that this assumption was used in all the calculations for both TI-based and SM-based heterostructures [see, for example, Eq. (2.38)]. The information about the proximity-induced gap can be extracted from the density of states,

$$DOS\left(\omega\right)=-\frac{1}{\pi}\mathrm{Im}\left[Tr\left(\frac{1}{\omega+i\eta-H_{eff}-\Sigma(\omega)}\right)\right]. \tag{4.1}$$

Note that H_{eff} in Eq. (4.1) denotes the Hamiltonian for the semiconductor and the interface-induced electrostatic potential.

The dependence of the proximity-induced gap on the filling factor and on the thickness of the semiconductor slab is shown in Fig. 4.5. First, note the different scales in panels (a) and (b). As expected, increasing the film thickness results in a lower amplitude of the wave functions at the interface and, consequently, in a smaller induced gap. Concerning the dependence on the filling factor (or, equivalently, on the chemical potential), we note that the induced gap tends to increase with increasing filling factor. However, the dependence is discontinuous and even non-monotonic in

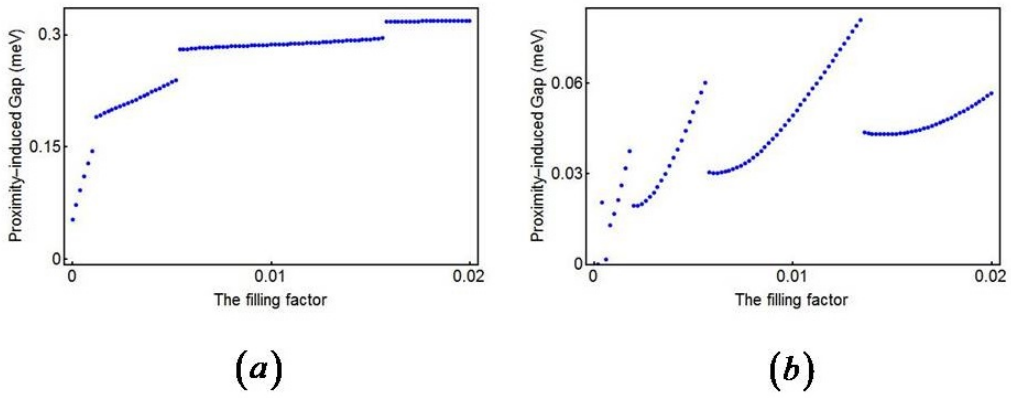

Figure 4.5: Proximity-induced gap as a function of the filling factor for two different values of the film thickness: (a) $40\,nm$ and (b) $200\,nm$. The discontinuities in the dependence of the gap on the filling factor are caused by the chemical potential crossing the bottom of different sub-bands.

the thick film case. We identify these discontinuities with filling factors corresponding to values of the chemical potential exactly at the bottom of some confinement-induced band. We note that for comparison with experiment a similar calculation has to done for the 1D case. While some details will be different, we expect the behavior in the 1D case to be qualitatively similar to these findings.

As mentioned above, the common feature seen in Fig. 4.5, i.e., the discontinuities of the proximity-induced gap as function the filling factor, is related to the chemical potential crossing the the bottom of confinement-induced sub-bands. This behavior has some similarities with that observed in TI-based systems and shown in Fig. 2.18. Note, however, that the physics is different. In the TI case it was a finite size effect: the surface-type states have finite "widths" and, consequently, experience an effective magnetic flux smaller than the nominal value corresponding to the full cross section of the nanoribbon. Since the characteristic "width" is band dependent, the degeneracy condition is not realized for all bands at exactly the same value of the magnetic field, which results in a sharp drop of the induced gap when the chemical

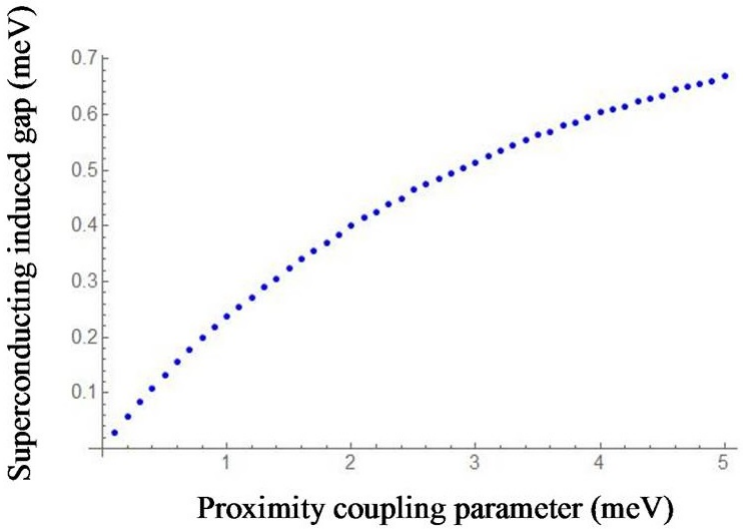

Figure 4.6: Induced superconducting gap as a function of the effective semiconductor-superconductor coupling.

potential is the vicinity of a nearly degenerate point. By contrast, the discontinuities in the semiconductor structure originate in the different "rigidities" of the wave functions associated with different bands. As pointed out in the context of Fig. 4.4-a, wave functions from higher energy bands tend to be less localized in the potential minimum near the interface. Consequently, when the chemical potential crosses into a new band the (minimum) wave function amplitude at the interface is realized by states from the top (new) band, hence it undergoes a discontinuous change. This conclusion has to be carefully verified in the 1D case (i.e., for semiconductor wires), possibly using a more detailed description of the SM band structure, such as an 8-band Kane-type model. Finally, we note that in Fig. 4.5-a the proximity-induced gap is nearly fixed at $0.29\,eV$ for filling factors in the range $0.6-1.6\%$, which suggests that thin slabs are more favorable for realizing a robust superconducting state.

The superconducting correlations are (formally) introduced by the self-energy term. We note that the self-energy depends on the Green function of the superconductor at the interface and on the effective semiconductor-superconductor coupling.

This coupling is a key parameter that determines many of the low-energy properties of the structure, including the induced gap. We have already seen that the topological phase diagram shows a strong dependence on the effective coupling, see Fig. 3.4. The dependence of the induced gap on the the effective coupling parameter for a fixed potential profile is plotted in Fig. 4.6. The size of the gap increase with increasing the effective coupling. Note, however, that the dependence is not linear, which reflects the fact that the induced gap cannot be larger that the bulk SC gap regardless of the coupling strength.

4.2.4 The Rashba SOC

Consider an electron moving in an electric field $\vec{E}$. In the reference frame of the electron, it will experience an effective magnetic field, $B_{eff} \sim \frac{\vec{E}\times\vec{p}}{mc^2}$. This effective magnetic field causes a momentum-dependent Zeeman energy, which is at the origin of the spin-orbit coupling [44], $H_{SO} \sim \vec{\sigma} \cdot \left(\vec{E} \times \vec{p}\right)$. For $\vec{E} = E_0\hat{z}$, the spin-orbit Hamiltonian can be written in the standard form

$$H_R = \alpha_R \left(\vec{\sigma} \times \vec{p}\right) \cdot \hat{z} \tag{4.2}$$

where α_R is the so-called Rashba coefficient. The term $(\vec{\sigma} \times \vec{p}) \cdot \hat{z}$ breaks inversion symmetry. Hence a nonzero Rashba spin-orbit coupling will appear naturally in a system that lacks this type of symmetry.

In a two-band model, the Rashba SOC has to be introduced manually by adding a term like the one in Eq. (3.2). The strength of the interaction, expressed by the parameter α_R, can be determined from experiment or by using a more complicated model, e.g., the 8-band Kane model. However, in the model calculation one has to specify the profile of the effective electrostatic potential that breaks in-

version symmetry. Consequently, a theory of Rashba-type spin-orbit coupling in a semiconductor-based structure has to include i) a suitable multi-orbital model of the semiconductor (e.g., the 8-band Kane model) and ii) a self-consistent calculation of the electrostatic potential. The method for calculating the interface-induced potential described in this thesis is extremely relevant in this context. The interface-induced potential caused by the charge accumulation in the vicinity of the interface breaks inversion symmetry and generates a non-zero Rashba spin-orbit coupling. The coupling strength, α_R, is determined by the electric field, $\vec{E} = -\vec{\nabla}V$, where V is the interface-induced potential profile.

4.3 Perspective: Majorana bound states and quantum computation

The main goal of this thesis is to provide a theoretical analysis that could facilitate enhancing the stability of topological superconducting phases and the realization of robust Majorana bound states in solid state hybrid structures. From the perspective of future applications, the ultimate goal is to be able to manipulate the topologically-protected Majorana modes and to exploit their properties for quantum computation. We conclude this thesis with a few remarks on this fascinating topic.

The first natural question is how can one realize a qubit using Majorana zero modes (MZMs). Consider a complex (Dirac) fermion. It can be mathematically expressed as a combination of two Majorana fermions, $c = \frac{1}{2}(\gamma_1 - i\gamma_2)$. Conversely, any pair of Majorana modes can be thought of as a (regular) fermion. For example, we can say that a pair of MZMs that emerges at the ends of a wire when the system is in the topological superconducting phase can be occupied by an electron (i.e. a

Dirac fermion). Remarkably, the state of the electron is highly non-local ("half" of the state being localized near one end of the wire and "half" near the opposite end). While the concept of "occupation number" is meaningless for Majorana fermions (since the creation and annihilation operators are identical and we have $\gamma^2 = 1$), one can naturally define the *fermion* occupation number for a *pair* of Majoranas, $n = c^\dagger c = \frac{1}{2}(1 - i\gamma_1\gamma_2)$. Note that the product $-i\gamma_1\gamma_2$ represents the fermion parity $(-1)^n$, i.e., it is 1 if the fermionic state is empty and -1 if it is occupied. Hence, a superconducting system containing two MZMs has two distinct zero-energy states: one corresponding to $n = 0$ (i.e., no fermion occupying the Majorana pair) and the other corresponding to $n = 1$. These degenerate ground states, let us call them $|0\rangle$ and $|1\rangle$, can be viewed as the basis states of a qubit.

The idea described above can be generalized to the case of $2N$ MZMs. Indeed, consider a system containing MZMs described by the operators $\gamma_1, \ldots, \gamma_{2j-1}, \gamma_{2j}, \ldots, \gamma_{2N}$. One can formally consider pairs of Majoranas, for example $(\gamma_{2j-1}, \gamma_{2j})$, with $1 \leq j \leq N$, and define the corresponding fermion occupation numbers, $n_1, \ldots, n_N$. The system is characterized by degenerate ground states corresponding to different fermion occupation numbers, $|n_1 n_2 \ldots n_N\rangle$. Typically, the total fermion parity of the system is fixed, i.e., it contains an even or an odd number of fermions. With this constraint, the dimension of the space of degenerate ground states is 2^{N-1}. In other words, a system of $2N$ MZMs can encode $N - 1$ qubits. Remarkably, these qubits are encoded in a highly non-local manner (we implicitly assumed that the MZMs are well separated spatially). Consequently, the quantum information is robust to any local perturbation affecting the system. In other words, perturbing the system in the vicinity of any MZM does not affect the occupation numbers, as long as the perturbation is local. This is stark contrast with the standard (i.e., non-topological)

schemes for quantum computation, which are highly sensitive to decoherence due to local perturbations. This example of topologically protected storage of quantum information reveals the huge potential advantage of using topological states for encoding quantum information.

Consider now a topological superconductor that hosts four MZMs (i.e., N=2). Since the total fermion parity is conserved, we choose an even parity state (i.e., an even total number of electrons in the system), which is consistent with two degenerate ground states $|n_1 n_2\rangle = |00\rangle$ and $|n_1 n_2\rangle = |11\rangle$. These states can be viewed as the basis states of a qubit. A generic state of the logical qubit is represented by the linear superposition

$$\Psi = \alpha\,|00\rangle + \beta\,|11\rangle\,, \quad \alpha^2 + \beta^2 = 1 \tag{4.3}$$

The question now is how to implement a unitary transformation that acts on the state Ψ, i.e., how to realize quantum gates. Note that, ideally, these unitary transformations should also be topologically protected, since otherwise the advantage of having a topologically protected memory would be partially wasted.

The implementation of quantum gates brings to the fore the most remarkable property of the Majorana zero modes: their *non-Abelian statistics*. To understand this property it is convenient to focus on a 2D system containing MZMs. For example, if a perpendicular magnetic field is applied to a 2D topological superconductor, it creates vortices that localize MZMs in their cores. Note that these vortices are topological defects, hence the presence of MZMs. Consider now the exchange of two MZMs bound to the corresponding vortices. One can show that this operation results in one of the Majorana operators switching the sign as a result of the MZM crossing a branch cut associated with the vortex that bounds the other MZM. Mathematically

this can be described by introducing an elementary *braiding* operator, T_i [31],

$$T_i : \begin{cases} \gamma_i \mapsto \gamma_{i+1} \\ \gamma_{i+1} \mapsto -\gamma_i \\ \gamma_j \mapsto \gamma_j \qquad \text{for j} \neq \text{i and j} \neq \text{i} + 1 \end{cases} \tag{4.4}$$

This operator captures the effect of exchanging the positions of MZMs "i" and "i+1". This type of operations, also called *braiding* operations, define a non-Abelian group. The result of a series of elementary operations depends on the order in which they are dome. The exchange can be alternatively described by a unitary matrix acting on the degenerated ground states,

$$U_{i,i+1} = \frac{1}{\sqrt{2}} \left(1 + \gamma_i \gamma_{i+1}\right). \tag{4.5}$$

This matrix form makes transparent the non-Abelian nature of these operations, since, in general, matrix multiplication does not commute. The result is that applying a transformation corresponding to braiding the MZMs is a certain way corresponds to a rotation within the Hilbert space of degenerate ground states [4], i.e., a quantum gate. For example, the action of T can be expressed as

$$U_{j,j+1} \gamma_{j/j+1} U^{\dagger}_{j,j+1} = \mp \gamma_{j+1/j}. \tag{4.6}$$

Focusing on a system containing four MZMs (and having even fermion parity), we have

$$c_1 = \frac{1}{2} \left(\gamma_1 + i\gamma_2\right) \tag{4.7}$$

$$c_2 = \frac{1}{2} \left(\gamma_3 + i\gamma_4\right). \tag{4.8}$$

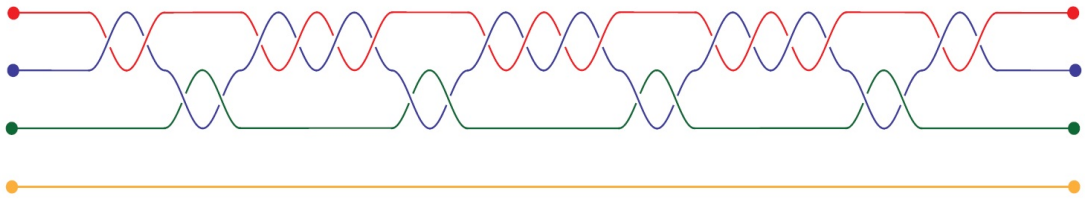

Figure 4.7: Braiding of four MZMs. The vertical axis describes the positions of the MZMs, while the horizontal axis it time. As a result of non-Abelian nature of the MZMs, the final quantum state of the system depends on the specific braid, not simply on the final positions of the MZMs. (From Ref. [64])

Let us assume that we start with the state $|00\rangle$. Exchanging γ_2 and γ_3 results in a new ground state, which can be determined by acting with the unitary operator U_{23} on the initial state. The matrix form of U_{23} in the basis $|00\rangle$, $|10\rangle$, $|01\rangle$, $|11\rangle$ is

$$U_{23} = \frac{1}{\sqrt{2}} \begin{pmatrix} 1 & & & i \\ & 1 & -i & \\ & i & 1 & \\ -i & & & 1 \end{pmatrix}, \tag{4.9}$$

where we have included both the even parity and the odd parity sectors. Note that U_{23} does not mix the two sectors. If the initial state is prepared to be $|00\rangle$, the unitary operator U_{23} will cause the ground state to evolve into

$$|\Psi\rangle = \frac{1}{\sqrt{2}} \left(|00\rangle + i\,|11\rangle \right). \tag{4.10}$$

An example of a more complex braiding operation is illustrated by Fig. 4.7. In general, one can rotate the wave function within the sub-space of degenerate ground states by braiding the MZMs. The goal is the realize a specific unitary transformation that would map the initial quantum state $|n_1 n_2 \ldots n_N\rangle$ that encodes the (classical)

input of a certain computational problem into the final state $|n'_1 n'_2 \dots n'_N\rangle$ that encodes the result of the computation. The unitary transformation that realizes this mapping can be expressed as a product of elementary unitary transformations, this task being realized by a so-called *quantum algorithm*. In the end, this corresponds to a complicated braiding involving the 2N MZMs in the system. The key advantage of using braiding for implementing quantum gates is that the result of an operation does not depend on the exact paths followed by the quasiparticles, but only on the topology of the world lines. In other words, quantum operations using braiding of non-Abelian anyons are topologically protected. Thus, this is an ideal scheme for implementing fault-tolerant quantum computation.

At the time of writing, quantum computers are a dream of the future. Even when realized, quantum computers will not replace classical computers, because they are not faster on computational tasks that classical computers can handle efficiently. However, there are intractable problems, such as factorizing large integers, for which efficient classical algorithms are not known and, as many believe, may not exist. Also there is the world of quantum simulators, which could revolutionize our approach to materials science and biology. This is where the quantum computer could be king.

Bibliography

[1] M. Agostini and *et. al.* Results on $\beta\beta$ decay with emission of two neutrinos or majorons in ${}_{76}ge$ from gerda phase i. *Eur. Phys. J. C*, 75:416, 2015.

[2] Y. Aharonov and J. Anandan. Phase change during a cyclic quantum evolution. *Phys. Rev. Lett.*, 58:1593, 1987.

[3] Y. Aharonov and D. Bohm. Significance of electromagnetic potentials in the quantum theory. *Phys. Rev.*, 115:485–491, Aug 1959.

[4] Jason Alicea. New directions in the pursuit of majorana fermions in solid state systems. *Reports on Progress in Physics*, 75(7):076501, 2012.

[5] Alexander Altland and Martin R. Zirnbauer. Nonstandard symmetry classes in mesoscopic normal-superconducting hybrid structures. *Phys. Rev. B*, 55:1142–1161, Jan 1997.

[6] N. W. Ashcroft and N. D. Mermin. *Solid State Physics*. Saunders College, Philadelphia, 1976.

[7] J. E. Avron, R. Seiler, and B. Simon. Homotopy and quantization in condensed matter physics. *Phys. Rev. Lett.*, 51:51–53, Jul 1983.

[8] B. A. Bernevig and T. Hughes. *Topological Insulators And Topological Superconductors*. Princeton University Press, 2013.

[9] B. Andrei Bernevig, Taylor L. Hughes, and Shou-Cheng Zhang. Quantum spin hall effect and topological phase transition in hgte quantum wells. *Science*, 314(5806):1757–1761, 2006.

[10] M. V. Berry. Quantal phase factors accompanying adiabatic changes. *Proceedings of the Royal Society of London A: Mathematical, Physical and Engineering Sciences*, 392(1802):45–57, 1984.

[11] M. Born and V. A. Fock. Beweis des adiabatensatzes. *Zeitschrift für Physik A*, 51:165–180, August 1928.

[12] J. C. Budich and B. Trauzettel. From the adiabatic theorem of quantum mechanics to topological states of matter. *physica status solidi (RRL) – Rapid Research Letters*, 7(1-2):109–129, 2013.

[13] Y. L. Chen, J. G. Analytis, J.-H. Chu, Z. K. Liu, S.-K. Mo, X. L. Qi, H. J. Zhang, D. H. Lu, X. Dai, Z. Fang, S. C. Zhang, I. R. Fisher, Z. Hussain, and Z.-X. Shen. Experimental realization of a three-dimensional topological insulator, bi2te3. *Science*, 325(5937):178–181, 2009.

[14] J. M. D. Coey. *Magnetism and Magnetic Materials*. Cambridge University Press, 2010.

[15] A. Cook and M. Franz. Majorana fermions in a topological-insulator nanowire proximity-coupled to an *s*-wave superconductor. *Phys. Rev. B*, 84:201105, Nov 2011.

[16] A. M. Cook, M. M. Vazifeh, and M. Franz. Stability of majorana fermions in proximity-coupled topological insulator nanowires. *Phys. Rev. B*, 86:155431, Oct 2012.

[17] A. Das, Y. Ronen, Y. Most, Y. Oreg, M. Heiblum, and H. Shtrikman. Zero-bias peaks and splitting in an al-inas nanowire topological superconductor as a signature of majorana fermions. *Nat. Phys.*, 8(12):887–895, 2012.

[18] M.T. Deng, C.L. Yu, G.Y. Huang, M. Larsson, P. Caroff, and H.Q. Xu. Anomalous zero-bias conductance peak in a nb-inas nanowire-nb hybrid device. *Nano Lett.*, 12(12):6414–6419, 2012.

[19] Freeman J. Dyson. Statistical theory of the energy levels of complex systems. i. *Journal of Mathematical Physics*, 3(1):140–156, 1962.

[20] M. El-Batanouny and F. Wooten. *Symmetry and Condensed Matter Physics*. Cambridge University Press, Cambridge Univerity Press, New York, 2008.

[21] Richard Feyman. *The Feynman Lectures on Physics*. Addison Wesley Longman, 1970.

[22] L. Fu and C. L. Kane. Superconducting proximity effect and majorana fermions at the surface of a topological insulator. *Phys. Rev. Lett.*, 100:096407, Mar 2008.

[23] Liang Fu and C. L. Kane. Topological insulators with inversion symmetry. *Phys. Rev. B*, 76:045302, Jul 2007.

[24] Liang Fu, C. L. Kane, and E. J. Mele. Topological insulators in three dimensions. *Phys. Rev. Lett.*, 98:106803, Mar 2007.

[25] F. D. M. Haldane. Model for a quantum hall effect without landau levels: Condensed-matter realization of the "parity anomaly". *Phys. Rev. Lett.*, 61:2015–2018, Oct 1988.

[26] F. D. M. Haldane. Berry curvature on the fermi surface: Anomalous hall effect as a topological fermi-liquid property. *Phys. Rev. Lett.*, 93:206602, Nov 2004.

[27] A. J. Heeger, S. Kivelson, J. R. Schrieffer, and W. P. Su. Solitons in conducting polymers. *Rev. Mod. Phys.*, 60:781–850, Jul 1988.

[28] Douglas R. Hofstadter. Energy levels and wave functions of bloch electrons in rational and irrational magnetic fields. *Phys. Rev. B*, 14:2239–2249, Sep 1976.

[29] D. Hsieh, D. Qian, L. Wray, Y. Xia, Y. S. Hor, R. J. Cava, and M. Z. Hasan. A topological dirac insulator in a quantum spin hall phase. *Nature*, 452:970–974, April 2008.

[30] Jimmy A. Hutasoit and Tudor D. Stanescu. Induced spin texture in semiconductor/topological insulator heterostructures. *Phys. Rev. B*, 84:085103, Aug 2011.

[31] D. A. Ivanov. Non-abelian statistics of half-quantum vortices in p-wave superconductors. *Phys. Rev. Lett.*, 86:268–271, Jan 2001.

[32] C. L. Kane and E. J. Mele. Quantum spin hall effect in graphene. *Phys. Rev. Lett.*, 95:226801, Nov 2005.

[33] C. L. Kane and E. J. Mele. Z_2 topological order and the quantum spin hall effect. *Phys. Rev. Lett.*, 95:146802, Sep 2005.

[34] Evan O. Kane. Band structure of indium antimonide. *Journal of Physics and Chemistry of Solids*, 1(4):249 – 261, 1957.

[35] A. Kitaev. Periodic table for topological insulators and superconductors. *AIP Conference Proceedings*, 1134(1):22–30, 2009.

[36] A. Yu. Kitaev. Unpaired majorana fermions in quantum wires. *Physics-Uspekhi*, 44(10S):131, 2001.

[37] K. v. Klitzing, G. Dorda, and M. Pepper. New method for high-accuracy determination of the fine-structure constant based on quantized hall resistance. *Phys. Rev. Lett.*, 45:494–497, Aug 1980.

[38] Markus König, Steffen Wiedmann, Christoph Brüne, Andreas Roth, Hartmut Buhmann, Laurens W. Molenkamp, Xiao-Liang Qi, and Shou-Cheng Zhang. Quantum spin hall insulator state in hgte quantum wells. *Science*, 318(5851):766–770, 2007.

[39] H. Kramers. Théorie générale de la rotation paramagnétique daws lew cristaux. *Proc. Amsterdam Akad.*, 33:959–972, 1930.

[40] P. Krogstrup, N. L. B. Ziino, W. Chang, S. M. Albrecht, M. H. Madsen, E. Johnson, J. Nygård, C. M. Marcus, and T. S. Jespersen. Epitaxy of semiconductor–superconductor nanowires. *Nat Mater*, 14:400–406, January 2015.

[41] R. B. Laughlin. Anomalous quantum hall effect: An incompressible quantum fluid with fractionally charged excitations. *Phys. Rev. Lett.*, 50:1395–1398, May 1983.

[42] M. Leijnse and K. Flensberg. Introduction to topological superconductivity and majorana fermions. *Semiconductor Science and Technology*, 27(12):124003, 2012.

[43] Chao-Xing Liu, Xiao-Liang Qi, HaiJun Zhang, Xi Dai, Zhong Fang, and Shou-Cheng Zhang. Model hamiltonian for topological insulators. *Phys. Rev. B*, 82:045122, Jul 2010.

[44] A. Manchon, H. C. Koo, J. Nitta, S. M. Frolov, and R. A. Duine. New perspectives for rashba spin-orbit coupling. *Nat. Mater.*, 14:871–882, 2015.

[45] M. J. Mansfield. *Introduction to Topology*. D. Van Nostrand Co., Inc., Princeton, New Jersey, 1962.

[46] Georgo Metalidis. *Electronic Transport in Mesoscopic Systems*. PhD thesis, Martin Luther University of Halle-Wittenberg, 2007.

[47] Joel E. Moore. The birth of topological insulators. *Nature*, 464(7286):194–198, 2010.

[48] V. Mourik, K. Zuo, S. M. Frolov, S. R. Plissard, E. P. A. M. Bakkers, and L. P. Kouwenhoven. Signatures of majorana fermions in hybrid superconductor-semiconductor nanowire devices. *Science*, 336(6084):1003–1007, 2012.

[49] M Nakahara. *Geometry, Topology and Physics*. CRC Press, second edition, jun 2003.

[50] H. G. Ong and J. Wang. *Study of Carbon Nanotube Based Devices Using Scanning Probe Microscope, Physical and Chemical Properties of Carbon Nanotubes*, chapter Study of Carbon Nanotube Based Devices Using Scanning Probe Microscope. InTech, may 2013. http://dx.doi.org/10.5772/52067.

[51] P. M. Ostrovsky, I. V. Gornyi, and A. D. Mirlin. Interaction-Induced Criticality in Z_2 Topological Insulators. *Physical Review Letters*, 105(3):036803, July 2010.

[52] M. Ali Pourghaderi, Wim Magnus, Bart Sorée, Kristin Meyer, Marc Meuris, and Marc Heyns. General 2d schrödinger-poisson solver with open boundary conditions for nano-scale cmos transistors. *Journal of Computational Electronics*, 7(4):475–484, 2008.

[53] Jay D. Sau, Roman M. Lutchyn, Sumanta Tewari, and S. Das Sarma. Generic new platform for topological quantum computation using semiconductor heterostructures. *Phys. Rev. Lett.*, 104:040502, Jan 2010.

[54] Jay D. Sau, Sumanta Tewari, Roman M. Lutchyn, Tudor D. Stanescu, and S. Das Sarma. Non-abelian quantum order in spin-orbit-coupled semiconductors: Search for topological majorana particles in solid-state systems. *Phys. Rev. B*, 82:214509, Dec 2010.

[55] Andreas P. Schnyder, Shinsei Ryu, Akira Furusaki, and Andreas W. W. Ludwig. Classification of topological insulators and superconductors in three spatial dimensions. *Phys. Rev. B*, 78:195125, Nov 2008.

[56] S.-Q. Shen. *Topological Insulators Dirac Equation in Condensed Matters*. Springer, Springer Heidelberg New York Dordrecht London, 2012.

[57] Barry Simon. Holonomy, the quantum adiabatic theorem, and berry's phase. *Phys. Rev. Lett.*, 51:2167–2170, Dec 1983.

[58] Piyapong Sitthison and Tudor D. Stanescu. Robustness of topological superconductivity in proximity-coupled topological insulator nanoribbons. *Phys. Rev. B*, 90:035313, Jul 2014.

[59] T D Stanescu and S Tewari. Majorana fermions in semiconductor nanowires: fundamentals, modeling, and experiment. *Journal of Physics: Condensed Matter*, 25(23):233201, 2013.

[60] Tudor D. Stanescu, Roman M. Lutchyn, and S. Das Sarma. Majorana fermions in semiconductor nanowires. *Phys. Rev. B*, 84:144522, Oct 2011.

[61] Tudor D. Stanescu, Jay D. Sau, Roman M. Lutchyn, and S. Das Sarma. Proximity effect at the superconductor˘topological insulator interface. *Phys. Rev. B*, 81:241310, Jun 2010.

[62] K. Sun. Condensed matter physics, 2012. Accessed May 2015. http://www-personal.umich.edu/ sunkai/teaching/Fall_2012/phys620.html.

[63] G. Sundaram and Q. Niu. Wave-packet dynamics in slowly perturbed crystals: Gradient corrections and berry-phase effects. *Phys. Rev. B*, 59:14915–14925, Jun 1999.

[64] Chi Yan Jeffrey Teo. *Topological Insulators and Supweconductors*. PhD thesis, University of Pennsylvania, 2011.

[65] D. J. Thouless, M. Kohmoto, M. P. Nightingale, and M. den Nijs. Quantized hall conductance in a two-dimensional periodic potential. *Phys. Rev. Lett.*, 49:405–408, Aug 1982.

[66] L. Trefethen. Numerical computation of the schwarz–christoffel transformation. *SIAM J. Sci. Stat. Comput*, 1:82–102, 1980.

[67] D. C. Tsui, H. L. Stormer, and A. C. Gossard. Two-dimensional magnetotransport in the extreme quantum limit. *Phys. Rev. Lett.*, 48:1559–1562, May 1982.

[68] D. van Dalft and P. Kes. The discovery of superconductivity. *Physics Today*, 63(9):38, Sep 2010.

[69] X. G. Wen. Topological orders in rigid states. *International Journal of Modern Physics B*, 4(2):239–271, 1990.

[70] Eugene P. Wigner. Characteristic vectors of bordered matrices with infinite dimensions. *Annals of Mathematics*, 62(3):548–564, Nov 1955. URL: http://www.jstor.org/stable/1970079.

[71] F. Wilczek and A. Zee. Appearance of Gauge Structure in Simple Dynamical Systems. *Phys. Rev. Lett.*, 52:2111, 1984.

[72] Frank Wilczek. Majorana returns. *Nat. Phys.*, 5:614–618, 2009.

[73] Y. Xia, D. Qian, D. Hsieh, L. Wray, A. Pal, H. Lin, A. Bansil, D. Grauer, Y. S. Hor, R. J. Cava, and M. Z. Hasan. Observation of a large-gap topological-insulator class with a single dirac cone on the surface. *Nat. Phys.*, 5:398–402, May 2009.

[74] H. Zhang, Ö. Gül, S. Conesa-Boj, K. Zuo, V. Mourik, F. K. de Vries, J. van Veen, D. J. van Woerkom, M. P. Nowak, M. Wimmer, D. Car, S. Plissard, E. P. A. M. Bakkers, M. Quintero-Pérez, S. Goswami, K. Watanabe, T. Taniguchi, and L. P. Kouwenhoven. Ballistic Majorana nanowire devices. *ArXiv e-prints*, March 2016.

[75] H. Zhang, C.-X. Liu, X.-L. Qi, X. Dai, Z. Fang, and S.-C. Zhang. Topological insulators in Bi_2Se_3, Bi_2Te_3 and Sb_2Te_3 with a single Dirac cone on the surface. *Nat. Phys.*, 5:438–442, 2009.

[76] Hai-Jun Zhang, Chao-Xing Liu, Xiao-Liang Qi, Xiao-Yu Deng, Xi Dai, Shou-Cheng Zhang, and Zhong Fang. Electronic structures and surface states of the topological insulator $Bi_{1-x}Sb_x$. *Phys. Rev. B*, 80:085307, Aug 2009.

[77] W. Zhang, R. Yu, H.-J. Zhang, X. Dai, and Z. Fang. First-principles studies of the three-dimensional strong topological insulators Bi_2Te_3,Bi_2S_3 and Sb_2Te_3. *New Journal of Physics*, 12(6):065013, 2010.

[78] Yi Zhang, Ke He, Cui-Zu Chang, Can-Li Song, Li-Li Wang, Xi Chen, Jin-Feng Jia, Zhong Fang, Xi Dai, Wen-Yu Shan, Shun-Qing Shen, Qian Niu, Xiao-Liang Qi, Shou-Cheng Zhang, Xu-Cun Ma, and Qi-Kun Xue. Crossover of the three-dimensional topological insulator Bi_2Se_3 to the two-dimensional limit. *Nat. Phys.*, 6(8):584–588, 2010.

[79] J. W. Zwanziger, M. Koenig, and A. Pines. Berry's phase. *Annual Review of Physical Chemistry*, 41(1):601–646, 1990.